Università degli Studi di Cagliari

Ph. D. Course in

INDUSTRIAL ENGINEERING

XXVIII Cycle

MAGNETO-FLUID-DYNAMIC ENERGY CONVERSION SYSTEMS FOR AEROSPACE APPLICATIONS

Curriculum

ING-IND/31

Renato Forcinetti

PhD Course coordinator: Roberto Baratti - Francesco Aymerich

Tutor: Augusto Montisci

2015 – 2016

Thesis presented on March 2017

Università degli Studi di Cagliari

Ph. D. Course in

INDUSTRIAL ENGINEERING

XXVIII Cycle

MAGNETO-FLUID-DYNAMIC ENERGY CONVERSION SYSTEMS FOR AEROSPACE APPLICATIONS

Curriculum

ING-IND/31

Renato Forcinetti

PhD Course coordinator: Roberto Baratti - Francesco Aymerich

Tutor: Augusto Montisci

2015 – 2016

Thesis presented on March 2017

Dedicated to my daughter Michela

Contents

Acknowledgements

A few words to thank all the people who have been close to me in the last years and have helped me to finish this work.

First of all, I'd like to thank my supervisor Augusto Montisci, for his willingness, his support and for being so generous, genuine, unconventional and straightforward. Special thanks goes to Sara Carcangiu, who helped me a lot whenever I needed during these years, for her kindness and her friendship. I thank them both for putting up with me despite my bad temper.

Additional thanks go to the whole Circuit Theory research group of the Department of Electrical and Electronic Engineering of the University of Cagliari, coordinated by Alessandra Fanni.

Part of this dissertation has been completed at the SIMAP Laboratory of the CNRS, in Grenoble. Thanks to my supervisor Antoine Alemany for his mankind, his determination and for sharing with me his enormous experience and expertise inside the MHD world.

Finally, but not secondary, I'd like to thank my parents, for their support and their unconditional love during my endless studies.

The last thinking is for Alessandra. Thank you for existing in my life.

List of figures

List of Tables

Nomenclature

$\boldsymbol{M}$ = vector quantity	M = scalar quantity		
Electromagnetic	**Fluid dynamic**	**Geometric**	**Generic**
$\boldsymbol{B}$ = magnetic flux density vector [T]	$\boldsymbol{v}$ = velocity vector [m/s]	r = distance [m]	$\boldsymbol{g}$ = gravitational acceleration
$\boldsymbol{H}$ = magnetic field vector [A/m]	$\bar{v}$ = velocity amplitude [m/s]	L_0 = system characteristic dimension [m]	$\boldsymbol{I_d}$ = identity tensor
$\boldsymbol{A}$= magnetic vector potential [(V·s)/m]	v_T= charges' velocity (drag component) [m/s]	R_d = duct radius [m]	e = total energy per volume unit [J/m^3]
$\boldsymbol{D}$ = electric displacement field [C/m^2]	ρ = mass density [kg/m^3]	R_x = torus thickness [m]	S_{ource} = generic power source [W/m^3]
Φ = magnetic flux [W$_b$]	ρ_0 = equilibrium density [kg/m^3]	R = torus mean radius [m]	Q_{wall} = wall heat transfer [W/m^3]
$\boldsymbol{E}$ = electric field vector [V/m]	p = pressure [Pa]	S = duct cross section [m^2]	N = interaction parameter
$\boldsymbol{F}$ = body force vector [N]	η = dynamic viscosity [Pa·s]	Σ = core cross section [m^2]	A_{lfven} = Alfvén number
$\boldsymbol{J}$ = current density vector [A/m^2]	ζ = bulk viscosity [Pa·s]	V_{ol} = volume [m^3]	H_a = Hartmann number
$\boldsymbol{J_e}$ = external current density [A/m^2]	$\boldsymbol{\tau}$ = stress tensor [N/m^2]	A_D = gas-plate interface [m^2]	**l** = circuitation unit vector
$\boldsymbol{J_i}$ = induced current density [A/m^2]	R_{spec}= gas specific constant [J/(kg·K)]	β = ratio between the gas-plate interface and the surface of the internal wall of the duct corresponding to the plate	**i** = axial unit vector
$\boldsymbol{I}$ = current intensity vector [A]	T = temperature [K]	d_{elta} = mean distance between the cloud of charge carriers and the surface of the plate [m]	**r** = radial unit vector
q = charge [C]	k = thermal conductivity [W/(m·K)]	δ = distance between two contiguous sheets of the capacitor plates [m]	$\boldsymbol{p_p}$ = particle position vector
σ = electric conductivity [S/m]	γ_{heat} = heat capacity ratio	y = ratio between the capacitor plates thickness δ and the viscous boundary layer	γ = variance of the Gaussian function
K = load factor	C_p = heat capacity at constant pressure [J/(kg·K)]	l = length of the capacitor's plate [m]	λ = mean value of the Gaussian function
V_0 = open circuit voltage [V]	R_e = fluid dynamic Reynolds number	L = length of the torus [m]	β_{eta} = ratio between plasma dynamic pressure and magnetic field pressure
ρ_q = volume charge density [C/m^3]	P_r = Prandtl number		C_d = thrust coefficient
σ_q = surface charge density [C/m^2]	δ_v = viscous boundary layer [m]		r$_{Li}$ = ion Larmor radius
λ_q = linear charge density [C/m]	δ_{th} = thermal boundary layer [m]		
ε_0 = vacuum electric permittivity [F/m]	c = sound speed [m/s]		
ε = electric permittivity [F/m]	s = shear wave number		
μ_0= vacuum magnetic permeability [H/m]	m_p = particle mass [kg]		
	M = total mass [kg]		
	P_L = viscous losses [W]		

μ = magnetic permeability [H/m] R_m= magnetic Reynolds number μ_e= electric mobility [m^2/ (V·s)] E_ρ= charge distribution electric field [V/m] E_C= externally applied electric field [V/m] E_R= armature reaction electric field[V/m] $\boldsymbol{U}$ = armature reaction voltage drop [V] Q_{tot} = total charge [C] n = number of coil turns $n_{density}$ = number density [m^{-3}] i = coil current [A] I = ionic current [A] **I_{disp} = displacement current [A]** V = applied voltage [V] V_{coil} = induced voltage [V] R_{el} = electric resistance [Ω] C = electric capacitance [F] P_0 = electric power [W] f = frequency [Hz] ω = angular frequency [rad/s] C_D = capacitance - gas-plate system [F] K_B = Boltzmann constant	S_{block} = MPS blocking area [m^2] L_{ssd} = sub solar distance [m]		

Thesis outline

The thesis is organized as follows.

In the introductive section (chapters 1 and 2) an overview of the state of the art about classical MHD energy conversion systems is given by highlighting their main drawbacks.

Subsequently, a brief description about the MHD mathematical model is reported.

Then, the main focus of the thesis is framed. The characteristics of MHD devices are pointed out as optimal for the fulfilment of the major requirements of on-board energy conversion and propulsion systems for Space applications.

In PART I (chapters 3, 4 and 5) two different concepts of MHD inductive generator are proposed aiming overcoming the main drawbacks of conventional MHD generators, but at the same time holding all their advantages, such as the static conversion of the energy and the capability to work with very high temperatures.

Chapter 3 deals with the Flowing MHD Induction generator (3.1), its working principle (3.2) and the implementation of a mono-dimensional mathematical model of the electromagnetic part of the system (3.3, 3.4, and 3.5). Then a sensitivity analysis of the performance of the system is reported (3.6) and the previously introduced model is used performing a preliminary dimensioning of the generator (3.7).

Chapter 4 deals with the TA-MHD Induction generator and its operation.

In 4.2.1 the physics behind the thermoacoustic section functioning is briefly introduced.

In 4.2.2 the main characteristics of MHD section are described and then a first theoretical study, developed in order to perform a coarse sizing and to estimate the performance of the generator for a given set of parameters, is illustrated (4.2.2.1).

A series of FEM simulations is depicted. First of all, an Acoustic analysis (4.2.2.2) shows velocity and pressure profiles inside the generator, confirming the ones reported in literature. Then an Electrostatic analysis (4.2.2.3) was performed in order to study the electrostatic behavior of the charges inside the generator. Moreover (4.2.2.4), a multi-physics analysis is implemented with the aim to perform a preliminary assessment of the behavior of the unbalanced charge carriers when they are subject to an acoustic vibration and to an external electric field.

Finally, in 4.2.2.6, the fully vector Multi-objective Tabu Search (MO-TS) algorithm proposed in [20] [22] has been customized in order to investigate the optimal design of the MHD section of the Thermo-Acoustic Magneto-Hydro-Dynamic electric generator.

Chapter 5 summarizes some conclusions about the first part of the thesis.

In PART II (chapter 6) a new concept of Space propulsion, the Magneto Plasma Sail (MPS), is introduced. This propulsion system is able to thrust a spacecraft by exploiting the energy of the solar wind.

In sections 6.1 and 6.2 the historical evolution of solar sail propulsion concept is shortly depicted.

In section 6.3 an analytical performance estimation as reported in literature is proposed.

In section 6.4 a comparison of the MPS concept with existing space propulsion technologies is performed.

In section 6.5 the state of the art about numerical simulation and experiments is reported.

In section 6.6 and 6.7a FEM analysis of the magnetic sail formation and inflation is conducted, some results and comments are reported.

MHD energy conversion

1 Introduction

The need to improve efficiency and reliability of known energy conversion processes and to effectively exploit new sources of energy pushes the research towards the use of direct conversion systems. There is talk of direct conversion when primary or secondary energy is directly converted into electrical energy, without requiring a passage through an intermediate stage of mechanical energy. When the conversion process takes place directly, rather than going through several steps, it is likely to be more efficient.

The direct conversion methods are of high interest for industrial applications and applied research. Some examples are:

- Photovoltaic power generation (photovoltaic solar cells) [66]
- Electrochemical conversion (fuel cells [74])
- Magnetohydrodynamic generation (MHD [48] [61] [62])
- Thermionic conversion ([37]).

In the first two mentioned systems, the step through the thermal energy is avoided, and they realize the actual direct conversion of primary energy into electrical energy. This represents a great advantage, because a significant loss characterizes the conversion heat into mechanical energy.

2 Classical MHD power generation

The MHD generation process realizes the thermoelectric conversion without any solid moving part, such as turbines and piston-engines. In conventional MHD generators [4] [33] [45] [55] [63] [67] [73] [75] a plasma flow goes through an intense magnetic field, so that, by closing the circuit on a load, the induced electromotive force determines an electric current in the fluid [48].

Interest in magneto hydrodynamic (MHD) power generation was originally stimulated by the fact that the interaction of a plasma flow with a magnetic field could occur at much higher temperatures than what is possible in a rotating mechanical turbine [61] [62].

The absence of moving mechanical parts, as well as reducing losses, allows the device to sustain very high temperatures, thereby increasing, at least potentially, the efficiency. This will lead to

lower consumption of primary energy and to a lower investment per unit of installed power. Furthermore, the mixing of combustion gases with cold gas to cut down the temperature is no longer necessary, therefore the total flow rate is limited and, as a consequence, the size and the global cost of the power plant are reduced too.

The classic MHD generator [48] is a device that generates electricity due to the interaction of a flowing fluid (typically an ionized gas or plasma, but also a liquid metal) with a magnetic field.

The principle of MHD generation is simple, is based on the Faraday's law of electromagnetic induction, according to which when the flow of a magnetic field through the surface bounded by an electrical conductor is variable in time or when the electrical conductor is moving with respect to a constant magnetic field, an electromotive force is induced in it. This is also the operation principle of the conventional electric generators, where the conductors of primary and secondary windings are solid (copper) and move thanks to a mechanical device in a direction orthogonal to the magnetic field.

In MHD generators (Fig. 1) the primary windings are replaced by a gaseous conductor; the motion of the ionized fluid determines an ionic current which, interacting with the magnetic field, generates electricity. The gas is directed inside a nozzle (duct convergent or convergent-divergent depending on the subsonic or supersonic regime) perpendicular to an imposed magnetic field; this leads to a gas expansion in a similar way to what occurs in a conventional gas turbine generator. In turbo generators, the gas expands interacting with the surfaces of the blades, driving the turbine and the coaxial electric generator. In MHD systems the gas kinetic energy is converted directly into electrical energy during the expansion, thanks to the presence of the magnetic field. If the gas flows at high speed through a powerful magnetic field (Fig. 1), each charged particle (with charge q and velocity $\boldsymbol{v}$) will be subject to a magnetic force, the so called Lorentz force or Laplace force $\boldsymbol{F}$:

$$\boldsymbol{F} = q\boldsymbol{v} \times \boldsymbol{B} \qquad (2—1)$$

The positive charges are forced in a direction perpendicular to the plane, identified by the directions of the magnetic field and of the charge motion, whereas the negative charges are forced in the opposite direction. Two electrodes immersed in the fluid, arranged perpendicularly with respect to both its flow and to the magnetic field and positioned on opposite walls of the duct, intercept the charged particles providing an interface with the external circuit, obtaining a source of direct current, with density $\boldsymbol{J}$.

$$\boldsymbol{J} = \sigma(\boldsymbol{v} \times \boldsymbol{B}) \qquad (2—2)$$

where σ is the electric conductivity. The produced electric energy, net of losses, is equal to the reduction of enthalpy of the fluid stream.

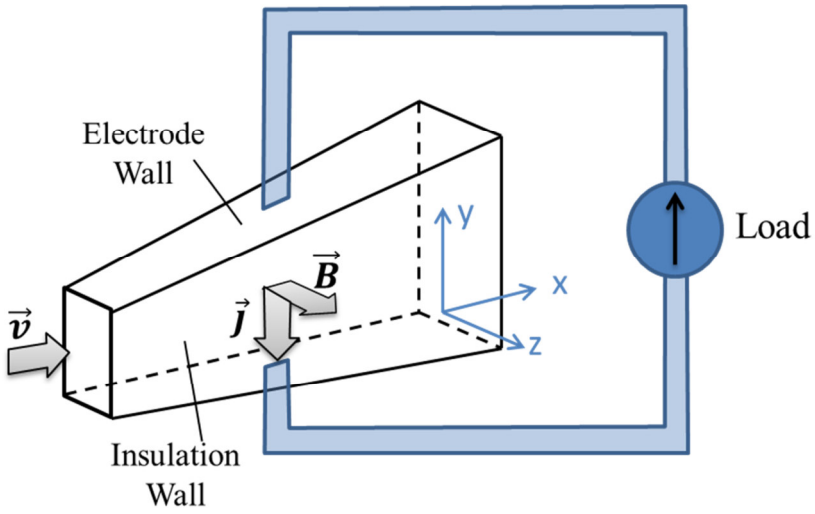

Fig. 1. MHD generator: operating diagram

Conversely, one can obtain a MHD propulsion system by applying a potential between the electrodes, which will circulate a current in the plasma in the direction perpendicular to the field $\boldsymbol{B}$, forcing the plasma itself to move.

The power of an MHD generator for each cubic meter of the channel volume is given by [48]:

$$P_{el} = J \cdot V_0 = \sigma \cdot v^2 \cdot B^2 \cdot K(K-1) \qquad (2—3)$$

where $K = \frac{V_0}{E_{ind}} = \frac{V_0}{(v \cdot B)}$ is the load factor (ratio between open-circuit voltage and induced voltage). It can be noted that, due to the fact that the current density flowing through the load and the open circuit voltage are aligned, the product between $\boldsymbol{J}$ and V_0 is a product between modules. Therefore, the power is proportional to the electrical conductivity, to the square of the gas velocity, and to the square of the intensity of the magnetic field. In order to reach a competitive operability with existing electric generators, the MHD system needs to have a high conductive gas, at high temperature, high speed, compatibly with the increase of the turbulence, and an extremely intense magnetic field (5-7 Tesla), coherently with the costs for the necessary superconducting magnets.

Typically, an electrically conductive high-pressure gas is produced by combustion of fossil fuels. Unfortunately, the most common gases do not ionize significantly at temperatures obtainable through chemical reactions with fossil fuels. This requires to dope the hot gases with small amounts

of easily ionisable materials, such as the alkali metals [48]. Materials such as potassium and cesium have so low ionization potentials that tend to ionize at temperatures achievable by combustion in air. Recovery and reuse of doping materials from the MHD channel exhaust system are fundamental both for economic issues and pollution prevention.

Consequently the widespread and most efficient application of the MHD generator is as the head stage of a coal fueled or a natural gas fueled thermal plant, in a combined cycle with conventional steam plants. Under these conditions the 40% efficiency of a conventional steam plant, could be improved until reaching values of around 60% [40]. There is talk of open-loop systems, because the exhaust is released into the atmosphere at end of the cycle. Higher efficiencies, up to 65-70%, can be obtained through a triple combined cycle, which includes a top MHD stage, followed by a gas turbine and finally a steam turbine [53].

The combined operation with nuclear fission reactors is taken into great consideration in the development of propulsion and power systems for aerospace travels, because it turns out to be the only system capable of providing enough energy for long time missions. In this case we speak of a closed cycle systems, because the working fluid, which acquires heat from the nuclear reaction and then partially loses it in the MHD channel and subsequently in the steam cycle, is a noble gas (helium or argon) which is continuously recycled for economic reasons.

In order to overcome the technologic limits associated with the very high temperatures, as for example the rapid deterioration of the electrodes which are immersed directly in plasma [34] [43], alternative approaches, which allow to operate at lower temperatures, were developed. One of these involves the use of liquid metal (mercury, sodium or potassium), replacing the plasma as charge carrier [38]. The liquid metal has a conductivity many orders of magnitude higher than a plasma, then a MHD plant using liquid metal can be much smaller and consequently have a significantly less cost. This kind of generator is particularly suitable for small powers, which moreover constitutes its main limitation.

Magnetohydrodynamics is involved in several engineering issues, such as the plasma confinement in nuclear fusion reactors [79] and the instability of the liquid coolant (e. g. liquid sodium) in nuclear fission reactors [42]. It is also widely used in the metallurgical industry for pumping and controlled deposition of metals (electromagnetic casting) [31]. Another interesting

idea is to use as conductive medium salt water in order to obtain a silent propulsion system for ships and submarines (first prototype: Yamato1 built by the Japanese in 1991; Fig. 2).

Fig. 2. Yamato 1 at Kobe maritime museum, built by Mitsubishi Heavy Industries [77]

A number of drawbacks have strongly limited the extensive use of this kind of generators:

A. The need of superconducting coils, to generate the required intense magnetic field (about 5 [T]) [61] [62];
B. The rapid deterioration of the electrodes, which retrieve the electric current from the plasma [34] [43];
C. The high enthalpy content of the exhaust gas, because the conductivity is guaranteed only at high temperatures [39];
D. The need for alkaline seeding, which is required to improve the fluid conductivity [46], and the difficulty of retrieving it at the end of the cycle [26].

Even, thanks to the development in different research topics, great improvements have been obtained in the recent years on superconductors [35] and ionized gases [46], the complexity of the apparatus has usually pushed to prefer other competitors, such as turbo gas.

In order to avoid the typical faults of classical MHD generators, liquid metals have been proposed as working fluid [36], but the liquid phase is not advisable to convert heat into other forms of energy, because the absorption of energy is not directly associated to an increase of volume, as it happens for the gases. An important improvement has been proposed in [1]. Here the thermoacoustic effect is combined with a MHD stage. A gas-liquid interface transmits the vibration from the gas to a liquid metal immersed into a magnetic field generated by a permanent magnet, so that, when it vibrates, an induced alternate current circulates in the liquid. Such current induces in

turn an electromotive force into a magnetically linked solenoid connected to the load; therefore, the electrodes are not required (Fig. 3). This technology fixes a number of problems, but others are added, such as adapting the acoustic impedance of the gas-liquid interface and handling liquid sodium.

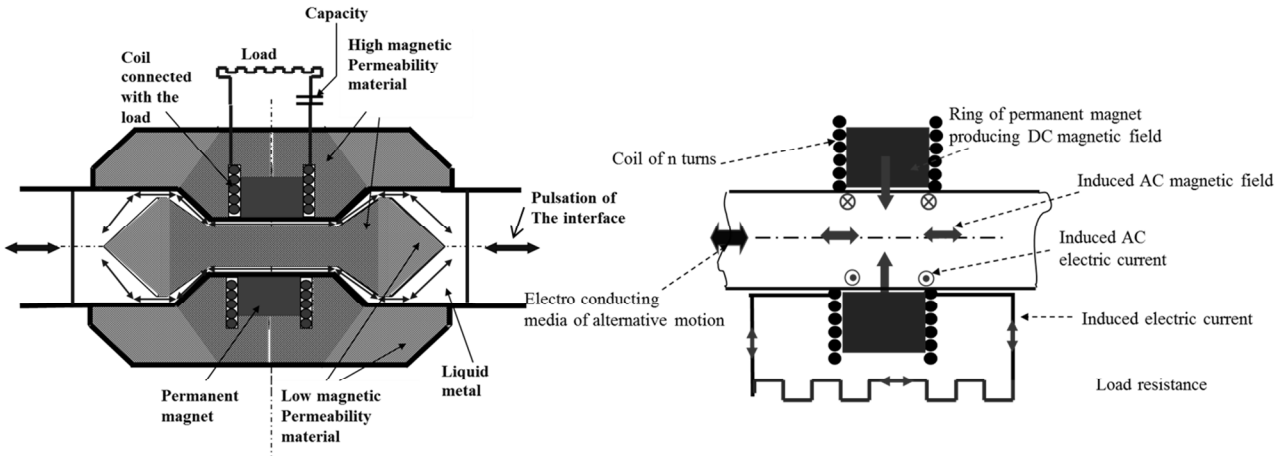

Fig. 3. Liquid Metal Inductive MHD generator: MHD section functioning

In [56] a new technology is proposed, which aims to overcome the above-listed limits. It represents the evolution of the technology presented in [1], with the introduction of new important features: the liquid phase is eliminated for a gaseous working fluid and the exciting external magnetic field is substituted by an electrostatic field. This field is used to separate positive and negative charge carriers, which are created in the working fluid by means of pulsed high voltage electrical discharges. The power will still be transferred to the electric load through the electromagnetic induction.

MHD Mathematical Model

In MHD, as in ordinary hydrodynamics, one of the fundamental hypothesis is the continuum approximation, which states that a fluid might be considered as continuous and described by local properties like pressure and velocity. That approximation is surely acceptable for liquids or gases in collision dominated conditions, where the mean free path of molecules is smaller than the characteristic dimension of the region of interest; it gives sometimes interesting results also for relatively free collision regimes because the tendency of the charges to gyrate around the magnetic field lines gives a local hydrodynamic behavior [64]. In the following, the equations of MHD are introduced; these are the Navier-Stokes equations for fluid mechanics (continuity equation, momentum equation and energy equation); in addition, also the Maxwell equations plus the generalized Ohm's law for electromagnetism are considered. The equations are written considering the plasma as a single fluid, then particle inertia is neglected and ions and electrons are not distinguishable. The equations for fluid mechanics used in MHD are the mass and the momentum conservation equations (see equations (2—4) and (2—5)) with the addition of the electromagnetic force depending on the current density and on the magnetic field (see equation (2—1)):

$$\frac{\partial \rho}{\partial t} + \nabla \cdot (\rho \boldsymbol{v}) = 0 \qquad (2—4)$$

$$\frac{\partial (\rho \cdot \boldsymbol{v})}{\partial t} + \boldsymbol{v} \cdot \nabla (\rho \cdot \boldsymbol{v}) = -\nabla p + \nabla \cdot \boldsymbol{\tau} + \boldsymbol{J} \times \boldsymbol{B} + \boldsymbol{F_v} \qquad (2—5)$$

where ρ is the fluid mass density, p is the pressure, $\boldsymbol{\tau}$ is the stress tensor and $(\rho \cdot \boldsymbol{g})$ the specific gravity force, if $\boldsymbol{g}$ is the gravitational acceleration. The gravitational effects are neglected because the height differences between any pair of points within the systems studied in this thesis are negligible if compared to the weight of the gas. The stress tensor could be expressed by the linear constitutive equation.

$$\boldsymbol{\tau} = \zeta (\nabla \cdot \boldsymbol{u}) \boldsymbol{I_d} + \eta \left(\nabla \boldsymbol{u} + (\nabla \boldsymbol{u})^T - \frac{2}{3} (\nabla \cdot \boldsymbol{u}) \boldsymbol{I_d} \right) \qquad (2—6)$$

where $\boldsymbol{I_d}$ is the identity tensor, ζ is the bulk viscosity and η is the fluid dynamic viscosity. The first term on the left-hand side of equation (2—6) is usually neglected for incompressible fluids or monoatomic gases like noble gases at standard temperature and pressure or, in general, like all the gases at a sufficiently high temperature. Therefore the most general form of the momentum equation for compressible fluids becomes:

$$\frac{\partial(\rho\cdot\boldsymbol{v})}{\partial t} + \boldsymbol{v}\cdot\nabla(\rho\cdot\boldsymbol{v}) = -\nabla p + \eta\left(\Delta\boldsymbol{u} + \frac{1}{3}\nabla(\nabla\cdot\boldsymbol{u})\right) + \boldsymbol{J}\times\boldsymbol{B} \qquad (2—7)$$

The plasma thermodynamic behavior could be described by the ideal gas state equation (2—8) due to the fact that the proposed study deals with noble gases or air at standard temperature and pressure conditions.

$$p = \rho\cdot R_{spec}\cdot T \qquad (2—8)$$

where R_{spec} is the specific gas constant and T its temperature.

The energy transfer could be modeled through a global energy balance:

$$\rho\frac{De}{Dt} = -\nabla\cdot(p\cdot\boldsymbol{u}) + \nabla\cdot(k\nabla T) + \boldsymbol{u}\cdot(\nabla\cdot\boldsymbol{\tau}) + \boldsymbol{J}\cdot\boldsymbol{E} + S_{ource} + Q_{wall} \qquad (2—9)$$

where e is the total energy per volume unit (sum of kinetic and internal specific energy), $k$is the thermal conductivity, $S_{ource}$is a generic internal power source and Q_{wall} is the wall heat transfer per volume unit and time unit. Equation (2—9) will be simplified considering the adiabatic flow assumption:

$$\frac{d}{dt}\left(\frac{p}{\rho^{\gamma heat}}\right) = 0 \qquad (2—10)$$

where $\gamma_{heat} = \frac{C_p}{C_v}$ is the heat capacity ratio between specific heat at constant pressure and specific heat at constant volume. Equation (2—10) is the energy equation written for the simplest possible functioning conditions and could be used replacing the overall energy balance.

In the following, in order to take into account the interaction between electric and magnetic field in the conductive fluid, the Maxwell's equations for electromagnetism (2—11), (2—12), (2—13), (2—14)) with the addiction of the generalized Ohm's law (2—15) are introduced:

$$\nabla\cdot\boldsymbol{E} = \frac{\rho_q}{\varepsilon_0} \qquad (2—11)$$

$$rot\,(\boldsymbol{E}) = -\frac{\partial\boldsymbol{B}}{\partial t} \qquad (2—12)$$

$$\nabla\cdot\boldsymbol{B} = 0 \qquad (2—13)$$

$$rot\,(\boldsymbol{B}) = \mu_0\left(\boldsymbol{J} + \varepsilon_0\frac{\partial\boldsymbol{E}}{\partial t}\right) \qquad (2—14)$$

$$\boldsymbol{J} = \sigma\,(\,\boldsymbol{E} + \boldsymbol{v}\times\boldsymbol{B}\,) \qquad (2—15)$$

where ρ_q is the unbalanced volume charge density, ε_0 is the vacuum electric permittivity and μ_0 is the vacuum magnetic permeability. The second term on the right-hand side of equation (2—14) known as displacement current is a source of magnetic field associated with the time variation of an

electric field. That term could be ignored if the wavelength of the variable electric field is much larger than the typical system dimension or if there are not areas without electrical charge in which the electric field is varying. In the following the displacement current will be neglected. Note that by combining the Maxwell equations with the Ohm's law it is possible to describe the magnetic field behavior by a single equation known as the induction equation (2—16):

$$\frac{\partial \boldsymbol{B}}{\partial t} = rot\,(\boldsymbol{v} \times \boldsymbol{B}) + \frac{1}{\mu_0 \sigma}\Delta \boldsymbol{B} \qquad (2—16)$$

where $\frac{1}{\mu_0 \sigma}$ is the magnetic diffusivity. Hereafter, one of Maxwell's equations or Ohm's law can be replaced by the induction equation, which often can offers advantages in terms of problem resolution, especially for incompressible fluids. The system is closed because comprises seven independent equations ((2—4), (2—7), (2—8), (2—10)) and three equations between (2—12), (2—14), (2—15) and (2—16)) and seven unknowns, $\boldsymbol{v}$, p, T, ρ, $\boldsymbol{B}$, $\boldsymbol{J}$,$\boldsymbol{E}$. In order to bring the electromagnetic problem toward formulations (Laplace, Poisson) with known solutions, an arbitrary solenoidal vector, the magnetic potential vector $\boldsymbol{A}$, is usually defined in such a way that:

$$\nabla \cdot \boldsymbol{A} = 0 \qquad (2—17)$$

$$\boldsymbol{B} = rot\boldsymbol{A} \qquad (2—18)$$

Non–dimensional numbers

In order to perform simulations providing solutions transferable to different scales of magnitude becomes mandatory to work with dimensionless equations. In the following, the absolute variables will be denoted as f, while dimensionless magnitudes will be denoted as f' with respect to the reference variables, denoted as f_0.

By introducing dimensionless variables in the general equations, the following equations are obtained:

$$\frac{\partial \rho'}{\partial t'} + div'\,(\rho' \boldsymbol{v}') = 0 \qquad (2—19)$$

$$\rho' \frac{D\boldsymbol{v}'}{Dt'} = -\nabla'(p') + N(\boldsymbol{J}' \times \boldsymbol{B}') + \frac{1}{R_e}\left(\Delta' \boldsymbol{v}' + \frac{1}{3}\nabla'(\nabla \cdot \boldsymbol{u}')\right) \qquad (2—20)$$

$$\frac{\partial \boldsymbol{B}'}{\partial t'} = rot'(\boldsymbol{v}' \times \boldsymbol{B}') + \frac{1}{R_m}\Delta \boldsymbol{B}' \qquad (2—21)$$

$$rot'\,(\boldsymbol{B}') = R_m \boldsymbol{J}' \qquad (2—22)$$

$$rot'\,(\boldsymbol{E}') = -\frac{\partial \boldsymbol{B}'}{\partial t'} \qquad (2—23)$$

$$p' = \rho'\, R_{spec}\, T' \qquad (2—24)$$

$$\frac{d}{dt'}\left(\frac{p'}{\rho'^{\gamma}}\right) = 0 \qquad (2—25)$$

The four dimensionless numbers (highlighted in red) allow comparing the different physical phenomena involved in the analyzed process [52]; these parameters are:

Reynolds number $R_e = \frac{v_0 L_0 \rho_0}{\eta}$ (2—26)

which is the ratio between inertia and viscous forces;

Interaction parameter $N = \frac{\sigma {B_0}^2 L_0}{\rho_0 v_0}$ (2—27)

which is the ratio of electromagnetic and inertia forces;

Magnetic Reynolds number $R_m = \mu_0 \sigma v_0 L_0$ (2—28)

which is the ratio between (magnetic) convective and diffusive effects (or ratio of diffusion and convection time of a magnetic field in a MHD flow), where L_0 is the characteristic dimension of the studied system; it can be noted that the subscript zero indicates reference quantities.

Frequently, in literature these three non-dimensional numbers may be partially or completely replaced or supplemented by other parameters, which could be expressed as a combination of the previous three:

Alfvén number $A_{lfven}^2 = \frac{R_m}{N}$ (2—29)

which is the ratio of inertia and magnetic forces;

Hartmann number $H_a^2 = \frac{R_e \cdot R_m}{A}$ (2—30)

which is the ratio of magnetic and viscous forces.

Table 1. Summary of the MHD non - dimensional parameters

Symbol	Extended name
R_e	Reynolds number
N	Interaction parameter
R_m	Magnetic Reynolds number
A_{lfven}	Alfvén number
H_a	Hartmann number

If the magnetic Reynolds number is sufficiently high, in the induction equation (2—21) the diffusion term (the second term on the right-hand side of the equation) could be neglected with respect to the convection term, so that the magnetic field is totally linked to the flow (frozen-in magnetic field condition) and its force lines tend to be advected by the fluid. This is equivalent to have a perfectly conducting fluid, so that the induction equation of the so called *Ideal MHD* could be written as follows:

$$\frac{\partial \boldsymbol{B'}}{\partial t'} = rot'(\boldsymbol{v'} \times \boldsymbol{B'}) \qquad (2—31)$$

At the end, the dimensionless system is closed because comprises seven independent equations (from eq. (2—19) to eq. (2—25)) and seven unknown, $\boldsymbol{v'}$, p', T', ρ', $\boldsymbol{B'}$, $\boldsymbol{J'}$, $\boldsymbol{E'}$.

MHD for aerospace

This study concerns the application of MHD to aerospace. This field puts a number of very challenging issues, due to both the severe operating conditions and the requirements for the launching. In fact, on one side the Space vehicles are subject to radiations, are hit by high-energy particles, while the exchange of heat with the environment can be performed only by radiation, which in general requires very large surfaces. On the other side, during the launch, the vehicle undergoes very strong vibrations, which can cause severe damages to the equipment with moving parts, such as pistons and gears, making them unavailable for the mission on the Space. Furthermore, the minimization of mass and volume of the on board devices is a critical aspect of the design.

This holds in particular for the equipment for energy conversion, such as generators of electrical power, active cooling systems, and propulsion systems. Most part of technologies for energy conversion we know require solid moving parts and heavy components, but this makes such systems unsuitable for Space applications. On the other hand, any technology that can do without solid moving parts, which have a high ratio power/volume and power/weight, which have a high efficiency, and finally that can adapt their shape to the vehicle, are preferable for space applications, even in the case the available power is limited.

In the present study, the MHD has been investigated as a candidate for the development of technologies for Space applications. Due to its static nature, the MHD energy converters have the advantage to stand the effect of vibrations during the take-off, can work at high temperatures and with no effects of friction, which guarantee high efficiencies; finally, due to the limited mechanical stresses during the functioning, they can be manufactured by using light materials, with a benefit in terms of load reduction. This study deals with two aspects of the energy conversion in Space vehicles: the production of electric energy to supply the on board electrical devices and the cruise propulsion. Even if the two topics seems to be very far each other, they are associated by the same framework, constituted by the combination of the equations of Fluid-dynamics with that of Electromagnetism, and thanks to the MHD features, they can provide an important stimulus in the field of Space exploration.

PART I

A first part of this thesis is dedicated to the study of a novel technology, which aims to convert thermal energy into electrical energy without mechanical moving parts, dealing with higher temperatures and lower flow rates with respect to gas turbines. The absence of mechanical frictions and wear, and the possibility to deal with polluted gases are further important introduced benefits. The described systems have the peculiarity to overcome the typical drawbacks of the conventional MHD generators, such as the need to operate at high temperatures and to have superconducting coils for the generation of the external magnetic field, but at the same time they hold all their advantages, such as the static conversion of the energy and the capability to work with very high temperatures.

3 Fluent gas MHD induction generator

In [16] [17] [49] [50] [51] [59], an inductive gas-dynamic generator was proposed with the aim to overcome the mentioned drawbacks of the classical MHD generators. This goal was reached by:

1. eliminating the heavy and expensive excitation superconducting coils;
2. introducing an electrostatic field (whose consumption is virtually null) with the goal to split in two separated flows of different sign the free charges in the gas, giving rise to a circulating primary current (current in the gas);
3. using a periodic discharge ionization system in order to generate a time-variant primary current, so that it can give rise to an induced electromotive force in a magnetically coupled coil and to a current in an electrical load (secondary current).
4. exploiting the induction principle only for the conversion from primary to secondary current, rather than for the primary current generation;
5. ionizing the gas through electrical discharges, so that the conductivity does not depend on temperature and a higher enthalpy content of the gas can be exploited.

Even if many of the challenges were solved by this new conceptual design, contemporarily, some new issues were introduced. For example, the charges inside the clouds of the same sign are subject to strong Coulombian repulsive forces, which tend to distribute them axially along the MHD tube. The described effect reduces the time variation of electrical current when it traverses the

magnetic core and, finally, the power transmitted by induction. In [17] some arrangements were proposed in order to address this effect.

In [16] [49] [50] [51] [59], the conceptual idea is described and the energy conversion process is illustrated. A preliminary study on the charge distribution and on the achievable performances is conducted by using the multiphysics approach, with a 2D finite element model which describes fluid dynamic, electrostatic and charge transport aspects of the process. The results from the previous listed studies highlighted that fluid velocity, charge density, electric and magnetic field distribution have no significant variance along the duct cross section, so that a mono-dimensional approach could be used. In [17] a 1D analytical model has been implemented and solved in the Simulink® environment. In this thesis work the influence of some design parameters on the open circuit induced voltage and on the transferred power has been investigated.

3.1 System description

The working principle of the studied generator studied is briefly described in Fig. 4.

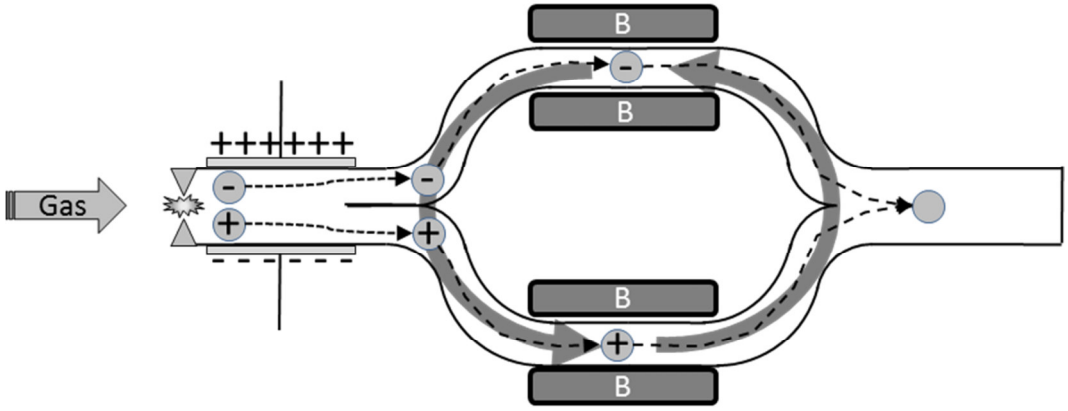

Fig. 4. Fluent gas inductive MHD generator, functional scheme [19]

The device can be divided in three sections. In the first, a gas flow at high speed and high temperature enters in a straight duct where it is ionized by a periodical electric discharge. In the second branch the charge carriers of different sign are separated thanks to an external high voltage electric field through the positioning of properly designed capacitor plates. Downstream of this process, in the third section, the duct splits in two different parallel paths, so that the flow will be divided in two currents with the same direction, one with an excess of positive charge, the other one of negative charge. Therefore, a time varying annular electric current flows between the two branches of the duct (see the dark grey large arrows in Fig. 4). The current generated induces in turn

an electromotive force in two toroidal coils wrapped around the duct. Several design parameters, such as duration, frequency and intensity of discharges, applied electric field, gas velocity and charges' mobility, tend to affect the time-evolution of the electric current inside the fluid (primary current). The energy conversion process takes place in correspondence of the toroidal coils (Fig. 4 and Fig. 5) where, thanks to the time-variance of the ionic current, a varying magnetic flux will interest the ferromagnetic core, so that an electromotive force is induced in the secondary windings and, thus, an electric current (secondary current) is supplied to an electrical load eventually connected.

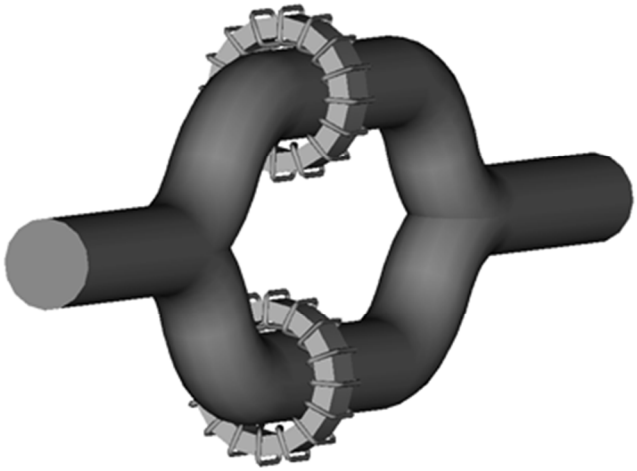

Fig. 5. Inductive MHD generator layout [17]

3.2 Energy conversion process

As previously depicted, the energy conversion occurs in the third section of the generator in correspondence of the toroidal coils, where the primary ionic current is converted into the secondary one supplying the load. The inductive generator behaviour is something like a conventional low quality transformer (current transformer), so that it can be studied by using the concerning well known equations. The primary solid winding is replaced by the plasma flow in the duct, while the secondary is the toroidal coil (Fig. 5). The electric current flowing in the load determines an electric field of armature reaction, which for definition opposes to the cause that generated it, slowing down the charge carriers into the plasma and then causing a gas expansion. Gas velocity, magnetic core geometry, number of loops of the windings and section of the used wire affect, together with a vastness of other design parameters, the achievable enthalpy jump. In this work the variation effect of some of these parameters is investigated.

3.3 System modelling

The MHD problem associated to the functioning of the generator has been faced with a multiphysics approach, by splitting it into an electrostatic part, a fluid dynamic part and a charge transport part, solved separately by means of the finite element analysis and by the use of the commercial software COMSOL® [16] [59]. The generator was considered as it had the secondary winding left open. The solution of the electrostatic model provides electric potential and electric field distributions, while the fluid dynamic one yields the velocity field; the results from these studies are used as input for the charge transport problem. The global results confirm the possibility to split the flow in two streams of charges of opposite sign, allowing to estimate the induced electromotive force in the open secondary winding and the power transferred to a pure resistive load adapted to the theoretical maximum power output. The achievable outlet power has been estimated by varying the electric load and the period between two consecutive ionizing discharges, showing that the device performance decreases with increasing load and discharge time interval. Moreover a sensitivity analysis highlighted the dependence of the induced electromotive force and of the achievable power by the gas velocity and the device geometry.

Afterward [17], in analysing the power transfer process, a mono-dimensional model of the process has been considered neglecting the flow variations over the cross section of the duct. Fig. 6 illustrates a detail of one of the separated branches of the duct.

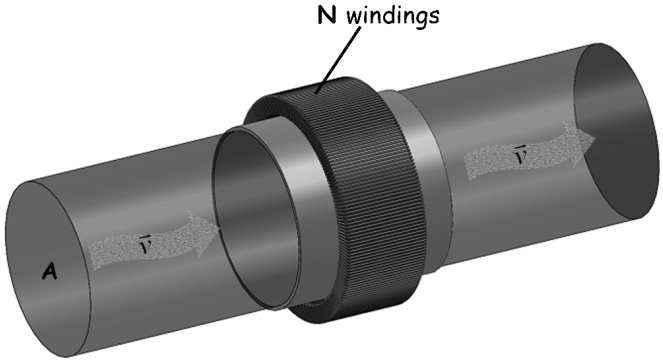

Fig. 6. Detail section of the generator where the energy conversion takes place [17]

A fundamental assumption has been that the charge carriers' concentration is such low that they cannot affect the average motion of the fluid, thus they are dragged at the same velocity of the neutrals. In addition, other two components were introduced, linked respectively to the armature reaction and to the Coulombian force between the charges. The repulsive force tend to spread the charges of the same sign, heavily affecting the transfer of energy, because the more the charges are

distributed, the less will be the time variation of the magnetic flux concatenated with the torus, the less will be the inducted electromotive force in the coil. In [17] has been proposed a supplementary electric field E_c applied by means of a metallic sleeve positioned around the duct (Fig. 6) in order to mitigate the repulsive effect between charges. Summarizing, four components of the velocity was taken into account in calculating the distribution of the charges during the time:

$$v(x,t) = v_T + \mu_e\left[E_\rho(x,t) + E_c(x,t) + E_R(x,t)\right] \qquad (3—1)$$

where v is the velocity of the charged particle in the position x at the time t, v_T is the dragging component, which is the constant velocity of neutrals, μ_e is the electric mobility of the charge carriers, E_ρ is the electric field due to the charges distribution, E_C is the external electrostatic field provided by the sleeve, E_R is the electric field due to the armature reaction. At the beginning of the branch, the charge has a Gaussian distribution, but evolving in the duct such distribution changes, because of the electric fields E_c and E_R, becoming asymmetric. In order to take into account such asymmetry, the combination of two Maxwellian distributions has been used [17] to model the charge density distribution (see Fig. 7):

$$\lambda_q(x) = \left(1 - \frac{x}{D_{ist}}\right) \cdot \frac{4Q_{tot}}{\sqrt{\pi}} \cdot \frac{x^2}{x_m^3} \cdot e^{-\frac{x^2}{x_m^2}} + \frac{x}{D_{ist}} \cdot \frac{4Q_{tot}}{\sqrt{\pi}} \cdot \frac{(D_{ist}-x)^2}{(D_{ist}-x_m)^3} \cdot e^{-\frac{(D_{ist}-x)^2}{(D_{ist}-x_m)^2}} \qquad (3—2)$$

where D_{ist} is the distance between the two ends of the cloud, $\lambda_q(x)$ is the linear charge density, Q_{tot} is the total charge of the cloud, x_m is the abscissa corresponding to the charge density maximum. The proposed distribution is preferable with respect to the Gaussian because it gives the possibility to describe asymmetric distributions.

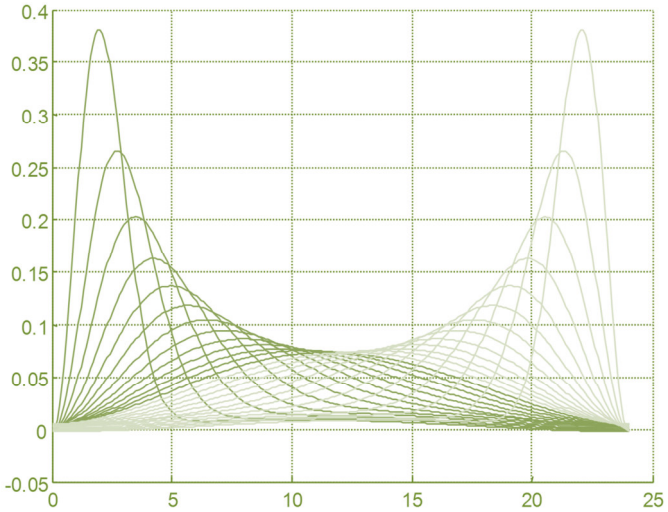

Fig. 7. Charge density distribution

3.4 Electric fields characterization

Given the charge distribution, it is possible to calculate the electric field $E_\rho(x,t)$ in the generic point x on the axis of the duct and then the component of velocity due to such field in (3—1) by integrating the Coulomb law all along the support **of** $\lambda_q(\boldsymbol{x},\boldsymbol{t})$. Under the hypothesis of homogeneous distribution of charges along each cross section, the contribution to the Coulomb field in a point X of the duct axis due to an element of surface charge $d\sigma_q$ (see Fig. 8) could be calculated. For symmetry, only the axial component of the field gives a contribution to the total field, therefore the elementary contribution of $d\sigma_q$ in the point X writes:

$$\boldsymbol{dE_\rho} = \frac{\mathbf{1}}{\mathbf{4\pi\varepsilon}} \cdot \frac{\boldsymbol{d\sigma_q\, d\xi}}{\boldsymbol{\xi^2+\gamma^2}} \cdot \boldsymbol{\cos\alpha} = \frac{\boldsymbol{d\xi}}{\mathbf{4\pi\varepsilon}} \cdot \frac{\lambda_q(\xi)\,\boldsymbol{\gamma\, d\gamma\, d\theta}}{(\boldsymbol{\xi^2+\gamma^2})\cdot\boldsymbol{\pi R_d{}^2}} \cdot \frac{\boldsymbol{\xi}}{\sqrt{\boldsymbol{\xi^2+\gamma^2}}} = \frac{\boldsymbol{d\xi\, d\gamma\, d\theta}}{\mathbf{4\pi^2\varepsilon R_d{}^2}} \cdot \frac{\lambda_q(\xi)\,\boldsymbol{\gamma\,\xi}}{(\boldsymbol{\xi^2+\gamma^2})^{3/2}} \quad (3—3)$$

where ξ is the distance (with sign) along the axis between the cross section of the charge distribution and the point X, $d\sigma_q$ is the element of surface charge, (γ,θ) is the polar system of coordinates in the cross section (Fig. 5), R_d is the radius of the duct.

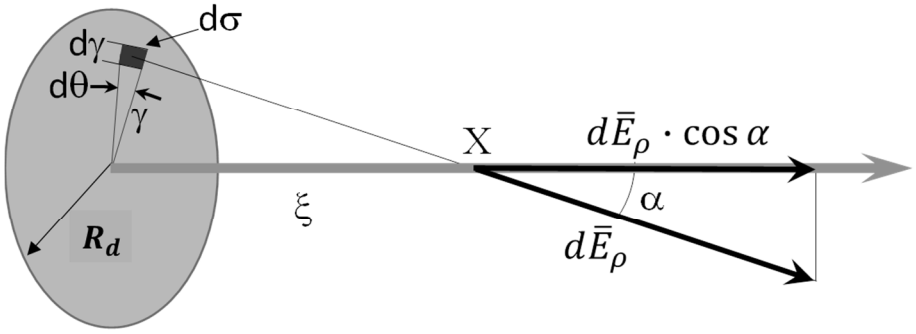

Fig. 8. Coulomb force calculation

The Coulomb field is obtained by integrating over the volume where the charge carriers are confined, obtaining:

$$\boldsymbol{E_\rho} = \frac{\mathbf{1}}{\mathbf{4\pi^2\varepsilon R_D{}^2}} \int_{X-x_1}^{X-x_2} \int_0^{R_d} \int_0^{2\pi} \frac{\lambda_q(X-\xi)\gamma\xi}{(\xi^2+\gamma^2)^{\frac{3}{2}}}\, \boldsymbol{d\theta d\gamma d\xi} = \frac{\mathbf{1}}{\mathbf{2\pi\varepsilon R_D{}^2}} \int_{X-x_1}^{X-x_2} \int_0^{R_D} \frac{\lambda_q(X-\xi)\gamma\xi}{(\xi^2+\gamma^2)^{\frac{3}{2}}}\, \boldsymbol{d\gamma d\xi} =$$

$$= \frac{\mathbf{1}}{\mathbf{2\pi\varepsilon R_D{}^2}} \int_{X-x_1}^{X-x_2} \boldsymbol{\lambda_q(X-\xi)}\, \boldsymbol{\xi} \left[\frac{-1}{\sqrt{\xi^2+\gamma^2}}\right]_0^{R_d} \boldsymbol{d\xi} = = \frac{\mathbf{1}}{\mathbf{2\pi\varepsilon R_D{}^2}} \int_{X-x_1}^{X-x_2} \boldsymbol{\lambda_q(X-\xi)} \left[\frac{\xi}{\sqrt{\xi^2}} - \frac{\xi}{\sqrt{\xi^2+R_D{}^2}}\right] \quad (3—4)$$

By substituting the (3—2) in this integral, we can calculate the Coulomb field in any point of the axis. The calculation is performed by using the integration function *quad(...)* of Matlab®.

The $E_R(x,t)$ field is due the armature reaction and depends on the current circulating in the coil. In order to calculate such field we can use the same mathematical steps which allow demonstrating the Biot-Savart law. Taking into account the definition of the vector potential $\boldsymbol{A}$ (see equation (2—17) e (2—18)) a new vector field $\boldsymbol{C}$ that can be defined as potential vector of the potential vector $\boldsymbol{A}$:

$$\boldsymbol{A} = rot\ \boldsymbol{C} \qquad (3—5)$$

By substituting (3—5) in (2—17), one obtains the following relation between the fields $\boldsymbol{A}$ and $\boldsymbol{C}$:

$$\boldsymbol{B} = rot(rot\ \boldsymbol{C}) \qquad (3—6)$$

The equation (3—5) leaves a degree of freedom in the definition of the field $\boldsymbol{C}$, because the relation admits also adding to $\boldsymbol{C}$ an arbitrary field having divergence equal to zero. In this case the (3—6) can be re-written in the form of a Poisson equation, whose general solution is known:

$$\nabla^2\boldsymbol{C} = -\boldsymbol{B} \Rightarrow \boldsymbol{C} = \iiint_{V_{ol}} \frac{\boldsymbol{B}}{r} dV \qquad (3—7)$$

where V_{ol} is the volume of integration and r is the distance between the two points where the fields $\boldsymbol{B}$ and $\boldsymbol{C}$ are evaluated.

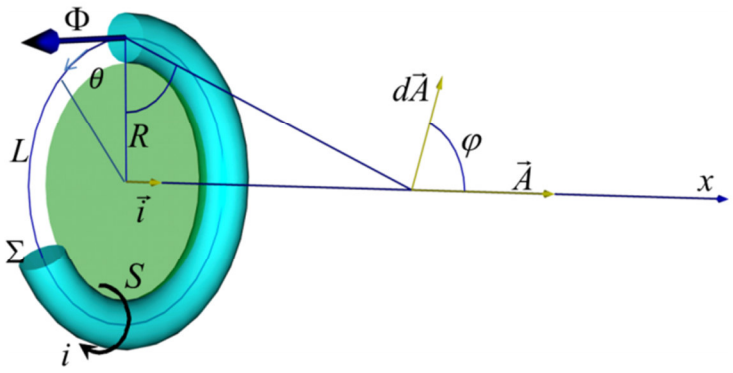

Fig. 9. Main variables of the problem

In the system depicted in Fig. 9, the integral in (3—7) has to be calculated only inside the toroidal core of the coil, which is the only volume where the field $\boldsymbol{B}$ is different from zero. The high permeability of the core makes the $\boldsymbol{B}$ field constant along the core and in each point orthogonal to the normal cross section, therefore the evaluation of the integral in (3—7) can be simplified as in the following:

$$\boldsymbol{C} = \oint_L \frac{\Phi}{r} d\boldsymbol{l} \qquad (3—8)$$

where Φ is the core magnetic flux.

Equation (3—8) gives the possibility to associate to the differential element of length $d\boldsymbol{l}$ of the core, an elementary contribution to the total field $\boldsymbol{C}$ calculated in a general point:

$$d\boldsymbol{C} = \frac{\Phi}{r} d\boldsymbol{l} \qquad (3—9)$$

By combining (3—5) and (3—9) we obtain:

$$rot(d\boldsymbol{C}) = d\boldsymbol{A} = \Phi \cdot \frac{d\boldsymbol{l} \times \boldsymbol{r}}{r^3} \qquad (3—10)$$

The (3—10) allows one to calculate the field $\boldsymbol{A}$ in each point of the space. The (3—10) is formally identical to the Biot-Savart equation, so that the force lines of electric field generated by the magnetic flux have the same shape of the magnetic field generated by a turn of electrical current, and it allows to calculate the electric field along the axis of the duct, which represents the armature reaction. For symmetry, the resultant potential vector $\boldsymbol{A}(x)$ is directed as the axis of the duct, so that integrating the contributions $d\boldsymbol{A}$ due to the flux along the torus, we have to consider their projection along the axis *x*:

In particular, in the generic point of the axis of the duct it results:

$$\boldsymbol{A}(x) = \int_0^{2\pi} \Phi \frac{d\boldsymbol{l} \times \boldsymbol{r}}{r^3} = \left(\int_0^{2\pi} \frac{\Phi \cdot \sqrt{(\boldsymbol{R}^2 + x^2)}}{\left(\sqrt{(\boldsymbol{R}^2 + x^2)}\right)^3} \cdot cos\,\varphi \cdot \boldsymbol{R} \cdot d\theta \right) \cdot \boldsymbol{i} =$$

$$= \frac{\Phi \cdot \sqrt{(\boldsymbol{R}^2 + x^2)}}{\left(\sqrt{(\boldsymbol{R}^2 + x^2)}\right)^3} \cdot \frac{\boldsymbol{R}}{\sqrt{(\boldsymbol{R}^2 + x^2)}} \cdot \boldsymbol{R} \cdot \int_0^{2\pi} d\theta = \frac{2\pi \cdot \Phi \cdot \boldsymbol{R}^2}{\left(\sqrt{(\boldsymbol{R}^2 + x^2)}\right)^3} \cdot \boldsymbol{i} \qquad (3—11)$$

By deriving the (3—11), we can calculate the electric field in a point of the axis:

$$\boldsymbol{E_R} = -\frac{\partial \boldsymbol{A}}{\partial t} = -\frac{2\pi \mathrm{R}^2}{\left(\sqrt{\mathrm{R}^2 + x^2}\right)^3} \cdot \frac{d\Phi}{dt} \cdot \boldsymbol{i} \qquad (3—12)$$

where R is the mean radius of the torus and x is the abscissa along the axis referred to the center of the torus. The value of the field in the center of the cross section is assumed for the whole section, so that it can be expressed in scalar terms. This electric field, due to its origin, is always opposite to the fluid flow, and then it brakes the charges in the gas. Through this mechanism, the gas loses the part of enthalpy that is yielded to the electric load.

At the end, equation (3—4) and (3—12) can be substituted in equation (3—1) allowing to determine the global velocity of the charged particle.

3.5 Power transfer to the electric load

In [17] [18] the energy conversion process has been described by resorting to the Ampère equation, written for the symmetry plane of the torus, which is orthogonal to the axis of the duct:

$$\oint_L \boldsymbol{H} \cdot d\boldsymbol{l} = I - n \cdot i + \varepsilon \frac{d}{dt} \iint_S \left(E_\rho + E_R\right) dS \qquad (3—13)$$

where L is the length of the revolution axis, $\boldsymbol{H}$ is the magnetic field inside the core, I is the current intensity in the gas, n is the number of the coil turns, i is the current circulating in the coil, ε is the permittivity and S is the cross section of the duct. As it can be seen, field E_C does not appear in the displacement current term, because it is null in the origin for symmetry reasons. On the other hand, it implicitly affects the current I by influencing the charge distribution $\lambda_q(\boldsymbol{x}, \boldsymbol{t})$.

If the magnetic flux density $\boldsymbol{B}$ is assumed to be constant in the cross section of the torus (no edge effect) and along the torus (homogeneous material and constant cross section), the circulation integral at the left-hand side can be re-written as:

$$\oint_L \boldsymbol{H} \cdot d\boldsymbol{l} = \oint_L \frac{\Phi}{\mu \cdot \Sigma} dl = \frac{\Phi \cdot L}{\mu \cdot \Sigma} \qquad (3—14)$$

where μ is the magnetic permeability and Σ is the cross section of the core.

The current I in the right-hand side of (3—13), is given by the concentration of charge λ_q given by the (3—2), evaluated in the origin and then multiplied by the charge velocity (3—1):

$$I = \lambda_q(x,t)_{x=0} \cdot \left\{ v_T + \mu_e \left[E_\rho(x,t) + E_R(x,t) \right]_{x=0} \right\} \qquad (3—15)$$

The current i circulating in the winding is related to both by the Ohm's law. For the sake of simplicity, the electric load is assumed to be purely resistive. Then the current i can be so expressed:

$$i = \frac{V_{coil}}{R_{el}} = \frac{1}{R_{el}} \cdot \frac{d(N \cdot \Phi)}{dt} = \frac{N}{R_{el}} \cdot \frac{d\Phi}{dt} \qquad (3—16)$$

where V_{coil} is the induced electric voltage and R_{el} the electric load.

The second term of the right-hand side of equation (3—6) becomes:

$$-N \cdot i = -\frac{N^2}{R_{el}} \cdot \frac{d\Phi}{dt} \qquad (3—17)$$

Finally, the third term, corresponding to the displacement current due to the time variation of the electric field in the origin, in the hypothesis of homogenous distribution, writes as:

$$\varepsilon \frac{d}{dt}\iint_S (E_\rho + E_R)dS = \varepsilon \frac{d(E_\rho+E_R)_{x=0}}{dt}\iint_S dS = \varepsilon \cdot S \cdot \frac{d(E_\rho+E_R)_{x=0}}{dt} \qquad (3—18)$$

The contribution of E_R to the displacement current could be obtained deriving the (3—12). In a first approximation the terms with second order derivatives have been neglected, therefore only the Coulomb component (linked to the charge distribution) of the displacement current is considered:

$$\boldsymbol{I_{disp} = \varepsilon \cdot S \cdot \frac{dE_\rho(0,t)}{dt} = \frac{\varepsilon \cdot S}{2\pi\varepsilon R_d^2}\frac{d}{dt}\int_{-x_1}^{-x_2} \lambda_q(-\xi)\left[\frac{\xi}{\sqrt{\xi^2}} - \frac{\xi}{\sqrt{\xi^2+R_d^2}}\right]d\xi =}$$

$$\frac{S}{2\pi R_d^2}\left\{\int_{-x_1}^{-x_2}\frac{\partial\lambda_q(-\xi)}{\partial t}\left[\frac{\xi}{\sqrt{\xi^2}} - \frac{\xi}{\sqrt{\xi^2+R_d^2}}\right]d\xi - v_2\lambda_q(x_2)\left[\frac{-x_2}{\sqrt{{x_2}^2}} - \frac{-x_2}{\sqrt{{x_2}^2+R_d^2}}\right] + v_1\lambda_q(x_1)\left[\frac{-x_1}{\sqrt{{x_1}^2}} - \frac{-x_1}{\sqrt{{x_1}^2+R_d^2}}\right]\right\} \qquad (3—19)$$

where $v_1(t)$ and $v_2(t)$ are the velocities of charge carriers at the ends of the charges cloud.

On the other hand, the two terms where the velocities appear are multiplied by the charge density at the ends, which is null by definition. Therefore, the term of the displacement current reduces to:

$$\boldsymbol{I_{disp} = \frac{S}{2\pi R_d^2}\int_{-x_1(t)}^{-x_2(t)}\frac{\partial\lambda_q(-\xi)}{\partial t}\left[\frac{\xi}{\sqrt{\xi^2}} - \frac{\xi}{\sqrt{\xi^2+R_d^2}}\right]d\xi} \qquad (3—20)$$

As for the case of the calculation of the Coulomb force, the integral of the displacement current is calculated numerically by using Matlab®.

By substituting (3—1), (3—2), (3—4), (3—12), (3—14), (3—15), (3—16), (3—20) in (3—13), we obtain an equation of the second order in the variable Φ. By assuming negligible the contribution due to the reaction field E_R in (3—18), the equation for the Simulink® model implementation writes:

$$\left[\frac{2\pi\cdot\lambda_q(0,t)\cdot\mu_e}{R_d} + \frac{N^2}{R_{el}}\right]\frac{d\Phi}{dt} + \frac{L}{A\cdot\mu}\Phi =$$

$$= \lambda_q(0,t)\cdot v_T - \frac{1}{2}\int_{x_1(t)}^{x_2(t)}\left[\frac{\lambda_q(0,t)\cdot\mu_e}{2\pi R_d^2\varepsilon}\lambda_q(\xi) + \frac{\partial\lambda_q}{\partial t}\right]\left(\frac{\xi}{\sqrt{\xi^2}} + \frac{\xi}{\sqrt{\xi^2+R_d^2}}\right)d\xi \qquad (3—21)$$

where ξ is the distance along the axis between the cross section coincident with the charge distribution and the considered point.

Table 2. Sensitivity analysis: Design parameters of the MHD generator [18]

Physical quantity	Symbol	Value [units]
Linear charge density	λ_q	[C/m]
Radius of duct	R_d	0.20 [m]
Permittivity	ε	$10^{-9}/36\pi$ [F/m]
Charge in the duct		10^{-5} [C]
Permeability	μ	0.0628 [H/m]
Gas velocity	v_T	150-200 [m/s]
Ions mobility	μ_e^+	$2 \cdot 10^{-4}$ [$m^2/(V \cdot s)$]
Electrons mobility	μ_e^-	$3 \cdot 10^{-2}$ [$m^2/(V \cdot s)$]
Length of the sleeve		0.20 [m]
Charge on the sleeve		10^{-5} [C]
Length of the torus	L	1.4 [m]
Cross area of the torus	Σ	$2 \cdot 10^{-2}$ [m^2]
Number of coil turns	N	2000
Electric load	R_{el}	100-2000 [Ω]

3.6 Sensitivity analysis

Table 2 summarizes the design parameters used for the simulation of the generator. The model equation has been solved with a first implementation in Simulink® environment [18]. The velocity of the working gas and the electrical load has been swept in order to evaluate the relative sensitivity with respect to voltage and transferred power [18]. The results (Fig. 10) show that the higher the velocity and the electric load are, the higher the achievable power will be and that the higher the velocity, the higher the induced voltage. A fundamental challenge to face is the estimation of the time needed to cross the toroidal windings for the whole cloud of charges. This value has to be taken into account for the choice of the right periodicity for the ionizing discharge. The simulations shown that a gas velocity of 150 [m/s] is sufficient to drag the charges beyond the torus. The time needed for the charges to cross the toroidal coil could be calculated by knowing both gas velocity and total charge. The duration of the pulse of the induced voltage indicates the minimum time interval between two consecutive discharges.

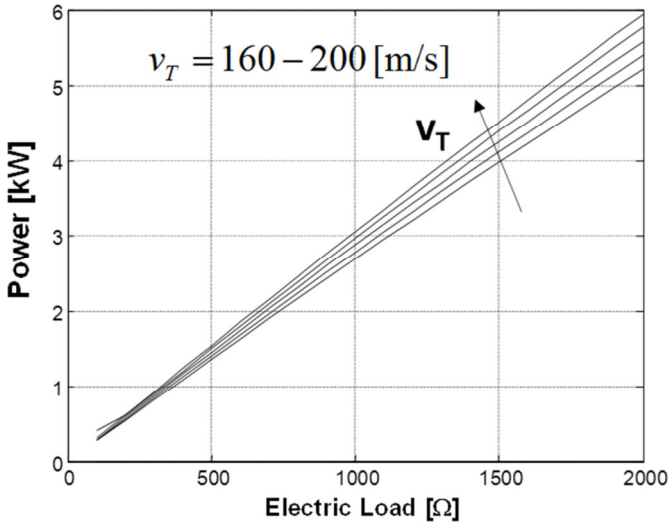

Fig. 10. Power trend with respect to load and velocity [18]

3.7 Dimensioning of the generator

In this thesis, the previously introduced mono-dimensional model [17] [18] [19] has been customized in order to perform a preliminary dimensioning of the MHD inductive generator in Simulink® environment.

The model equation (3—21) is a first-order differential equation in the magnetic flux Φ. The right-hand side is the sum of three contributions; the former one is due to the dragging of charges by the neutrals, the second one is due to the electric field generated by the charges' distribution while the latter is due to the armature reaction field and depends on the current circulating in the coil. The left-hand side of the equation gives some preliminary indications on the dimensioning of the parameters:

1. in order to maximize the converted power, the induced voltage applied to the electrical load will be maximized;
2. the coefficient of the first-order term grows with the square of N, therefore a large number of turns will produce a limited power conversion;
3. a large value of the electric load R_{el} will cause a reduction of that coefficient, but the power will be also reduced, therefore a compromise solution is mandatory;
4. the increasing radius of the torus R has a benefit for the reduction of the coefficient but, at the same time, the reluctance of the magnetic core increases with the radius, therefore also in this case a crossover value has to be determined;

5. the electrical mobility μ_e has in general a negative effect on power conversion, mainly because it spreads the charge carriers along the duct, reducing the induction effect.

Table 3. Dimensioning: Design parameters of the MHD generator [19]

Physical quantity	Symbol	Value [units]
Radius of duct	R_d	0.10 [m]
Permittivity	ε	$10^{-9}/36\pi$ [F/m]
Charge in the duct	Q_{tot}	10^{-3} [C]
Permeability	μ	0.0628 [H/m]
Gas velocity	v_T	1000 [m/s]
Ions mobility	μ_E^+	$2 \cdot 10^{-4}$ [m^2/(V·s)]
Length of the torus	L	1.25 [m]
Cross area torus	A	0.4 [m^2]
Number of coil turns	N	30
Electric load	R_{el}	3 [kΩ]

The following figures show the simulation results, showing respectively the time evolution of charge distribution along the duct (Fig. 11), of the voltage applied to the electrical load (Fig. 12) and of the transmitted power (Fig. 13).

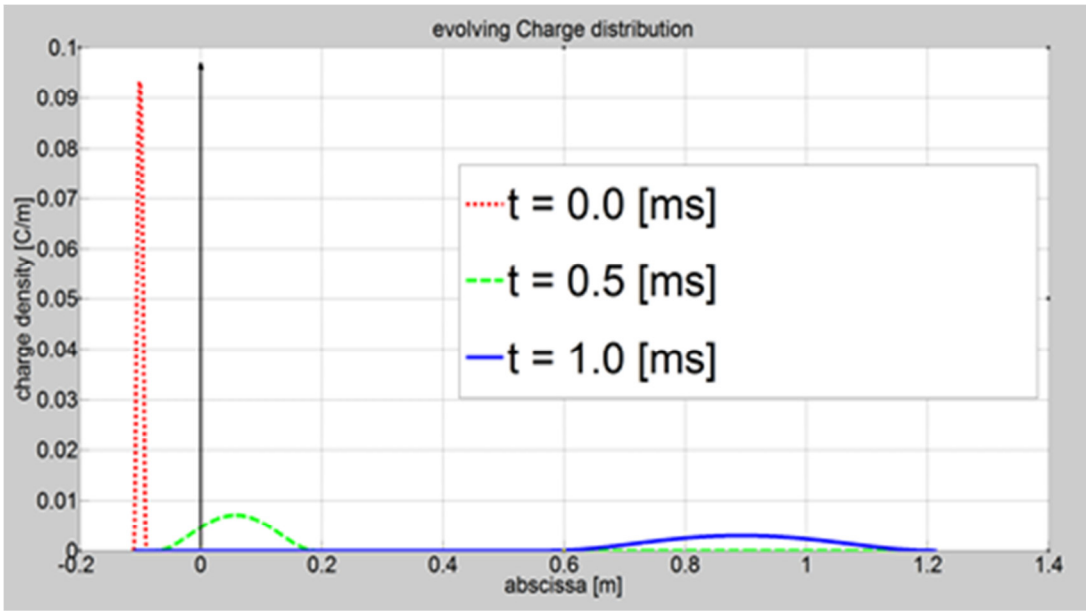

Fig. 11. Time evolution of charge distribution

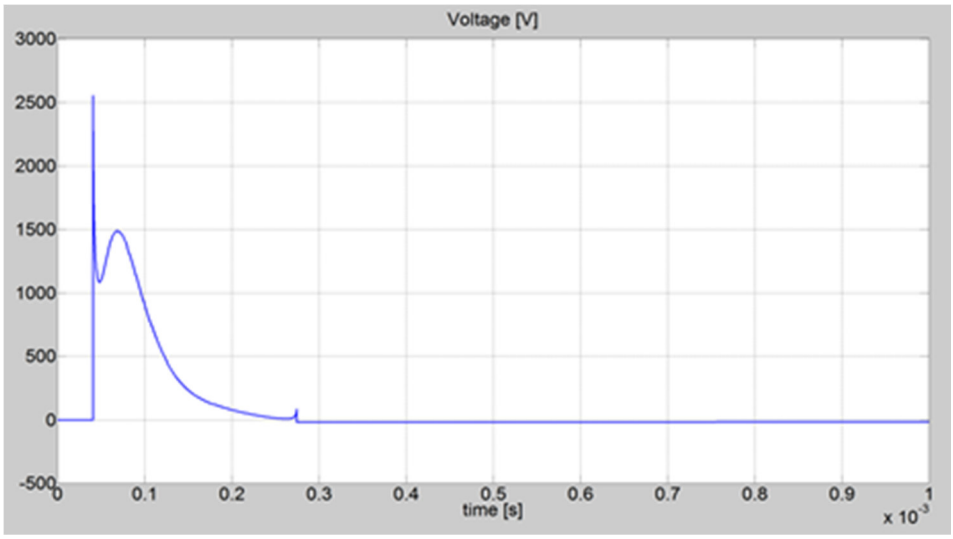

Fig. 12. Time diagram of the voltage

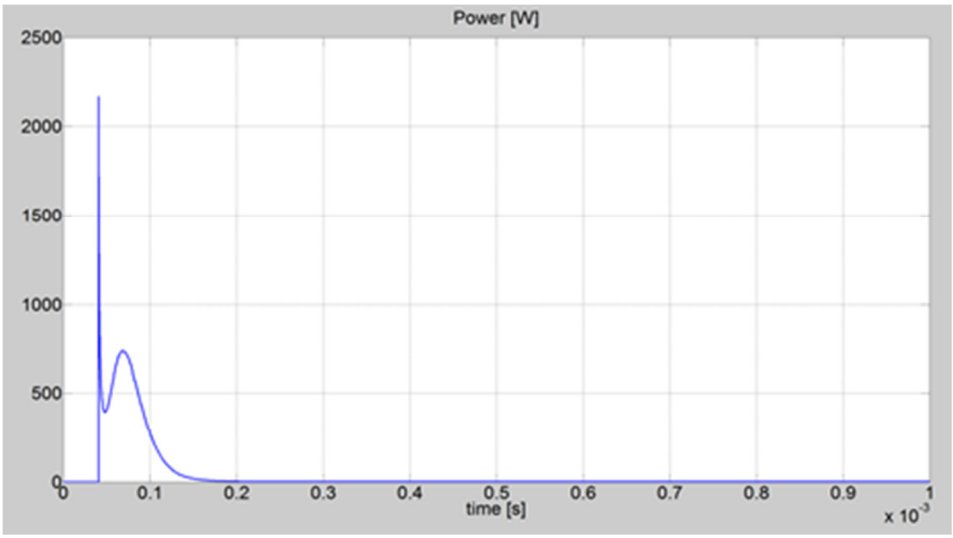

Fig. 13. Time diagram of the power

What clearly emerges from and is that the active time is very short (less than 0.3 [ms]), but considerable values of voltage (Fig. 12) and power (Fig. 13) are reached. On the other hand, the time necessary to clean the duct from the charge carriers is much longer, because the thrust of repulsive force is very strong, especially when the charge is much concentrated (see Fig. 11). After a time of 0.5 [ms] the cloud of charges have not still totally overtaken the zero abscissa, corresponding to the toroidal coil, so that the feasible time-rate of the ionizing discharges have to be chosen carefully in order to avoid interferences between consecutive clouds. This at the end affects also the average power produced by the generator.

If the pressure is an adequate level when at the exit of the diaphragm the exhaust gas is neutralized (Fig. 4), it can undergo a new stage of conversion. The global achievable power will be the sum of the power retrieved in all the cascade stages.

The results of the simulation are in good agreement with the expected behavior of the generator.

3.8 Simulink® Model implementation

In Fig. 14 the schematics of the implementation in Simulink® environment of the mono-dimensional model of the generator is depicted:

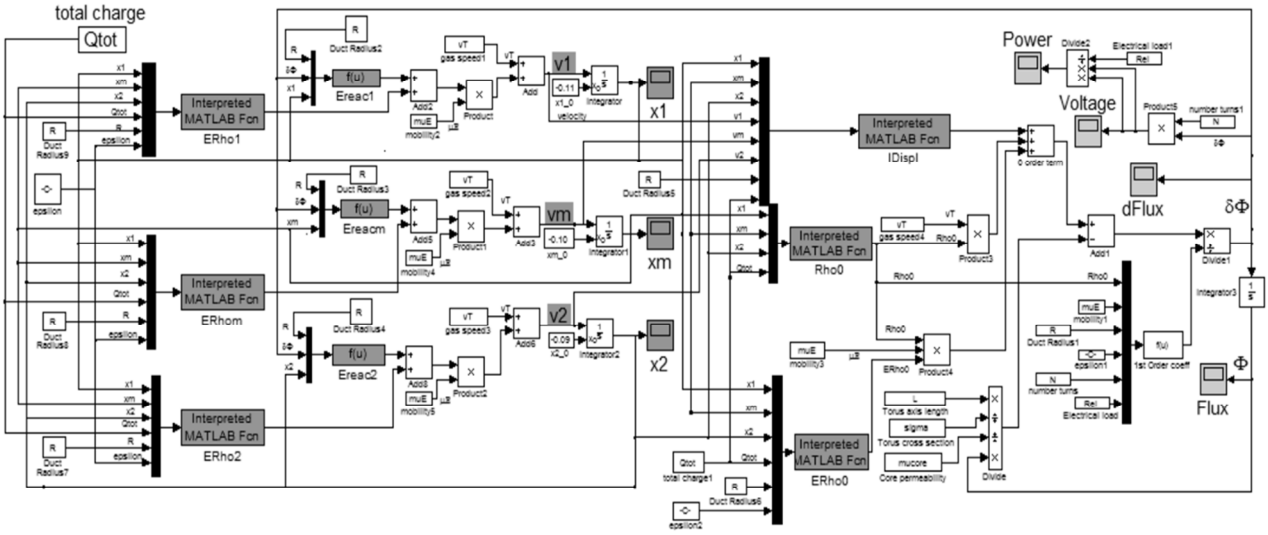

Fig. 14. Schematics of the Simulink® Model of the generator

A first stage is devoted to the calculation of the three coordinates x_1, x_m and x_2, which identify the density distribution of the charges, by integrating the corresponding velocities. To this end, two electric fields are calculated in correspondence of the three points, the field due to the charge distribution (ERho*x*, with $x = 1$, m, 2) and to the armature reaction (EReac*x*, with $x = 1$, m, 2) respectively. The sum of these two fields gives the electric field contribution to the velocity of charges, which is combined with the drag velocity of neutrals, providing the velocities of the three points (v_1, v_m, v_2). By integrating these velocities, we obtain the three coordinates, which define the charge distribution. Once this distribution has been determined, it is possible to calculate the three components of current flowing in the origin, namely the displacement current (IDispl), the dragging of the charges in the origin (Rho0), and the current determined by the electric field in the origin (ERho0). All this allows calculating the derivative of the flux (δΦ), and finally the Flux (Φ), the Voltage and the Power diagrams.

4 TA-MHD induction generator

4.1 Generalities

In this section, a further static system which exploits a quasi-static working fluid is proposed. It is a two stage Thermo-Acoustic (TA), Magneto-Hydro-Dynamic (MHD) device (Fig. 15, Fig. 16 and Fig. 17). The thermo acoustic engine converts thermal energy into mechanical energy (see Section 4.2.1) then the MHD generator converts the mechanical energy into electricity.

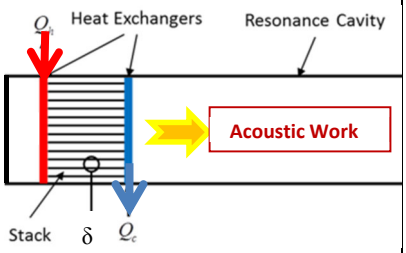

Fig. 15. TA Section

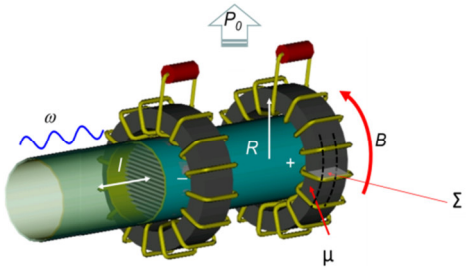

Fig. 16. MHD section [2]

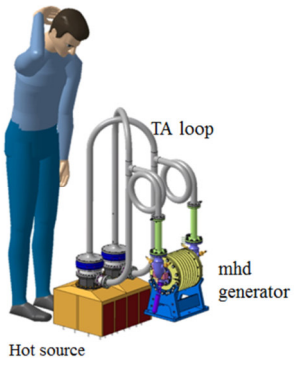

Fig. 17. Configuration adopted in SpaceTrips [68]

TA engines can convert high temperature heat into acoustic power with high efficiencies and without moving parts. In this transformation, the gradient of temperature affects the flow rate of energy, whereas the frequency is determined by the length of the duct. The TA engines have a competitive efficiency, a limited mass and promise to be high reliable [6] [8] [70].

The second stage of the energy conversion is performed by means of an MHD process.

The proposed device, inspired from the previously cited Patent [56], does not require an external magnetic field to work, since it performs the energy conversion through the induction principle. In this thesis, the proposed generation concept is validated theoretically and numerically.

4.2 Principle of functioning

4.2.1 The Thermoacoustic section

4.2.1.1 A brief historical overview on thermoacoustics

Around the half of the XIX century, the German physicist Karl Friedrich Julius Sondhauss investigated over an observation of the glassblowers who noticed that when a hot glass bulb was attached to a cool glass tubular stem, the tube sometimes emitted sound [6]. He built the so called

Sondhauss tube, a tube with the hot end closed, able to produce detectable, but very weak, gas oscillations. The Sondhauss tube is considered the earliest thermoacoustic engine. In contrast with Newton, which had hypothesized that the movement of a sound wave was isothermal, Laplace discovered the existence of gas temperature variations associated with expansions and compressions of the sound wave [54]. The first qualitative explanation of such phenomena was provided by Lord Rayleigh in the early 1870's, with the well-known Rayleigh criterion: "If heat be given to the air at the moment of greatest condensation or be taken from it at the moment of greatest rarefaction, spontaneous acoustic vibrations are encouraged" [9] [32]. Anyhow, only in the 1970's with the work of Nikolaus Rott and his collaborators, at the Institute of aerodynamics of the Federal Institute of Technology of Zurich, a theory on thermoacoustics was developed [32].

4.2.1.2 The thermoacoustic phenomenon

The thermoacoustic process can convert high-temperature heat into acoustic power (prime mover), or, vice versa, exploit the acoustic power in order to pump heat from a low temperature source to a high temperature source (heat pump) (see Fig. 18).

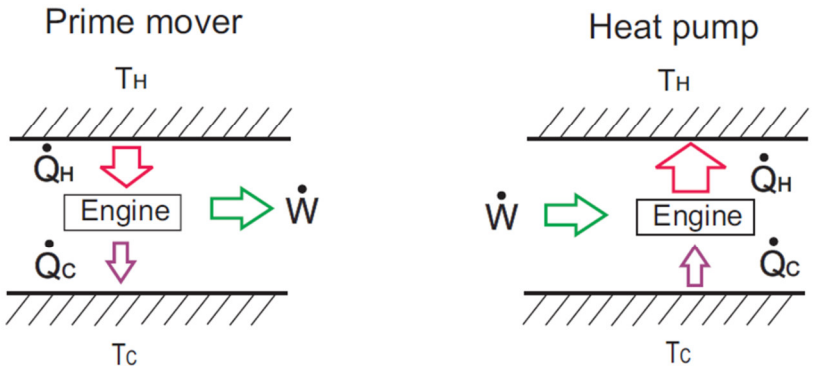

Fig. 18. The thermodynamics of the prime mover and of the heat pump [54]

The thermoacoustic conversion mechanism is intuitive; when a gas parcel enclosed in a tube comes into contact with a hot source, it experiences a thermal dilatation pushing away the adjacent particles. The same gas parcel will come, therefore, in contact with colder wall, releasing heat and then experiencing a thermal contraction. Usually, the described dilatations and contractions are localized and very weak, tending to vanish very quickly. The presence of a solid element inside the duct, the "stack", which has much higher specific heat capacity than gases, allows the cited dilatation and contractions to be amplified, giving rise to a thermoacoustic vibration if the applied gradient of temperature is steep enough.

The distance over which the diffusion of heat towards or from a solid surface can take place, is the thermal penetration depth (δ_k) and it is linked to the frequency of the sound wave and to the gas properties [6]. In order to strengthen the acoustic power generated by the engine, or to maximize the heat pumped by a refrigerator, the "stack" needs to be carefully sized with respect to the thermal penetration depth.

According with the Rayleigh criterion [69], the thermoacoustic effect is emphasized when the gas oscillation has the correct phasing with the heat exchange. For the accuracy, the compressed gas have to be in contact with the hot heat exchanger (absorbing heat), when it is at its maximum pressure, temperature and density; whereas the same gas volume have to be in contact with the cold heat exchanger (releasing heat) when it is expanded to its minimum pressure, temperature and density.

4.2.1.3 Standing-wave thermoacoustic devices [6] [9] [54] [70]

When an acoustically driven gas moves through the stack, pressure, temperature and position all oscillate with time. If the gas is enclosed within a tube, sound bounces back and forth generating interference and producing a not clearly detachable wave pattern in the medium that is usually not periodic. If the enclosed gas is stimulated with the correct frequency (resonance frequency of the tube), a standing-wave is created. In that case, particles velocity is in phase with displacement, so that the pressure reaches its maximum or minimum value (pressure antinodes) when the considered gas parcel is at one end of the duct. At the same time, pressure and velocity are out of phase, thus the gas velocity is always zero at the two ends where also the particle's displacement is null (velocity and displacement nodes).

If the distance between the stack layers is more than twice the thermal penetration depth, we are in conditions of imperfect thermal contact of the gas with the walls. In particular only the gas which is inside the thermal penetration depth is able to exchange heat with the wall. The existence of a bulk gas that is not in good thermal contact with the duct, leads to a global imperfect heat exchange which, in turn, introduces a significant time-delay between the gas motion (velocity) and its thermal expansion (pressure variation), ensuring the fulfilment of the standing-wave functioning conditions. The imperfect thermal contact occurring in the stack causes significant thermal dissipations, so standing-wave engines are inherently inefficient [70].

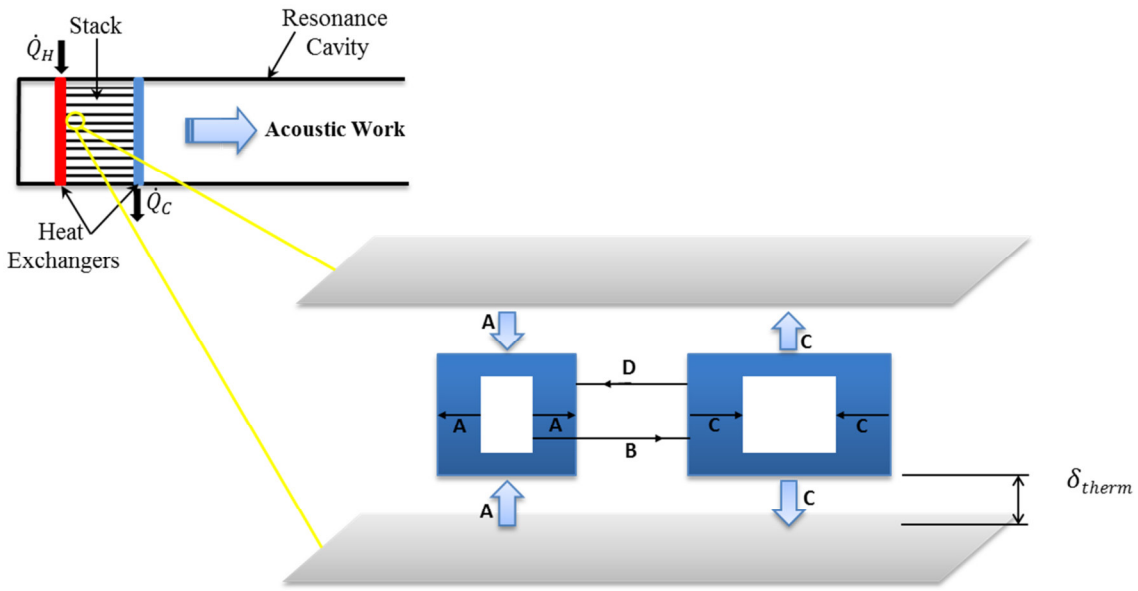

Fig. 19. Demonstrative standing-wave engine with an enlarged view of a gas parcel inside the stack

Fig. 19 shows an enlarged view of an elementary mass of gas inside the thermal layer of a stack's pore. The thermodynamic cycle, which involves that mass, is shown in Fig. 20 in comparison with an ideal Brayton-Joule cycle (gas turbines). All the fluid properties vary sinusoidally in time, but, for qualitative understanding of the process, the cycle could be described as a sequence of four discrete steps, marked as A, B, C, and D in Fig. 19 and Fig. 20.

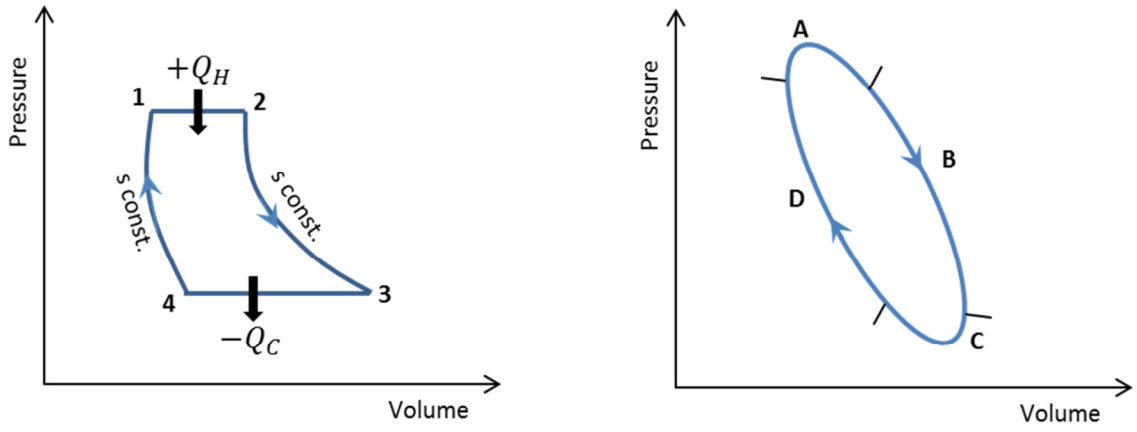

Fig. 20. Standing-wave engine ideal (Brayton-Joule) and real cycle

4.2.1.4 Traveling-wave thermoacoustic devices [6] [7] [8] [9] [10] [70]

In a traveling-wave generator velocity and pressure variations are in phase, like in a traveling wave. This result is achieved adopting regenerator's pore size less than twice the thermal penetration depth [70], thus ensuring perfect thermal contact between all the mass of gas and the solid walls. What was called "stack" for a standing-wave device is now called "regenerator" and its

channels must be smaller than those of the stack, guaranteeing a thermodynamically reversible heat transfer, so that thermal dissipation is negligible, and traveling-wave devices have an inherently high thermal efficiency [70]. At the same time, the small pores introduce a high viscous dissipation, which could be minimized by acting on the global acoustic impedance, through the addition and the correct tuning of inertances and compliances.

This concept is inspired from an idea of Peter Ceperley, which in 1979 wrote the paper titled "A pistonless Stirling engine-The traveling wave heat engine" [23] [24]. Ceperley realized that the phasing between pressure and velocity within a Stirling regenerator was the same as in a traveling acoustic wave, so that he imagined realizing a Stirling engine without moving parts. Initially the idea was abandoned due to the high viscous dissipation the sound wave suffered crossing the regenerator, which always overcame the modest power gain [6]. However, at the dawn of the current century, several research groups around the world started to reconsider Ceperley's approach, led by the rising need for improved efficiency in energy conversion. They understood that if on the one hand, the acoustic power achievable with the Ceperley's device was proportional to the product between gas pressure and gas velocity, on the other, the dissipated power depended on the square of the velocity. Therefore, like in an electrical power line, it was possible to reduce the power losses minimizing the flow velocity and contemporary increasing the pressure, in order to maintain constant the produced power, with a boosted efficiency.

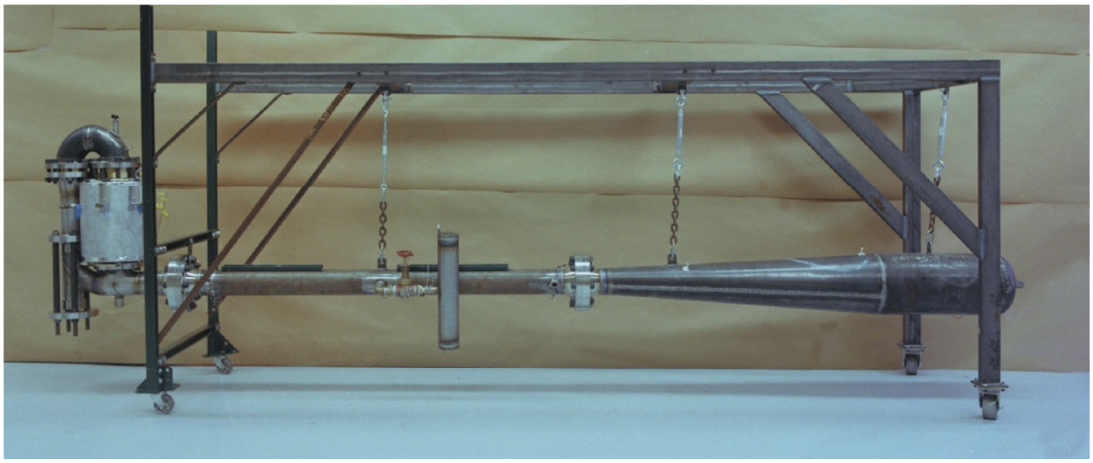

Fig. 21. Thermoacoustic Stirling engine designed at Los Alamos National Laboratory [6]

By using a hybrid standing-wave/traveling-wave engine, it was possible to achieve the needed high ratio pressure/velocity and contemporary the typical high power levels of traveling-wave devices (Fig. 21).

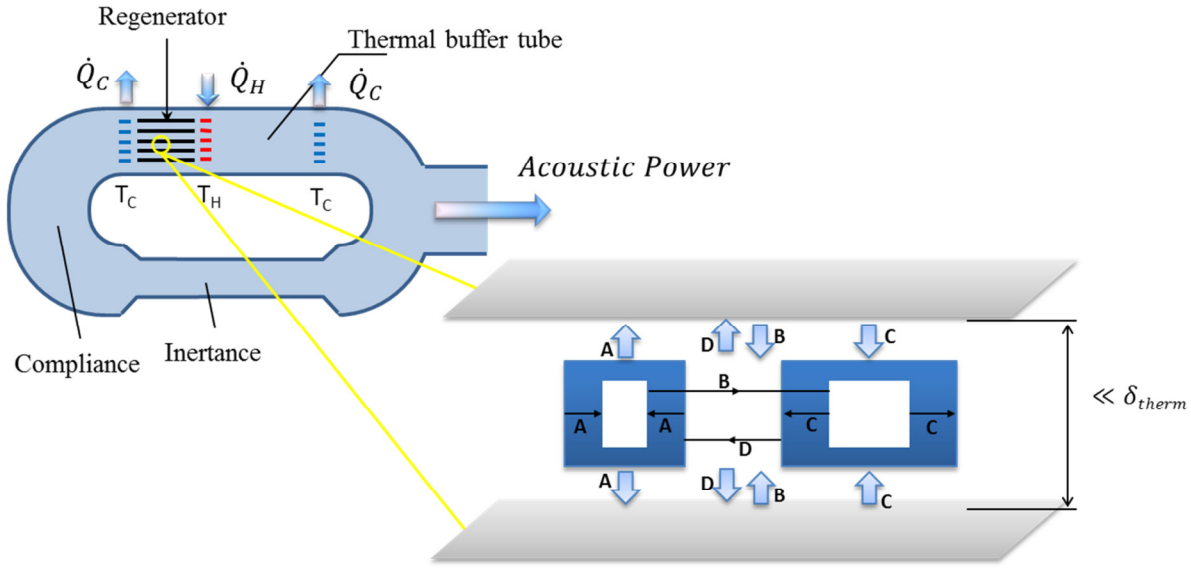

Fig. 22. Traveling wave thermoacoustic engine with an enlarged view of a mass of gas

The traveling-wave engine (Fig. 22) is able to amplify a mechanical vibration partially converting a gradient of temperature into an acoustic power gain. For a small mass of gas in a single pore of the regenerator, the four steps of the real thermodynamic cycle are illustrated in Fig. 22 and Fig. 23, in comparison with the ideal Stirling cycle.

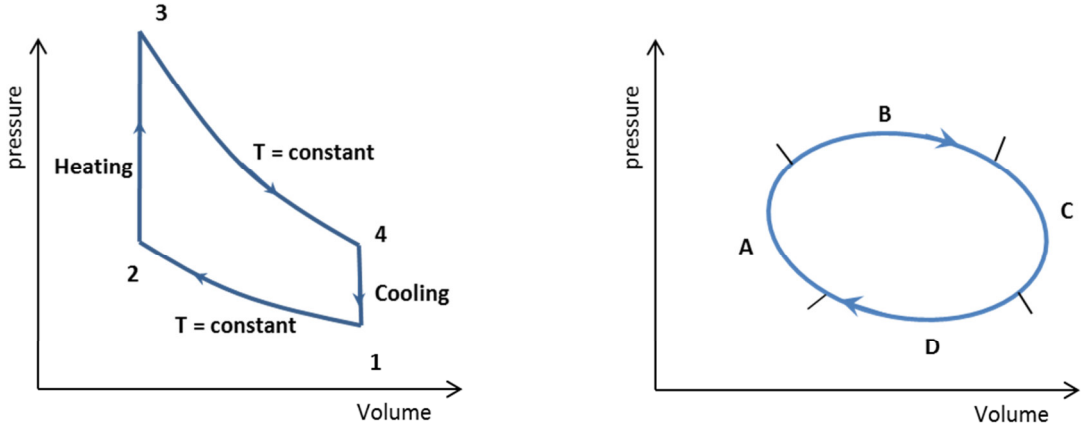

Fig. 23. Traveling wave engine: ideal (Stirling) and real thermodynamic cycle

In this study, due to the most promising power and efficiency levels achieved, a traveling wave engine has been chosen for the thermoacoustic section of the proposed TA-MHD generator, but it is considered only like a black box which is able to supply a mechanical vibration with known

characteristics taken from literature. Possible configurations for the whole generator should be the one proposed in [68] (see Fig. 17), with the MHD liquid metal stage positioned inside the thermoacoustic loop or the one with only the gaseous phase, where regenerators and capacitor plates are collapsed into a single element (see Fig. 25), both with a double thermoacoustic regenerator working in push-pull. Anyway, the global design of the generator is beyond the scope of this thesis work.

4.2.2 The MHD section

In Fig. 24, the technology of the MHD section of the TA-MHD inductive generator is depicted. The energy conversion process could be divided into four steps; in the starting phase, the gas contained in the duct is ionised under the action of a high voltage electrical discharge. The ionization of the gas can be accomplished by means of several methods, the main requirement being to limit the velocity of charge carriers, so that they can be flushed by the transversal electric field, applied by the two plates. The more suitable candidate should be the Electric Barrier Discharge method (See §4.2.2.5 [44]).

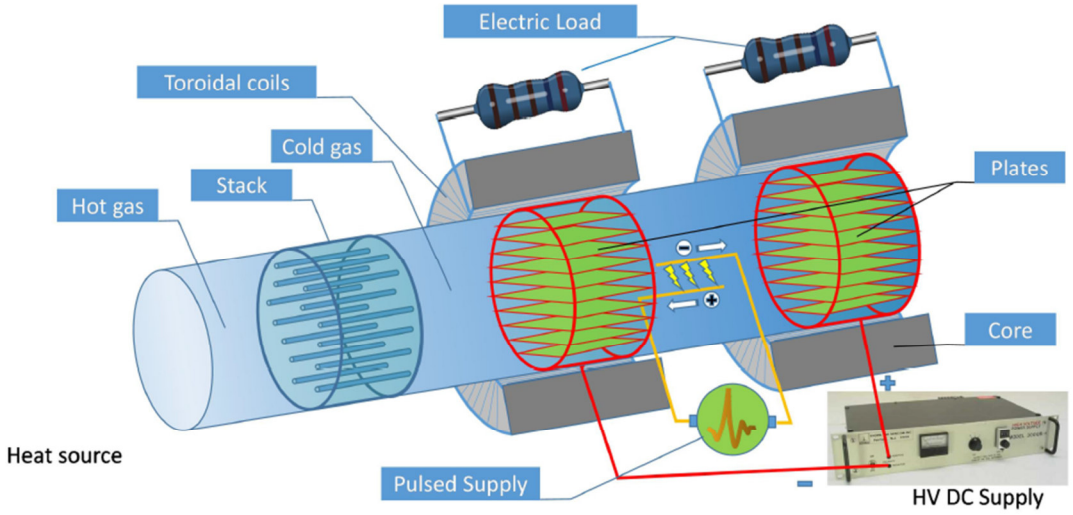

Fig. 24. Schematic view of the TA-MHD generator [22]

In the second step two clouds of charges of opposite sign are segregated by means of an external electrostatic field, applied to the gas through a properly designed capacitor. After a transient, the charges migration stops and the electric field maintains the charge carriers in a dynamic equilibrium. When the TA vibration occurs (step 3), the charges participate to the oscillating motion of the neutrals, giving rise to an alternating electrical current in the working fluid. Such current

induces in turn (step 4) an alternating electromotive force into a magnetically linked toroidal coil wrapped around the duct and connected to the electric load (Fig. 24).

In Fig. 25 a possible global configuration of the devise is depicted. A circular thermoacoustic loop has two stacks working in push-pull, the stack and the plates of the capacitor are for instance collapsed in the same component.

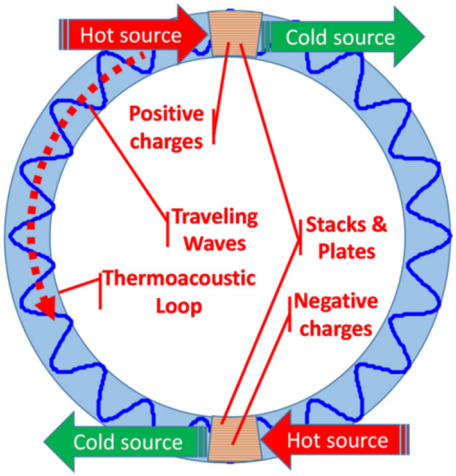

Fig. 25. Thermoacoustic loop

In the following, starting from a first, approximated theoretical study, are given the design criteria which permit to define the parameters of the generator for a given set of requirements. Secondly, the order of magnitude of the obtained parameters is used to model and simulate the system with the Finite Element Method (FEM) with the aim to confirm the theoretical results. Moreover, the charge confinement issues are analysed and some possible solutions are discussed. Finally, the issue of the optimal design of the MHD section is taken on. A multi-objective optimization algorithm, which makes use of a Tabu Search meta-heuristic [22], has been customized to this purpose.

4.2.2.1 Simplified analytical study

A first study has been done in order to perform a coarse sizing and a performance estimation of the generator for a given set of parameters. By taking into account the different sign, the two clouds of charges give rise to the same phenomenon, therefore, for the sake of simplicity, it has been assumed that the two toroidal coils are electrically independent. What follows can be independently referred to both positive and negative charge carriers.

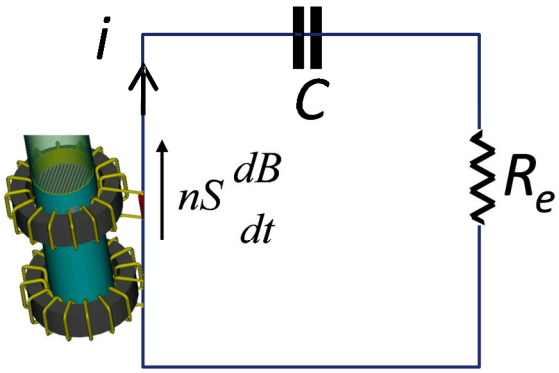

Fig. 26. Equivalent electric circuit scheme [2]

The study starts from the Ampère's circuital law and the Kirchhoff voltage equation, written for the equivalent circuit of the MHD conversion stage (Fig. 26):

$$2\pi R \cdot B(t) = \mu\big(I(t) - n \cdot i(t)\big) \qquad (4—1)$$

In this expression, $I(t)$ is the total electric current in a cross-section generated by the charge oscillation, $i(t)$ is the induced electric current in the toroidal coil, μ is the magnetic permeability of the core of the toroidal coil, where the magnetic induction $B(t)$ oscillates, and R is the mean radius of the ferromagnetic torus. For sake of simplicity, the current due to the armature reaction (see Fig. 27) and the displacement current generated by the charge distribution have been neglected. The induced current is controlled by the magnetic flux in the core of the cross-section Σ surrounded by the n-turn coil. The electrical circuit of the coil comprises also the load resistance R_{el} and a capacitance C to compensate the self-inductance of the coil. We assume that the oscillation can be approximated by a sinusoid of frequency ω, therefore, the equations can be represented in the phasorial form. The equation of the electrical circuit reads as follows:

$$j\omega nS \cdot \boldsymbol{B} = \left(R_{el} + \frac{1}{j\omega C}\right) \cdot \boldsymbol{i} \Rightarrow B^2 = \frac{1}{\omega^2 n^2 \Sigma^2}\left(R_{el}^2 + \frac{1}{\omega^2 C^2}\right) \cdot i^2 \qquad (4—2)$$

where $\boldsymbol{B} = Be^{j\phi}$ and $\boldsymbol{i} = ie^{j\psi}$. Let us call P_0 the required electrical power. Taking into account that $C = P_0/i^2$, we obtain:

$$B^2 = \frac{1}{\omega^2 n^2 \Sigma^2}\left(\frac{P_0^2}{i^2} + \frac{i^2}{\omega^2 C^2}\right) \qquad (4—3)$$

from which we can derive the condition for the minimum value of the induction field **B**:

$$\frac{dB^2}{di^2} = \frac{1}{\omega^2 n^2 \Sigma^2}\left(-\frac{P_0^2}{i^4} + \frac{1}{\omega^2 C^2}\right) = 0 \qquad (4—4)$$

Therefore, one can assess the value of the current circulating in the coil as being equal to the minimum of the magnetic induction: $i^2 = \omega C P_0$. Bearing in mind once again that $R_{el} = P_0/i^2$, that condition occurs when $R_{el} = 1/\omega C$. Eq. (4—4) allows strongly reducing the complexity of the problem formulation and evidences that the minimum value of the magnetic induction occurs when the impedance of both the capacitor and the resistor have the same modulus:

$$-\omega n \Sigma \cdot \boldsymbol{B} = \frac{1}{\omega C}(1 + j) \cdot \boldsymbol{i} \Rightarrow \boldsymbol{i} = -\frac{\omega^2 \cdot n \cdot \Sigma \cdot C}{2}(1 - j) \cdot \boldsymbol{B} \qquad (4—5)$$

By considering the expression of the power:

$$P_0 = R_{el} i^2 = i^2/(\omega C) \qquad (4—6)$$

one can obtain the value of the capacitance:

$$C = 2P_0/(\omega^3 n^2 \Sigma^2 B^2) \qquad (4—7)$$

Such value of capacitance can be substituted into the Ampere equation. The phases are referred to the ionic current I. As a consequence, this current is represented by a real value. Eq. (4—1) becomes:

$$\left[\frac{2\pi R}{\mu} - \frac{P_0}{\omega \Sigma B^2}(1 - j)\right] \cdot \boldsymbol{B} = \left[\frac{2\pi R}{\mu} \cdot B - \frac{P_0}{\omega \Sigma B}(1 - j)\right] e^{j\phi} = I e^{j0} = R_d^2 \cdot \rho_q \cdot \bar{v} \qquad (4—8)$$

where R_d is the radius of the duct, ρ_q is the average volume charge density, $\bar{v}$ is the amplitude of the sinusoidal velocity of charge carriers. This equation allows us to calculate the electric current in the gas so that the desired power and magnetic induction can be obtained. Since the right-hand side of Eq. (4—8) is real, the phase of the term within brackets in the left-hand side has to be opposite to the exponential factor out of brackets. Thus, we obtain:

$$tan\phi = \left[1 - \frac{2\pi R \cdot \omega \cdot \Sigma \cdot B^2}{\mu \cdot P_0}\right]^{-1} \qquad (4—9)$$

We can calculate the value of B which is the modulus of $\boldsymbol{B}$, which corresponds to the minimum value of the ionic current I. To do that, we have to minimize the modulus of the term within brackets in Eq. (4—8) deriving:

$$B^2 = (\mu P_0)/(2\pi R \omega \Sigma) \qquad (4—10)$$

This result comes up with an important consequence. Indeed by Eq. (4—8) and (4—9) we derive the minimum of both $\boldsymbol{B}$ and I when the magnetic induction is in quadrature with respect to the gas current. By substituting Eq. (4—10) into Eq. (4—8) we obtain:

$$\pi R_D^2 \rho_q v_0 = \sqrt{\frac{2\pi \cdot R \cdot P_0}{\mu \cdot \omega \cdot \Sigma}} \qquad (4—11)$$

Equations (4—10) and (4—11) allow us to perform the device sizing. For a given material of the torus core, Eq. (4—10) establishes a direct relationship between the required power, the size of the core and the frequency of the current. On the other hand, Eq. (4—11) provides indications on the size and on the operative conditions of the duct. As in the case of magnetic induction, the frequency and the cross-section of the core contribute limiting this parameter, whereas the permeability and the radius of the torus result in having an opposite effect. Therefore, if we have heavy constraints on both magnetic induction and electric current in gas, it would be preferable to act on the frequency and cross-section of the torus.

Finally, in order to obtain the desired current *I* in the gas, we can see that the radius of the duct has a stronger effect with respect to both the density of charge and the velocity amplitude. These three parameters are constrained for different reasons. The radius of the duct affects the size of the device, so it could be critical in contexts, where this aspect is important, such as in aerospace applications. A high charge density will require high values of capacitance and voltage in order to separate positive from negative charges. The amplitude of the charges velocity depends on the power injected into the system, then on the thermoacoustic resonator and the heat source.

The values of these parameters, reported in Table 4 represent the best compromise for a specific aerospace application. Changing the context, the best configuration of the parameters should be completely different.

By means of few substitutions we can obtain the current circulating in the coil:

$$\boldsymbol{i} = -\sqrt{\frac{2\pi \cdot R \cdot P_0}{\mu \cdot n^2 \cdot \omega \cdot \Sigma}}(1 + j) \qquad (4—12)$$

By introducing the expressions of $\boldsymbol{B}$ and $\boldsymbol{i}$ from equations (4—5) and (4—12) in the Faraday's law, one obtains the voltage drop $\boldsymbol{U}$ in the gas, which results to be in phase with the ionic current $\boldsymbol{I}$:

$$\boldsymbol{U} = \omega \Sigma \sqrt{\frac{\mu \cdot P_0}{2\pi R \omega \Sigma}} e^{j0} \qquad (4—13)$$

The voltage drop $\boldsymbol{U}$ is due to the electric field generated by the alternated magnetic flux circulating in the core of the toroidal coil. Let us call this field armature reaction. It is possible to demonstrate [17] that the field lines of such electric field have the same shape of the magnetic field due to a turn of current circulating in the place of the magnetic flux (Fig. 27).

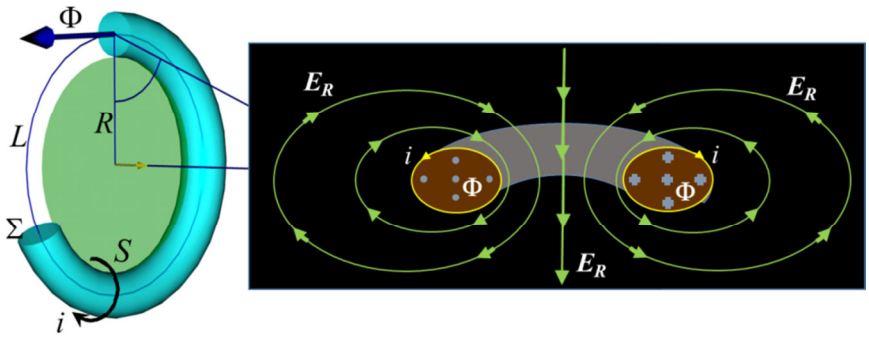

Fig. 27. Armature reaction: electric field lines

That electric field is always opposite to the velocity of the charge carriers that consequently are braked. The consequent difference in velocity between charge carriers and surrounding neutrals determines an expansion of the gas and the consequent loss of energy. Finally, we can calculate the voltage V to be applied to the plates to maintain the charges in equilibrium inside the gas:

$$C_D = \varepsilon \frac{2\pi \cdot R_d \cdot L \cdot \beta}{d_{elta}} = \frac{\pi \cdot R_d^2 \cdot L \cdot \rho_q}{V} \Rightarrow V = \frac{d_{elta} \cdot R_d}{2\varepsilon\beta} \rho_q = \frac{d_{elta} \cdot I}{2\varepsilon\beta\pi R_d \bar{v}} \qquad (4—14)$$

where C_D is the capacitance of the plate + gas system, ε is the vacuum dielectric constant, L is the length of the plate, β is the ratio between the gas-plate interface surface A_D and the surface of the internal wall of the duct corresponding to the plate, d_{elta} is the mean distance between the cloud of charge carriers and the surface of the plate.

Table 4. Design parameters and results

Real case scale		**Demonstrative facility**	
Design Parameters	**Results**	**Design Parameters**	**Results**
P_0 = 200 W	i = 1.6 A	P_0 = 10 W	i = 0.252 A
R = 12 cm	V_{coil} = 177 V	R = 6 cm	V_{coil} = 56 V
R_d = 7 cm	I = 11.28 A	R_d = 3.55 cm	I = 1.78 A
ρ_q = 15 C/m^3	U = 17.72 V	ρ_q = 15 C/m^3	U = 5.61 V
$\bar{v}$ = 30 m/s	R_{el} = 200 Ω	$\bar{v}$ = 30 m/s	R_{el} = 10 Ω
n = 10 tr	C = 0.8 μF	n = 10 tr	C = 15.9 μF
Σ = 3 10^{-3} m^2	V = 37.9 kV	Σ = 3 10^{-3} m^2	V = 15.1 kV
ω = 2π ·10^3 rad/s	$\|B\|$ = 0.94 T	ω = 2π ·10^3 rad/s	$\|B\|$ = 0.297 T
$\mu = 5\mu_0 \cdot 10^4$ H/m		$\mu = 5\mu_0 \cdot 10^4$ H/m	
d_{elta} = 0.5 mm		d_{elta} = 0.5 mm	
β = 1000		β = 1000	

It is worth specifying that in these calculations only the contribution of the convective electric current is taken into account, while the displacement currents, originating from the border effects of the electric field at the ends of the plates, are neglected.

With the aim to establish the order of magnitude, two sets of design parameters were used: the first one related to a real case scale and the second one to a demonstrative facility. The design parameters and the results coming from the analytical calculation are reported in Table 4.

4.2.2.2 FEM Acoustic analysis

A first FEM simulation has been performed with the commercial software COMSOL Multiphysics ® [5] in order to assess the bounds of the design parameters and to accomplish a rough performance estimation of the generator for the considered set of parameters [2]. To this end, it has been assumed that the MHD generator was coupled with a known thermoacoustic resonator providing acoustic power at a given frequency and velocity. Under this hypothesis, the velocity profiles corresponding to the cross-section of the duct have been studied.

Table 5. Helium properties (p = 50 bar; T = 293 K) [57]

Property	**Value**
Dynamic viscosity η [Pa·s]	$1.9912 \cdot 10^{-5}$
Equilibrium density ρ_0 [kg/m3]	7.8
Heat capacity C_p [J/(kg·K)]	5195
Thermal conductivity k [W/(m·K)]	0.156
Prandtl number P_r	0.663
Specific gas constant R_{spec} [J/(kg·K)]	2077

In order to obtain a meaningful outlet power, knowing the two-dimensional distribution of the velocities, it is mandatory to involve the largest possible number of charge carriers in the vibrating motion. In fact, both the velocity and the charge density are non-uniformly distributed along the cross-section; therefore, if most charge carriers are concentrated in zones with null velocity, the conversion process cannot take place.

The modeled device is a straight glass tube containing helium (He) at a temperature of 293 K and a pressure of 50 bar (see Table 5), within which the propagation of the imposed vibration occurs. Due to the symmetry of the device, a 2D axisymmetric geometry has been chosen for the

simulation, so that the studied domain has been a simple rectangle representing a half longitudinal section of the generator's duct (Fig. 28). The formulation used for this numerical study is referred to the thermoacoustic module of COMSOL®. Differently from what usually happens in isentropic and lossless acoustics, the used formulation takes into account the dissipative effects of viscous shear and thermal conduction. These effects cannot be neglected in acoustic wave propagation through narrow geometries such as those modeled. Actually, thermal conduction and viscosity in the proximity of the duct walls become important because they create viscous and thermal boundary layers, where losses are significant [72]. The length scale required to perform the thermoacoustic study has to be related to the thickness of the viscous boundary layer:

$$\delta_v = \sqrt{\frac{\eta}{\pi f \rho_0}} \qquad (4—15)$$

and the thickness of the thermal boundary layer:

$$\delta_{th} = \sqrt{\frac{k}{\pi f \rho_0 C_p}} \qquad (4—16)$$

where η is the dynamic viscosity, ρ_0 is the equilibrium density, f is the frequency of the acoustic wave, k is the thermal conductivity, and C_p is the heat capacity at constant pressure. Note that the thickness of both boundary layers decreases with increasing frequency f. The square of the ratio between the two length scales is the non-dimensional Prandtl number P_r, which defines the relative importance of thermal and viscous dissipations for a given fluid.

The simulation was made with the following assumptions: ideal gas; homogeneous medium, which means that the wavelength and the radius R_d of the tube must be large compared with the mean free path; non-steady flow with zero mean velocity and small amplitude sinusoidal perturbations (no circulation and no turbulence); tube long enough, so that the end effects are negligible.

The *lossy linear acoustic* model implemented with the thermoacoustic module of COMSOL® solves, in a quiescent background conditions, the fully linearized Navier-Stokes equations (4—17), the continuity equation (4—18) and the energy equation formulated using the Fourier heat law (4—19). In order to close the system, also a state equation (4—20), describing the thermodynamic behavior of the gas, must be added. The thermoacoustic interface of COMSOL® solves the system of equations for the propagation of compressible linear waves in a generally viscous and thermally conductive Newtonian fluid. The chosen physics interface is able to solve simultaneously in the

frequency domain the equations for the density ρ, the acoustic pressure p, the particle velocity vector $\boldsymbol{v}$, and the temperature T in the frequency domain assuming all fields and sources to be harmonic. Note that the indicated variables of the problem represent the acoustic deviation from the steady state solution.

$$j\omega\rho_0\boldsymbol{v} = \nabla\cdot\left[-p\boldsymbol{I} + \eta(\nabla\boldsymbol{v} + (\nabla\boldsymbol{v})^T) - \frac{2}{3}\eta(\nabla\cdot\boldsymbol{v})\boldsymbol{I}\right] \quad (4—17)$$

$$j\omega\rho + \rho_0\nabla\cdot\boldsymbol{v} = 0 \quad (4—18)$$

$$j\omega\rho_0 C_p T = -\nabla\cdot(-k\nabla T) + j\omega p \quad (4—19)$$

$$p = R_{spec}\cdot\rho\cdot T \quad (4—20)$$

where R_{spec} is the specific gas constant (see Table 5).

The value of the Prandtl number from Table 5 shows clearly that the viscous boundary layer is a fraction of the thermal one $\left(\delta_v = \sqrt{P_r}\cdot\delta_{th} = 0.814\cdot\delta_{th}\right)$, so that, in order to accurately solve the model inside the boundary layer, a very fine mesh, with a high number of parallel layers of thickness equal to a fraction of the viscous boundary layer, has been considered near no-slip boundaries (see Fig. 28).

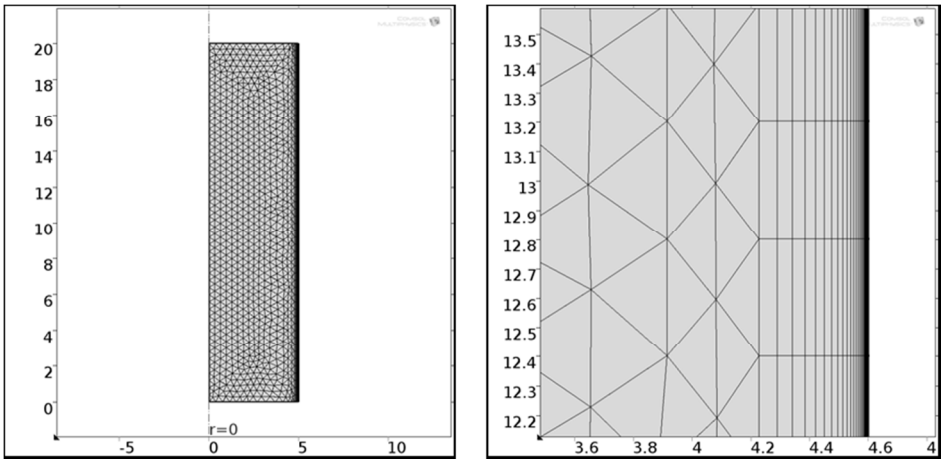

Fig. 28. Meshed model with boundary layer detail [2]

The considered boundary conditions have been:

Axial Symmetry on the axis of the duct, where there is symmetry in the pressure, so that the normal component of the acceleration could be considered null;

Sound Hard Boundary Wall on the external wall of the duct, where the normal component of the acceleration is null;

Initial Values; all the initial values of the variables have been set to zero;

Pressure; an inlet pressure has been applied to the lower (inlet) boundary of the domain and a null pressure has been considered at the upper (outlet) boundary.

Note that, in order to take into account the thermoacoustic effect, a vibration with previously assigned values of amplitude and frequency was applied to the gas. According to the literature [1] [68], a velocity $v = 30\,[m/s]$ was chosen and consequently the inlet acoustic pressure was calculated as follows:

$$p = v \cdot \rho_{He} \cdot p_{rel} \cdot c_{He} \qquad (4—21)$$

On the other hand, by assuming an ideal energy conversion process, the relative pressure at the outlet was set to zero, thus, also the outlet velocity resulted to be null.

The results of the acoustic analysis are reported hereunder. The velocity profile in the axial direction in the cross-section of a rigid cylinder is completely determined by the shear wave number [72]:

$$s = R_D \sqrt{\frac{\rho_0 \cdot \omega}{\eta}} \qquad (4—22)$$

Given the gas with a set pressure (see Table 5), the parameters, affecting the velocity distribution, are mainly the working frequency and the radius of the duct. Different velocity distributions and the corresponding shear wave number have been obtained with a parametric study by setting the radius of the duct equal to 0.1 cm, 1 cm, 1.5 cm, 2 cm, 3.55 cm (radius relative to demonstrative facility), 5 cm and 7 cm (radius relative to real device), and by varying the frequency from 10^{-2} Hz to 10^{3} Hz. In Fig. 29, the velocity distributions at the working frequency (f = 1 kHz) for the demonstrative facility (R_d = 3.55 cm) and for the real device (R_d = 7 cm) are reported. In the same figure, an enlargement shows the detail of the velocity profile in the wall proximity. In both cases, the velocity profiles have the same shape with small peaks close to the wall.

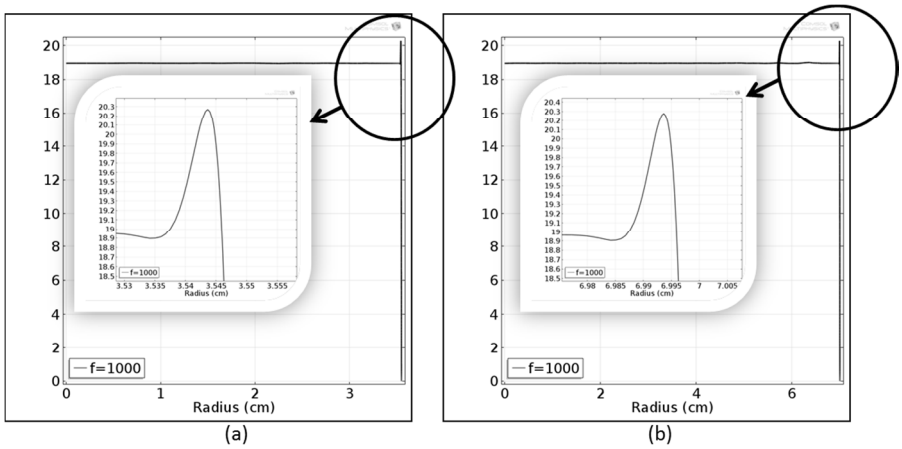

Fig. 29. Velocity distribution, axial direction; (a) Rd = 3:55 cm; (b) Rd = 7 cm (f = 1 kHz) [2]

The obtained results confirm the theoretical ones (Fig. 30) [72]. As it can be seen, for $s \leq 1$ the boundary layer lessens the entire profile, whereas with $1 \leq s \leq 2$ the velocity has a maximum in the centre of the cross section, but the profile is very narrow, therefore the average velocity is still low; for $s = 4$, the profile is still parabolic and the average velocity increases. Generally, at low values of the shear wave number $(0.4 \leq s \leq 4)$ the axial velocity shows a parabolic profile. At higher values $(s > 4)$, the amplitudes of the velocity in the center of the tube become smaller and the profile becomes more and more uniform. With very high values of the shear wave number, the velocity profile is almost completely flat, with small peaks close to the tube wall and it tends to involve an even larger part of the cross section.

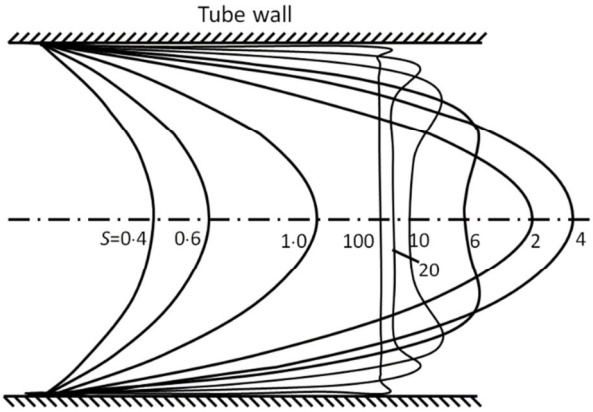

Fig. 30. Velocity distribution in axial direction for a varying shear wave number [72]

The achievable power is linked to the ionic current density and thus to the amount of charges confined. As can be noticed from the analytical study (see equation (4—14)), in order to optimize the performance of the device, the interface-surface of the plate + gas system and its electric capacity have to be maximized, ensuring the growth of the amount of confined charges and, at the

same time, the voltage to be applied, needs to be minimized for insulation issues. Summarizing, the dimensionless parameter β has to be maximized. This parameter is the ratio between the surface of the actual capacitor plate and the corresponding surface of the wall. In order to have high values of β, we can use a plate constituted by a thick pack of layers having a very rough surface. If due to the growing β, a significant part of the cross-section is occupied by the grid, viscous effects will beget high losses, causing a considerable reduction of the vibration velocity of the charge carriers thickened into this area. Then, the charges have to maintain a suitable distance from the wall and the distance between two contiguous sheets of the capacitor has to be at least larger than the double of the viscous boundary layer.

A number of numerical analysis has been performed in order to retrieve useful indications for the design of the capacitor [13], so that the best configuration can be chosen taking inspiration from the studies in the literature.

As previously reported, the profile of the velocity depends on the shear wave number s (see equation (4—22)) which is, apart from a factor $\sqrt{2}$, coincident with the ratio between the radius of the duct and the thickness of the viscous boundary layer (4—15); for given gas, pressure and frequency, eq. (4—22) can be used to determine the optimal distance between two contiguous sheets of the capacitor.

As explained about the TA generators (see section 4.2.1), in order to ensure good thermal contact between gas and solid walls, so that pressure and velocity will be in phase and hence the powerful and efficient traveling-wave functioning is guaranteed, the optimal distance between two plates of the stack is equal or less than twice the thermal penetration depth.

Taking into account all these aspects, the same element could be capacitor and stack simultaneously. Therefore the best distance between sheets, which represent the best compromise between the intensity of electric current in the gas, the global dimensions of the device and the thermoacoustic requirements, can be determined ((see the following section 4.2.2.5 for further comments about this issue).

4.2.2.3 FEM Electrostatic analysis

Another FEM simulation has been performed with the aim to study the electrostatic behavior of the charges inside the generator [2]. The modeled 2D axisymmetric geometry (see Fig. 31) consists

of a glass tube closed at the ends containing ionized helium gas with the properties summarized in Table 5.

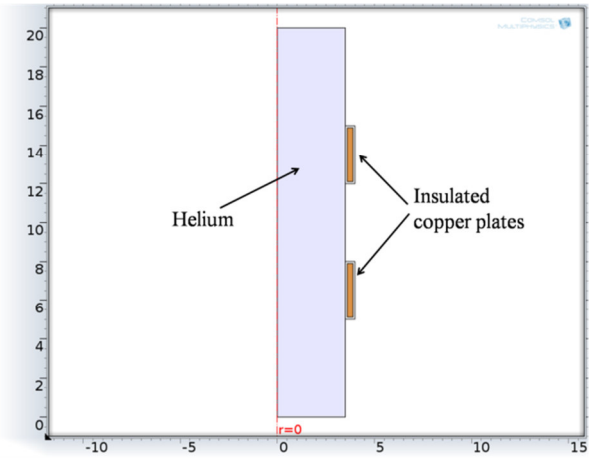

Fig. 31. 2D axisymmetric model geometry [2]

Two insulated copper sleeve plates were positioned at an equal distance from the duct extremities and it was assumed that they were connected to a HVDC power supply. In that case, the ratio β between the surface of the plate and the correspondent surface of the wall was considered equal to unity. The Electrostatic Module of COMSOL® is used to compute the electric field $\boldsymbol{E}$, the electric displacement field $\boldsymbol{D}$ and the electric potential distribution; it solves the Gauss' law for the electric displacement field (eq. (4—23) and (4—24)), where the scalar electric potential V represents the dependent variable of the problem.

$$\nabla \cdot \boldsymbol{D} = \sigma_q \qquad (4—23)$$

$$\boldsymbol{D} = \varepsilon_0 \varepsilon_r \boldsymbol{E} = \varepsilon \boldsymbol{E} \qquad (4—24)$$

$$\boldsymbol{E} = -\nabla V \qquad (4—25)$$

The considered boundary conditions have been:

Charge Conservation on the whole domain; which adds the equations for charge conservation according to the Gauss' law for the electric displacement field;

Axial Symmetry the duct axis, where a no-flux condition is imposed to the electric field;

Zero Charge on the external walls of the duct, where the normal component of the electric displacement field $\boldsymbol{D}$ is null;

Initial Values; all the initial values of the variables have been set to zero;

Space charge density in correspondence of the two plates; which adds two volume charge distributions of opposite sign.

Dielectric Shielding on the external insulated sides of the capacitor plates, which introduces a thin material layer that shields out the electric field.

Electric potential on the copper plates' edges; where an imposed potential is considered.

A volume charge density ρ_q obtained as a result of a previous charge separation (according with Table 4) was inserted in correspondence of the capacitor plates. With a parametric analysis, by varying the external source HVDC in a range from 1 MV to 2 MV (Fig. 32a), an optimal value of voltage equal to 1.63 MV was found (Fig. 32b). Applying this value to the copper plates, the electric potential profile was null and flat in the central zone between the two plates (Fig. 32b), where the electric field was thus equal to zero (Fig. 33).

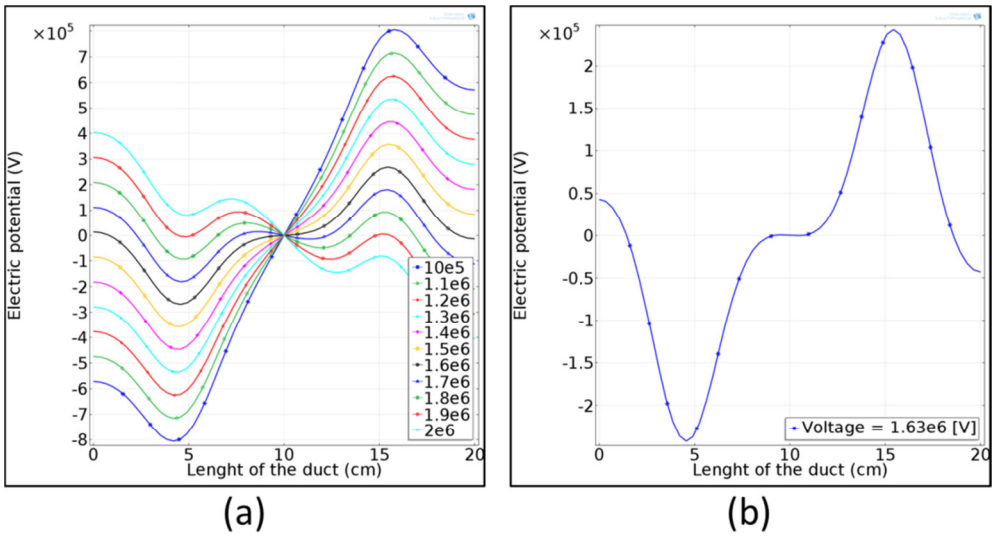

Fig. 32. Electric potential along the duct as a function of applied voltage: (a) Parametric; (b) Optimal [2]

As shown in Fig. 33.a, the electric field is mainly confined in the inner volume within each sleeve.

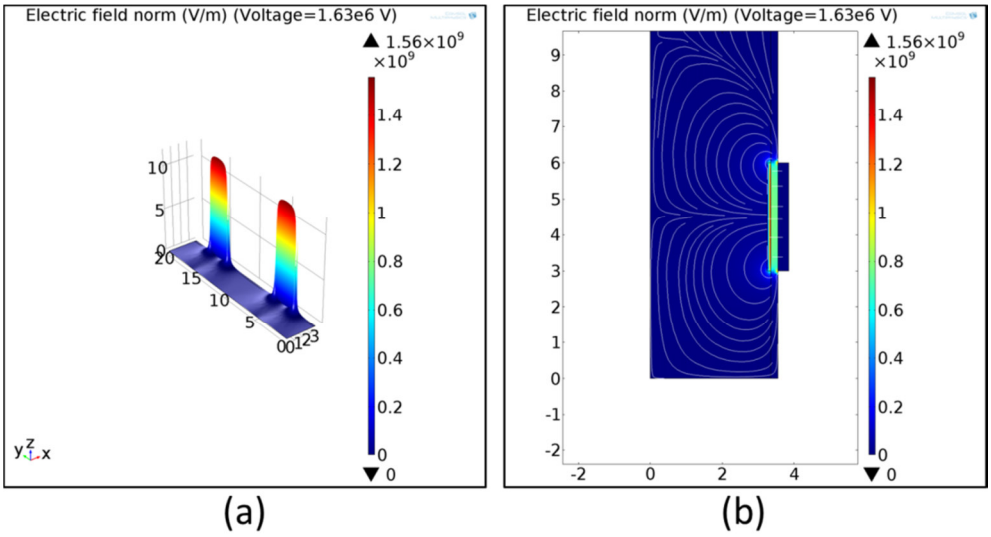

Fig. 33. Electric field along the duct (V = 1.63 MV): (a) mapping; (b) force lines [2]

This allows achieving an equilibrium condition for the charge distributions that the electric field cannot alter. The value of the needed voltage can be reduced by increasing the plate-gas interface-surface, e.g. by using a pack of layers, as described above ($\beta \gg 1$). For example, by assuming $\beta = 1000$, like in Table 4, the voltage we need is reduced of three orders of magnitude until 1.63 kV. This value still differs by one order of magnitude from the theoretical one calculated for the demonstrative facility (see Table 4) because two different charge distributions were considered. Finally, the force lines of the electric field along the duct are shown in Fig. 33b.

4.2.2.4 FEM Multi-physics analysis

A multi-physics analysis, where acoustics is coupled with electrostatics and particle tracing, was implemented with the aim to perform a preliminary assessment of the behavior of a system of unbalanced charge carriers when they are subject to an acoustic vibration and to an external electric field. A special attention was paid to the phenomena occurring in the volume inside the plates of the capacitor where the charges are confined, therefore the thermo-acoustic effect is treated here once again as an external pressure source.

The simulation was done with the same assumptions of the previous ones (ideal gas; homogeneous medium; no steady flow with small amplitude sinusoidal perturbations; tube long enough, so that the end effects are negligible). The modeled geometry was, as usual, a straight glass tube, full of helium, with two copper capacitor plates positioned at the same distance from the ends and connected to a high voltage DC supply (see Fig. 31). Moreover an initial uniform distribution

of negative charged particles was released in the whole volume of the duct and their time evolution was observed. The behavior of the positive charges will be certainly dual.

The lossless Acoustic module, used to compute the pressure variation for the propagation of acoustic waves in fluids in quiescent background conditions, solves the Helmholtz equation (4—26) in the frequency domain. That equation was obtained by combining a linearized, small parameter expansion of the Navier-Stokes equation (momentum equation) and of the continuity equation (mass conservation) for the time-harmonic pressure wave considered as input.

$$\nabla \cdot \frac{1}{\rho}(\nabla p) - \frac{k_{eq}^2 p}{\rho} = 0 \qquad (4—26)$$

where $k_{eq} = \omega/c$ is the wave number, ω is the angular frequency of the imposed acoustic oscillation and c is the speed of sound in the considered medium. The equation, obtained for a reversible and adiabatic process, is solved for the acoustic pressure p; the particle velocity vector $\boldsymbol{v}$ is subsequently derived.

It can be noted that in equation (4—26) the contribution of electromagnetic forces has been neglected since for hypothesis in the studied problem there are no energy exchanges with the external ambient. In that situation, the low concentration of charge carriers allows to neglect their contribution to the neutrals motion from the macroscopic point of view. Therefore, the fluid dynamic problem could be decoupled from the electromagnetic one and solved separately; the obtained solution will be used as inlet for the electrostatic Model and for the particle tracing one.

Subsequently, the Electrostatic Module solves the Gauss' law for the electric field with respect to the electric potential (see eq. (4—23), (4—24), (4—25)).

Finally, the Particle Tracing Module, governed by the formulations from classical mechanics (Newtonian, Lagrangian, or Hamiltonian), allows to compute and to visualize the trajectory of the particles in the fluid, under the action of the electric field and of the acoustic force. The dependent variables are the components of the particle position vector $\boldsymbol{p_p}$.

$$\frac{d(m_p \cdot \boldsymbol{v})}{dt} = \boldsymbol{F} \qquad (4—27)$$

where m_p is the particle mass, $\boldsymbol{v} = d\boldsymbol{q}/dt$ is the velocity vector and **F** is the total force acting on the particle. That force is given by the sum of the drag force exerted from the fluid flow, with the gravity force (neglected in the described study) and with other external forces like the electric force and the acoustic force hereby considered.

The considered boundary conditions for the acoustic and the electrostatic study have been the same described previously (see sections 4.2.2.2 and 4.2.2.3); with respect to the particle tracing, it has been imposed:

Axial Symmetry on the axis of the duct, where it is imposed the so called ***Diffuse scattering*** that the incident particles are bounce off according to the Knudsen's cosine law, which states that the probability a particle bouncing off the selected boundary in a given direction within a solid angle $d\omega$, is given by $cos(\theta)d\omega$ where θ is the angle between the direction of the particle and the normal to the wall.

Wall on the external walls of the duct (including inlet and outlet sections), where the condition ***Bounce*** specularly reflects the incident particles from the wall, so that the particle momentum is conserved;

Particle properties, which specifies the particle properties as charge number, density and diameter;

Release, which sets on the whole simulated volume, the release times, initial position, number of particles per release and initial velocity of the released particles;

Acoustophoretic Force, which adds an acoustic force on the charged particles, due to acoustic pressure distribution calculated from the acoustic study.

Electric Force, which adds an electric force to the particles linked to the electric potential or the electric field. The field comes from the computation done by the electrostatic module.

After a transient of 1 [s], the charge distribution reached a regime of dynamic equilibrium. In Fig. 34 three different charge distributions are reported in correspondence of three different time instants: the start, the middle and the end of the transient.

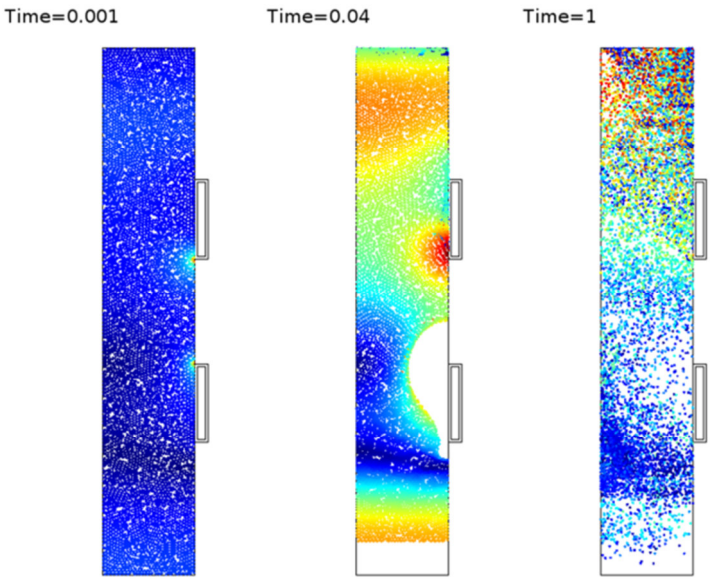

Fig. 34. Particles position at three different instants (red: high velocity, blue: low velocity) [21]

The negative charges, as expected, tend to thicken near the positive plate (the upper one) of the capacitor under the action of the electric force. Furthermore, the particles move forward and backward along the duct due to the acoustic wave, giving rise to an alternating current in the fluid. As it can be noted, under the combined effect of acoustic perturbation, external field and mutual repulsive forces, the charge carriers tend to distribute in the whole cross section of the duct, while along the axis they have the maximum concentration within the positive capacitor plate.

This preliminary result represents a first fundamental step for the assessment of the process suitability. Indeed, it shows that the charge carriers tend to gather inside the volume of the plates but do not stick on their walls, so that they can participate to the vibrating motion of the neutrals and then give rise to an alternate electric current, which the energy conversion process is based on.

4.2.2.5 Charge generation and confinement issues

The energy conversion process requires a high charges concentration in the working fluid, which is a gas at low temperature; therefore, those charges have to be generated in the gas by means of an external intervention. The charge carriers have to be pushed towards the two plates of the capacitor (Fig. 24); therefore, ionization processes that transmit an excessive velocity to the charge carriers are not suitable for this application. The most promising technology for charge generation is the Dielectric Barrier Discharge [44]. In this process, the charge carriers bump the dielectric barrier, which makes easier to address them towards the capacitor plates (Fig. 35), in a direction orthogonal to that one of the ionizing field.

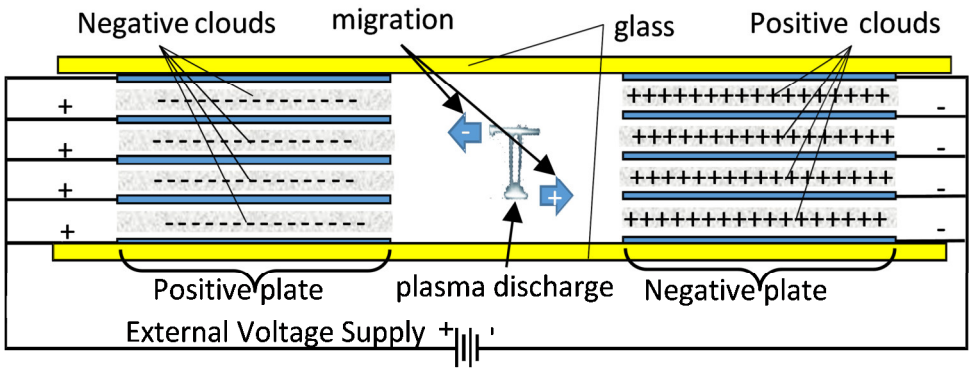

Fig. 35. Representation of the charge confinement system [3]

Another crucial issue concerns the charge confinement technique. The system formed by the two plates and the ionized gas performs as a double-layer capacitor [11] [13]. The capacitor charging process might require a long time, depending on the rate of charge generation and on the applied external electric field. On the other hand, the charging is performed only once, therefore its duration is not a critical design aspect.

The charge density strongly affects the output power of the generator, because a high density of charges causes an intense ionic current. The amount of confined charge depends on both the applied voltage and the plates' capacitance. The energy consumption of the voltage supply is virtually null, but the applied voltage must be limited for insulation issues, so that the plates of the capacitor should have a high ratio surface/volume, as depicted in Fig. 24. Other shapes can be assumed in order to increase the surface/volume ratio, provided that the particles are free to oscillate along the axis of the duct.

As the same feature is required for the thermo-acoustic stack [76], it is worth to evaluate the possibility to have a unique element that plays both the roles of stack and capacitor plate, in this way limiting the hydraulic losses. Actually, the two functions have a number of requirements; therefore the choice of a unique element is not at all straightforward. In order to guarantee a suitable temperature gradient, the material of the stack have to be a bad thermal conductor, whereas the plate has to be a good electrical conductor, which propriety in general is associated to the thermal conductivity. Furthermore, the capacitor plate has an isolating coat, which could be not compatible with the temperature of the hot end of the stack. Finally, the functioning of the stack and the plate is associated to the thermal and hydraulic boundary layer respectively, whose depth could be right different, depending on the operating conditions. Therefore, in spite of the fact that collapsing the

two functions could considerably improve the performance of the generator, a number of design issues have to be nailed down.

In order to obtain a suitable value of the electric current, it is fundamental that most part of charges remain beyond the viscous boundary layer, so that they can be involved in the vibration. The generation of the electric current in the gas is the combination of different well-established electro kinetic phenomena, such as electrophoresis, sedimentation potential and colloid vibration current [30]. We know that, when a potential is applied to a surface in contact with an electrolyte, the charge carriers in the fluid do not stick to the wall, but a charge-free layer (Stern layer [30]) tends to separate the surface from the layer of adsorbed charges.

The peculiarity of the setup of the present work makes necessary the adaptation of the models commonly used for studying the involved phenomena. For example, the attractive force towards the walls is mitigated for two different reasons. First of all, the charge carriers are confined between two equipotential plates. Furthermore, in the gas there is a limited amount of charge carriers, equal to the quantity segregated during the charging phase. This implies that beyond a certain voltage applied to the capacitor plates, the charges in the gas are not able to shield out completely the external electric field. Acting properly on some design parameters (as the applied potential, the number of available charges, the frequency of the vibration and the properties of the gas), it is possible to influence the thickness of the Stern layer and in general the charges' mobility, so that the charge distribution could be modified, maximizing, at the end, the number of carriers involved in the vibrational motion.

4.2.2.6 MO-TS optimal design of the MHD section of the TA-MHD generator

A multi-objective optimization problem (MOP) or vector optimization problem is characterized by a vector of mutually conflicting objective functions [29].

The MOP problem can also be seen as a constrained optimization problem where one or more of the quantities are assumed as the function to be optimized, whereas the other quantities are defined as constraints of the problem. The two definitions are similar and all the quantities involved can be treated as objective functions of the MOP, neglecting their division into goals and constraints.

During the last decades, stochastic techniques have been widely investigated in order to face optimization problems with multiple conflicting objectives. A large number of multiobjective stochastic optimizers, based on local or global search methods, have been developed for the optimal

design of electromagnetic devices [20] [27] [28] [41]. These algorithms are commonly referred to as evolutionary algorithms, including Genetic Algorithms, Tabu Search (TS) methods, Ant Colony algorithms, and Particle Swarm Optimization. Among them, TS methods are meta-heuristic iterative procedures that guide a local search avoiding trapping in local minima. These methods, starting from a potential optimum, tend to investigate in depth its immediate neighbors aiming to find an enhanced solution. As a drawback, the local search risks to be trapped in a suboptimal region, like a local minimum. However, the TS technique is able to improve the performances of the cited optimum search method by allowing worsening moves and avoiding the return to the already examined solutions. Some scalarization techniques have been proposed in literature with the aim to adapt the inherent scalar schema of the TS to the vector optimization problems [15] [78]. Conversely, in [20] an innovative fully vector multiobjective TS algorithm has been proposed and its performance has been successfully compared with other existing TS algorithms on some analytical and electromagnetic MOPs, whose Pareto front is available from the literature [5] [14] [25] [71]. A MOP can be formalized as follows:

$$\min_{\bar{x}\in\Omega} \boldsymbol{F}(\bar{x}); \qquad \Omega = \{\bar{x}\epsilon R^n:\ G(\bar{x}) \leq 0;\ H(\bar{x}) = 0\} \qquad (4—28)$$

where $\bar{x}$ is the vector of the n real-value input variables (design variables), Ω denotes a decision variable space and $\boldsymbol{F}$ is the vector of objective functions (F_1, F_2, F_3,……F_k). Here $G(\bar{x})$; $H(\bar{x})$ represent the problem constraints. A MOP aims to find the Pareto-optimal solutions, by seeking non-dominated solutions. In a MOP, a solution $\bar{x}_d$ is dominated by another solution $\bar{x}_{nd}$ if $\bar{x}_{nd}$ is better than $\bar{x}_d$ on all objectives, and it will be denoted, here, by $\bar{x}_d \prec \bar{x}_{nd}$. A solution $\bar{x}_p$ is a Pareto optimal solution if no objective function can be improved without worsening at least one other objective function.

In this work, the fully vector Multi-objective Tabu Search (MO-TS) algorithm proposed in [20] has been customized in order to investigate the optimal design of the MHD section of the studied TA-MHD electric generator.

The obtained algorithm is able to build a list of non-dominated solutions deeply exploring regions of the parameters space that look promising, and moving away from regions that do not look promising. A Pareto-optimal list **P** is introduced in the proposed method. The values of the archive are dynamically updated and used in the optimization process; at each iteration, some

solutions in the Pareto-optimal list **P** could become dominated by the new solution, and then they must be removed. The length of this list is finite.

In order to overcome the limit of the TS schema, which is inherently scalar, the vector optimization problem is formalized by assigning to each visited solution x_i two functions to be maximized:

$$f_1(\bar{x}_i) = \frac{1+N(\bar{x}_d \prec \bar{x}_i)}{1+N(\bar{x}_{nd} \succ \bar{x}_i)} \qquad (4—29)$$

$$f_2(\bar{x}_i) = \left(exp\left(-0.5\left(\frac{d-\lambda}{\gamma}\right)^2\right) - exp\left(-0.5\left(\frac{d}{\gamma}\right)^2\right)\right) \qquad (4—30)$$

The first one (f_1) allows storing a set of solutions that are not dominated by those already present in the list. Referring to the list **P** of the Pareto optimal solutions presently found, $N(\underline{x}_d \prec \underline{x}_i)$ is the number of such solutions that are dominated by the current solution $\underline{x}_i$, $N(\underline{x}_{nd} \succ \underline{x}_i)$ is the number of solutions dominating $\underline{x}_i$. The aim of the algorithm is to find solutions not dominated, therefore solutions with $N(\underline{x}_{nd} \succ \underline{x}_i) = 0$.

The second function (f_2) has two terms, the first one that favours the new points at a certain distance from the nearest point of **P**, and the second one that penalizes the points that are very close to a point of **P**. Some parameters in the function have to be set: d is the smallest distance between the visited solution x_i and the points of the list **P**, whereas λ and γ determine the sampling step of the Pareto front. In fact, equation (4—30) is the combination of two Gaussian functions with the same variance γ and different mean value (λ in the first one and 0 in the latter). Then, f_2 penalizes the solutions close to those already found, whereas it privileges those with a distance equal to λ. The function f_2 is null for the solutions far from the already found ones. Therefore, maximizing f_2 a uniform sampling of the Pareto Front is fostered.

Accordingly to the absence of solid moving parts and to the exploitation of a quasi-static working fluid, peculiarities of the considered energy conversion system are the high power to mass ratio, the high energy conversion efficiencies and the low maintenance requirements. Depending on the specific application, which the generator is oriented to, different regions of the Pareto front could be of interest for the designer. For example, for space applications, the limitation of mass and the space-saving are strategic, so as for automotive field, but in this case higher level of power have to be considered; on the other hand, in nuclear plant and in nuclear fusion, the main target is to

maximize the flow of power, while larger size and high values of exciting voltage are allowed; finally, in renewable energy harvesting, a low level of power can be accepted, provided that the excitation voltage and the size are limited.

In [2] the coarse sizing of the MHD section is performed analytically by assuming the physical quantities derived from the TA section as inputs. As a result, the relations among the variables of the system are assessed, allowing defining the set of design parameters and the objectives. In the present work, the feasible ranges of the design parameters and the target values are assumed on the basis of the power requirements for future deep Space and Mars science missions stated by NASA [60], which envisage Radioisotope Thermoelectric Generator systems with a specific power of 9 10 [W/kg] and a power of 100 [W] or greater. In [21], the applicability to the present context of the data concerning the assumed velocity and pressure profiles has been validated by means of a FEM multiphysics analysis.

In the present study, the MO-TS algorithm has been used with the goal to optimize only the MHD section of the generator, i.e., the size of the duct, the characteristics of the capacitor plate, which work also as stack and the dimensions of the magnetic core.

In Fig. 36 a schematic view of the MHD section is shown. Particularly, the geometrical design parameters to be optimized are the thickness of the torus Rx, the radius of the duct Rd, the distance δ between the sheets of the capacitor's plates. The frequency has been swept around classic values for thermoacoustic generators [1] [10] [54] [68], pushing toward higher values that allow size and mass reduction of the duct and thus of the whole device. The sweep has been stopped at values around the kHz beyond which the viscous losses are no longer negligible and the device size becomes excessively small. Finally δ was swept from four to one hundred times the viscous boundary layer in order to ensure that the velocity profile is totally developed. The length l of the capacitor, which has also the function of stack in order to reduce hydraulic losses inside the generator, it is set on the basis of the thermal gradient required to trigger the thermoacoustic vibration [32] [70], taking into account that the temperatures of hot and cold source are of 827°C and 127°C respectively [68]. Concerning the length L of the torus, it cannot be used as design parameter because the optimization process tends to maximize it without any bound. A value has been set, such that the magnetic saturation of the core should be avoided, independently on the other design parameters.

To a first approximation, the induction $\boldsymbol{B}$ is assumed to be uniformly distributed in the cross section of the core. In the real case, a number of influencing factors have to be taken into account. For example, the thickness of the core and the ratio between the widths L and l of core and plate should cause a non-uniformity of $\boldsymbol{B}$; on the other hand, the local saturation of the core should improve the homogeneity of the distribution. All these aspects are beyond the scope of this work, and they have been neglected.

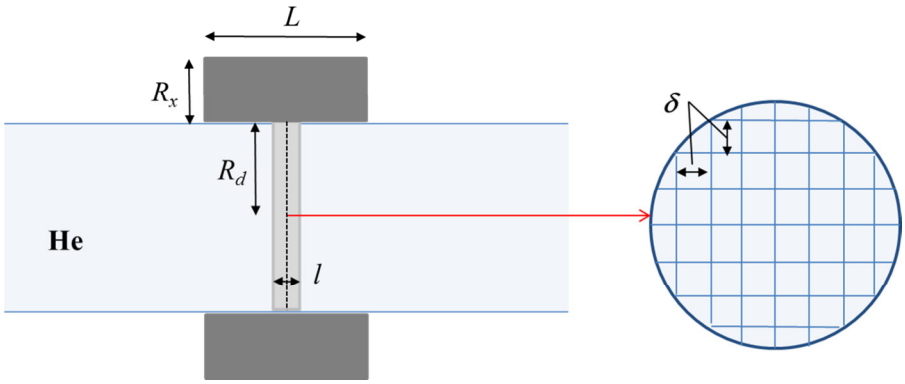

Fig. 36. Schematic view of the MHD section, with a magnified capacitor plate section [22]

The charge density is a critical parameter because, for a given frequency and amplitude of the thermo acoustic vibration, the higher the charge density the higher will be the ionic current in the gas and then the outlet power. In order to confine a sufficiently large quantity of charge carriers in the gas, the plates of the capacitor have to be characterized by a large surface/volume ratio. This requirement can be fulfilled by adopting a sieve, rather than a sleeve, as shape of the plates, obtained by means of a set of parallel sheets, electrically connected among them by a peripheral ring (see the right side of Fig. 36). At the same time, it is crucial avoiding the volume where the fluid viscosity tends to dissipate the velocity, thus the distance δ between two consecutive sheets is assumed as a multiple y of the thickness of the viscous boundary layer (4—15) in order to minimize the viscous dissipation.

The confinement of the charges inside the plate of the capacitor is carried out as it occurs in a porous electrode of a double layer ultracapacitor [11] [13]. The applied electric field attracts the charges inside the cavities, where an equipotential wall surrounds them. Inside the cavity, the charge tends to distribute on the wall, in order to cancel the electric field in the cavity itself. Once the gas is set in vibration, the charge is distributed between a stagnant layer and a hydrodynamically mobile layer [30]. The stagnant layer does not take part to motion, and then the charge inside this layer does not participate to the transmission of power. The quantity of charge that stay within the

stagnant layer depends on several parameters, such as the applied potential, the number of available charges, the frequency of the vibration and the properties of the gas. The determination of such design parameters is beyond the scope of this work, so we will assume, to a first approximation, the entire charge participates to the motion of the neutrals.

Table 6 reports the design parameters of the MOP together with their feasible regions.

Table 6. Design parameters of the MOP with their feasible regions

Design parameters	Description	Range	Units
R_d	Duct radius	[7 ÷ 30]	[cm]
R_x	Torus thickness	[1 ÷ 30]	[cm]
y	Ratio between the capacitor plates thickness δ and the viscous boundary layer δ_v	[4 ÷ 100]	[a.u.]
f	Frequency of the inlet acoustic vibration	[10 ÷ 1000]	[Hz]

In order to limit the computational costs and to fulfill the construction constraints, some of the design parameters have been fixed. Table 7 reports the values of the other parameters involved in the design of the device, which have been set from literature as the best choice for a specific aerospace application [2].

Table 7. Imposed design parameters set from literature

Fixed parameters	Description	Value	Units
μ	Torus relative permeability (mu-metal)	$5 \cdot 10^4$	[a. u.]
ρ	Torus mass density (mu-metal)	8747	[kg/m^3]
ρ_0	Helium equilibrium density	7.8	[kg/m^3]
η	Helium dynamic viscosity	$1.9912 \cdot 10^{-5}$	[Pa·s]
$\bar{v}$	Charges velocity amplitude [2]	30	[m/s]
ρ_q	Average charge density inside the capacitor	5	[C/m^3]
l	Capacitor length	1	[cm]
L	Torus length	15	[cm]

Three conflicting objective functions have been selected:

- ✓ the output power P delivered to the loads;

- ✓ the voltage V to be applied to the plates of the capacitor;
- ✓ the mass M of the device.

In [2], by minimizing both the magnetic induction B and the ionic current I in the gas, the following relation between the theoretical output power P_0 and design parameters was derived:

$$P_0 = \frac{\pi \cdot \mu \cdot \mu_0 \cdot \omega \cdot \Sigma \cdot R_d^4 \cdot \rho_q^2 \cdot \bar{v}^2}{2(R_d + R_x)} \qquad (4—31)$$

where μ is the magnetic permeability of the torus, ω is the angular frequency of the inlet acoustic wave, Σ is the cross-section of the torus of length L and thickness R_x, ρ_q is the average volume charge density confined inside the capacitor and $\bar{v}$ is the maximum amplitude of the sinusoidal velocity of the charge carriers.

However, the actual power to the load is lower than P_0, due to the viscous power losses P_L inside the channels of the capacitor plates composed of parallel sheets spaced δ:

$$P_L = \frac{32 \cdot \pi \cdot R_d^2 \cdot \eta \cdot l \cdot \left(\bar{v}/\sqrt{2}\right)^2}{\delta^2} \qquad (4—32)$$

where η is the Helium dynamic viscosity. Therefore the output power to be optimized is:

$$P = P_0 - P_L \qquad (4—33)$$

Moreover, starting from the capacitance of the plates-gas system, the voltage V to be applied to the plates, in order to maintain the cloud of charges in equilibrium into the gas, has been derived:

$$\mathrm{V} = \frac{\delta R_d}{2\varepsilon_0 \beta} \rho_q \qquad (4—34)$$

where ε_0 is the vacuum electric permittivity, and β is the ratio between the active interface-surface and the lateral surface of the plates of the capacitor, which is related to the surface/volume ratio of the capacitor.

It can be demonstrated that β is related to the duct radius R_d and to the distance δ among the sheets according to the following relation

$$\beta = \frac{16 R_d}{\pi^2 \delta} + 1$$

Here, once the average charge density ρ_q confined inside the capacitor is fixed, the needed voltage grows with the duct radius and the distance between the capacitor layers, while it is limited by the value of β. By applying a high voltage, a large quantity of charge carriers participates to generate the electrical current, with benefit to the output power. On the other hand, the dielectric

strength of the insulating coating puts an upper bound to the voltage that can be applied. In order to limit the applied voltage, the two plates of the capacitor should have a high surface/volume ratio, which allows to increase the capacitance, and then to reduce the voltage, without increasing the size of the device. High β means high outlet power, so that the optimization procedure will certainly tend to maximize β. Low values of the distance between the sheets of the capacitor (then a high number of layers constituting the plates) are positive for the applied voltage minimization because this is directly proportional to δ. In order to increase the charge stored in the plates, and then the released power, we are interested to maximize the number of sheets inside the duct. However, the velocity profiles during the vibration represent a strict constraint to the value of δ. If the gap between two sheets is less than twice the viscous boundary layer, the motion of charges is strongly limited; therefore, concentrating an excessive quantity of charge might be not advantageous.

Finally, once selected the materials, mass and the size limiting become of basic interest for some applications such as aerospace. Actually, the total mass of the device could be roughly considered as coincident to the mass of the magnetic core, so that:

$$M = \rho \cdot \Sigma \cdot 2\pi \left(R_d + \frac{R_x}{2} \right) \qquad (4—35)$$

where ρ is the mass density of the material constituting the torus. Once chosen the material for the magnetic core, the mass density is set and the mass of the device will depend approximately only on the medium radius ($R_d + \frac{R_x}{2}$) and on the cross-section Σ of the toroidal core.

All the calculations have been performed using an Intel Core i7-6560U CPU with 16 GB of RAM running under Windows 10 Professional.

First, a bi-dimensional optimization problem has been solved considering as objective functions the output power P to be maximized and the voltage V to be minimized. The Pareto-optimal list **P** permits to store a limited number of not dominated solutions. The algorithm stops when the list is full or when the maximum number of iterations is reached. For the calculation of the function f_2 the values λ=100 and γ=33 have been selected in order to uniformly sample the Pareto front.

The MO-TS optimization procedure is able to find a sampling of the Pareto front (Fig. 37) composed by 56 Pareto optimal solutions after 200 iterations and 200 000 000 computations of objective function with a computation time of 15 min. As can be noted, the algorithm is able to find uniformly sampled Pareto optimal solutions which span in a range of [78 – 5982] W, and [16.8 –

56.54] kV. Further fitness sharing functions would be used to choose among the optimal solutions [78].

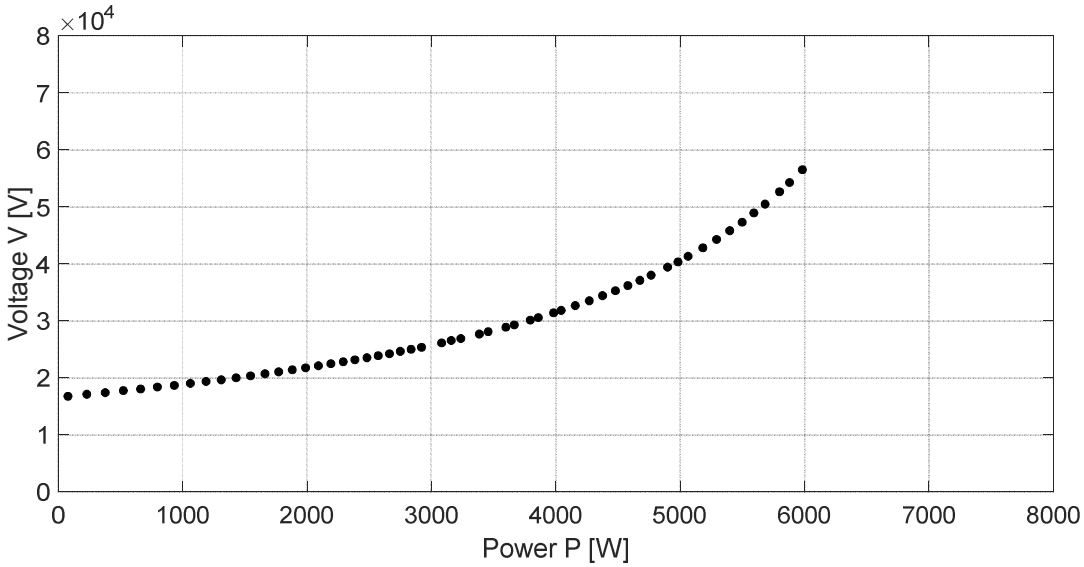

Fig. 37. Bi-dimensional Pareto Front

All the points of the obtained Pareto front correspond in the design space to the maximum values of the first three parameters, i.e., f equal to 1 [kHz] and both R_x and R_d equal to 30 [cm]. The only design parameter that changes is the ratio y that varies between 10.9 and 20, which corresponds to a number of parallel sheets in the capacitor comprised between 1052 and 1931.

Successively, all the three objective functions have been considered and a new MO-TS optimization problem has been solved. Fig. 38 shows the Pareto front in the 3-dimensional space of the objective functions.

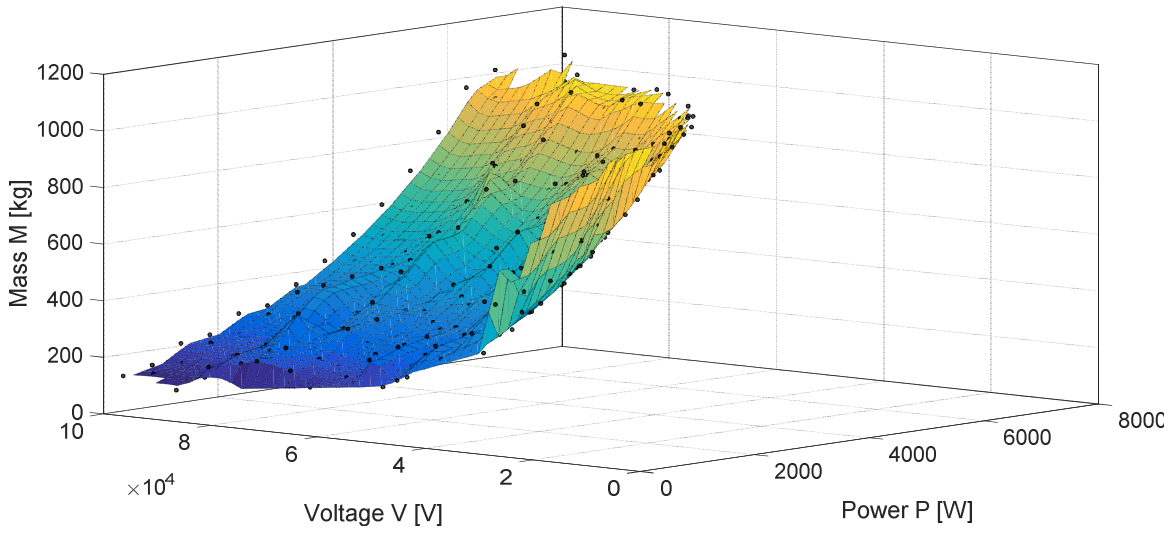

Fig. 38. Tri-dimensional Pareto Front

In this case, for the calculation of the function f_2 the values λ=500 and γ=167 have been chosen and 243 Pareto optimal solutions have been obtained with a computation time of 3 h. The obtained front is still quite uniform and the optimal solutions spam in a range of [9-6763] W, [20-100] kV, and [110-1106] kg, confirming the suitability of the proposed generator for aerospace applications [60].

In Table 8 some Pareto solutions and the corresponding design parameters values are reported. For example, if a supply power of about 3 [kW] is required for the on-board instrumentation, the minimum mass of the device will be about 514 [kg] and the voltage to be applied to the plates of the capacitor will be about 60 [kV]. On the other hand, by limiting the power at 1 [kW], a great advantage is obtained in terms of mass of the generator and voltage. Finally, it is possible to obtain the maximum power with larger values of mass (1021 [kg]) and voltage (68 [kV]).

Table 8. Values of the objective functions and of the corresponding design parameters

Power P [W]	**Voltage E_0 [kV]**	**Mass M [kg]**	**R_d [cm]**	**R_x [cm]**	***y***	***f* [Hz]**
2985	59.89	514.3	28.5	16.9	20.49	990.65
1091.72	44.41	359.5	27.2	13	17.72	999.98
6318.4	68.64	1021	30	28	22.036	1000

If, for a fixed power, a further reduced mass of the device is requested, magnetic materials with higher permeability, such as supermalloy [65], can be used for the torus. It must be considered that, due to ferromagnetic core saturation, the achievable mass reduction will not be directly proportional to the increase of the permeability.

The obtained results show that the proposed algorithm is able to sample the approximate optimal Pareto front with a chosen number of sampling points. The uniformity of the sampled Pareto front is good and MO-TS algorithm performs very well in terms of computational cost. The results are very useful for the designers because they are the expression of a multi-purpose optimization, where one can choose different functioning points depending on the specific application.

5 Conclusions

The first part of this thesis deals with the description of two different innovative concepts of MHD inductive generator aiming overcoming the main drawbacks of conventional MHD generators, such as the need to operate at high temperatures and to have superconducting coils for the generation of the external magnetic field, but at the same time holding all their advantages, such as the static conversion of the energy and the capability to work with very high temperatures.

In chapter 3 the Flowing MHD Induction technology is described, then a sensitivity analysis of the system performance is reported and a preliminary dimensioning of the generator is performed. The process is described and analysed by means of a mathematical model that has been solved in Simulink® environment. First, a parametric sweep of the velocity of the working gas and of the electrical load allowed evaluating the sensitivity of voltage and transferred power to those parameters. Then, another simulation has been carried out, performing a preliminary dimensioning of the generator and giving an order of magnitude of the performance and of its sensitivity to the design parameters. The results of the simulation are particularized with respect to the evolution of the charge distribution during the time, of the voltage applied to the electrical load and of the power transmitted. The active time is very short, but considerable values of voltage and power are reached. On the other hand, the time necessary to clean the duct from the charge carriers is much longer than the active time, because the thrust of repulsive force is very strong, especially when the charge is much concentrated. After a time of 0.5 [ms] a part of charges have not still overtaken the zero abscissa, corresponding to the toroidal coil. This affects the feasible rate of the ionization discharges, because we need to avoid interferences between consecutive clouds. This at the end affects the average power of the generator, and then all the influencing design parameters have to be stated carefully. The results of the simulation are in good agreement with the expected behaviour of the generator. Furthermore, the equation model of the system provides useful suggestions for the generator optimal design.

Chapter 4 deals with the TA-MHD Induction generator and its functioning characteristics. A theoretical study, developed in order to perform a coarse sizing and a performance estimation of the generator for a given set of parameters, has been used for the implementation of a series of FEM analysis. The results of Acoustic FEM analysis confirm the velocity profiles from literature [72], while the Electrostatic analysis allows finding the optimal voltage to be applied in order to ensure a

stable charges segregation. The FEM multi-physics analysis investigated the behaviour of charge carriers under the action of a mechanical vibration and of an external electrostatic field. This specific problem is of paramount importance for the feasibility of the TA-MHD electric generator which exploits thermo-acoustic effect and magneto-hydrodynamics in order to statically convert heat into electrical energy. The feasibility of this energy conversion process depends on how the unbalanced charge carriers spread into the volume where the electrostatic field is applied. The simulation results show that the charge carriers are segregated inside the volume where the electric field is applied, but they do not stick to the capacitor plates' walls, forming a charge free layer as reported in literature [30]. As a consequence, the charge carriers have high possibility to be involved in the vibration motion, giving rise to an alternate current which makes possible the transfer of energy by means of the electromagnetic induction.

Finally, the MO-TS algorithm proposed in [20] [22] has been customized in order to investigate the design alternatives for the MHD section of the TA-MHD electric generator. First of all, a bi-dimensional problem has been solved in order to simultaneously maximize the generated power and minimize the voltage necessary to maintain the charge segregation. Secondly, the minimization of the mass of the device has been introduced as a third objective function, so that the MOP has been solved for Space oriented applications. The obtained results show that the proposed algorithm is able to sample uniformly the Pareto front of the optimal solutions and performs very well in terms of computational cost. The results of the optimization are very useful for the designers because they are the expression of a multi-purpose optimization, where different functioning points can be chosen depending on the specific application.

If on the one hand, the proposed technologies make possible avoiding the typical drawbacks of conventional MHD generators which have limited until now their use; on the other, the new design concept requires adaptation of known Models, for studying both electromagnetic and fluid dynamic phenomena. The preliminary study conducted during this thesis work show that, from the point of view of the applied voltage and of the transferred power, the proposed energy converters could be effective for industrial applications (e.g. by using a multi-stage modular system) as well as for aerospace.

Bibliography

[1] Alemany A., Krauze A., Al Radi M., **Thermo acoustic-MHD electrical generator.** *Energy Proceedia*, Vol.6, 2011.

[2] Alemany A., Carcangiu S., Forcinetti R., Montisci A., Roux J. P., **Feasibility analysis of an MHD inductive generator coupled with a thermo acoustic resonator**. *Magnetohydrodynamics*; Vol.51, No.3, p. 531-542, University of Latvia, 2015.

[3] Alemany A., Carcangiu S., Forcinetti R., Montisci A., **Charge confinement for a Thermoacoustic driven MHD generator**. *In Proceedings of 10th PAMIR International Conference, Fundamental and Applied MHD*, p. 611-615, University of Cagliari, Italy, 2016.

[4] Alexeff I., Brickey J. and Mitchell S., **An electrodeless AC MHD generator and pump.** *In Proc. IEEE Int. Conf. on Plasma Science*, Oakland, CA (USA), p. 114-115, 1990.

[5] Alotto P., Nervi M. A. **An efficient algorithm for the optimization of problems with several local minima.** *Int. J. Numer. Methods Eng.*, Vol.50, p. 847–868, 2001.

[6] Backhaus S., Garrett S., **The power of sound.** *American Scientist*, Vol.88, p. 516-525, 2000.

[7] Backhaus S., Swift G. W., **A Thermoacoustic-Stirling heat engine: Detailed study.** Nature, Vol. 107, Issue 6, p. 3148-3166, *The Journal of the Acoustical Society of America*, 2000.

[8] Backhaus S., Tward E., Petach M., **Thermo-acoustic power systems for space applications.** *In: AIP Conference Proceedings*, Vol.608, p. 939-944, 2002.

[9] Backhaus S., Swift G. W., **New Varieties of Thermoacoustic Engines**. *In Proceedings of the 9th International Congress on Sound and Vibration*, Orlando, Florida, USA, 2002.

[10] Backhaus S., Tward E., Petach M., **Traveling-wave thermo-acoustic electric generator.** *Applied Physics Letters*, Vol.85, No.6, p. 1085-1087, 2004.

[11] Biesheuvel P. M., Bazant M. Z., **Nonlinear dynamics of capacitive charging and desalination by porous electrodes.** *Physical Review E, Statist Nonlinear Soft Matter Phys*, Vol.81, No.3, p. 031502–031512, 2010.

[12] Blackstock D. T., **Fundamentals of Physical Acoustics.** *Wiley-Interscience*, 2000.

[13] Bullard G. L., Sierra-Alcazar H. B., Lee H. L., Morris J. L., **Operating principles of the ultracapacitor.** *IEEE Trans. on Magnetics*, Vol.25, No.1, 1989.

[14] Canova A., Gruosso G., Repetto M., **Magnetic design optimization and objective function approximation.** *IEEE Trans. Mag.*, Vol.39, No.5, p. 2154–2162, 2003.

[15] Carcangiu S., Di Barba P., Fanni A., Mognaschi M.E., Montisci A., **Comparison of multi-objective optimisation approaches for inverse magnetostatic problems.** *Compel*, Vol.26, No.2, p. 293-305, 2007.

[16] Carcangiu S., Montisci A., Pintus R., **Performance analysis of an inductive MHD generator.** *Magnetohydrodynamics*, Vol.48, No.1, p.3–11, 2012.

[17] Carcangiu S., Montisci A., **Assessment of the machine parameters affecting the overall performance of an inductive MHD generator.** *In Proceedings of IEEE ENERGYCON*, Florence (Italy), 2012.

[18] Carcangiu S., Forcinetti R., Montisci A., **A Simulink Modelization of an Inductive MHD Generator.** *In Proceedings of 9th PAMIR International Conference, Fundamental and Applied MHD*, *Thermo acoustic and Space technologies*, Vol.1, p. 368–372, University of Latvia, 2014.

[19] Carcangiu S., Forcinetti R., Montisci A., **Simulink Model as a tool for the optimization of an Inductive MHD generator.** *In Proceedings of the 10th PAMIR International Conference, Fundamental and Applied MHD*, p. 616-620, DIEE, Cagliari, Italy, 2016.

[20] Carcangiu S., Fanni A., Montisci A., **Multiobjective Tabu Search Algorithms for Optimal Design of Electromagnetic Devices.** *IEEE Transactions on Magnetics*, Vol.44, No.6, p. 970-973, 2008.

[21] Carcangiu S., Forcinetti R., Montisci A., **Multiphysics Analysis of a Thermo Acoustic MHD Inductive Generator**. *In Proceedings of the European COMSOL® Conference,* Grenoble, France, 2015.

[22] Carcangiu S., Fanni A., Forcinetti R., Montisci A., **Multi-objective Tabu Search algorithm for the optimal design of a Thermo-Acoustic Magneto-Hydro-Dynamic electric generator.** *In Proceedings of the IEEE International Workshop on Optimization and Inverse Problems in Electromagnetism*, OIPE 2016, Rome, Italy, 2016.

[23] Ceperley P. H., **A pistonless Stirling engine–The traveling wave heat engine.** *Journal of the Acoustical Society of America*, Vol.66, p. 1508-1513, 1979.

[24] Ceperley P.H., **Gain and efficiency of a short traveling wave heat engine.** *Journal of the Acoustical Society of America*, Vol.77, p. 1239–1244, 1985.

[25] Cherubini D., Fanni A., Montisci A., Testoni P., **Inversion of MLP neural network for direct solution of inverse problems.** *IEEE Trans. Mag.*, Vol.41, No.5, p. 1784–1787, 2005.

[26] Cicconardi S. P., Perna A., **Performance Analysis of Integrated Systems based on MHD Generators.** *Energy Procedia*, Vol.45, p. 1305-1314, 2014.

[27] Coelho L., Alotto P., **Multiobjective Electromagnetic Optimization Based on a Nondominated Sorting Genetic Approach With a Chaotic Crossover Operator.** *IEEE Trans. Mag.*, Vol.44, No.6, 2008.

[28] Coelho L., Alotto P., **Gaussian Artificial Bee Colony Algorithm Approach Applied to Loney's Solenoid Benchmark Problem.** *IEEE Trans. Mag.*, Vol.47, No.5, 2011.

[29] Deb K., **Multi-objective optimization**. In *Search methodologies*, p. 403-449, Springer US, 2014.

[30] Delgado A.V., González-Caballero F., Hunter R. J., Koopal L. K., Lyklema J., **Measurement and interpretation of electrokinetic phenomena.** *Pure and Applied Chemistry*, Vol.77, No.10, 2005.

[31] Evans J. W., **The use of electromagnetic casting for AI alloys and other metals.** *The Journal of the Minerals, Metals & Materials Society*, Vol.47, No.5, p. 38–41, 1995.

[32] Garrett S., **Thermoacoustic Engines and Refrigerators**. *In Proceedings of the 13th French Acoustics Congress, CFA/VISHNO*, Le Mans, 2016.

[33] Hardianto T., Sakamoto N. and Harada N., **Three-Dimensional Flow Analysis in a Faraday-Type MHD Generator.** *IEEE Transactions on Industry Applications*, Vol.4, No.4, p. 1116-11234, 2008.

[34] Hosler W. R.; Negas T.; Schneider S. J., **Development, testing and evaluation of MHD-materials.** *National Bureau of Standards Internal Report (NBSIR)* 78-1461, June 1978.

[35] Hott R., Kleiner R., Wolf T., Zwicknagl G., **Review on Superconducting Materials.** *In Applied Superconductivity: Handbook on Devices and Applications.* Paul Siedel Editor, Wiley-VCH, p. 26-48, 2015.

[36] Hu L., Kobayashi H., Okuno Y., **Analyses on response of a liquid metal MHD power generation system to various external inputs.** *IEEJ Transactions on Electrical and Electronic Engineering*, Vol.10, No.3, 2015.

[37] Kamarul A. A. K., Thye J. L., Khairudin M., **Review on Thermionic Energy Converters**. *IEEE Transactions on Electron Devices*, Vol.63, No.6, p. 2231-2241, 2016.

[38] Kapooria, R. K., **Possible developments in energy conversion using liquid metal magnetohydrodynamics.** *Journal of Energy in Southern Africa*, Vol.20, No.2, p.17-25, 2009.

[39] Kaushik S.C., Verma S.S., Chandra A., **Solar-assisted liquid metal MHD power generation: A state of the art study.** *Heat Recovery Systems and CHP*, Vol.15, No.7, p. 675-689, 1995.

[40] Kayukawa N., **Comparisons of MHD topping combined power generation systems.** *Energy Conversion & Management*, Vol.41, p. 1953-1974, Elsevier, 2000.

[41] Khan S. U., Yang S., Wang L., Liu L., **A Modified Particle Swarm Optimization Algorithm for Global Optimizations of Inverse Problems.** *IEEE Trans. Mag.*, Vol.53, No.3, 2016.

[42] Kim H. R., Lee Y. B., **MHD stability analysis of a liquid sodium flow at the annular gap of an EM pump**. *Annals of Nuclear Energy*, Vol.43, p. 8–12, 2012.

[43] Koester J., Perkins R., **Discharge and corrosion characteristics of slagging metal electrodes for MHD power generator.** *En. J. of Materials for Energy Systems*, Vol.1, No.2, 1979.

[44] Kogelschatz U., **Dielectric-barrier Discharges: Their History, Discharge Physics, and Industrial Applications.** *Plasma Chemistry & Plasma Processing*, Vol.23, No.1, 2003.

[45] Lou G. and Okuno Y., **Numerical simulation of non-equilibrium plasma in Closed-Cycle MHD generator.** *In Proc. of the 2nd International Conference on Computer and Automation Engineering, ICCAE*, Singapore, p. 36-39, 2010.

[46] McDaniel E. W., **Collision phenomena in ionized gases.** Wiley, N.Y., 1964.

[47] McLaughlin B. J., **Study and development of high frequency thermoacoustic prime movers with piezoelectric transducers.** *Dissertation Abstracts International*, Vol.69, No.4, Section: B, p. 2368, 165 pages, 2008.

[48] Messerle H. K., **Magnetohydrodynamic Electrical Power Generation.** *UNESCO Energy Engineering Series*, John Wiley & Sons Ltd, England, 1995.

[49] Montisci A., Pintus R., **Sensitivity Analysis of Design Parameters of an inductive MHD Generator.** *20th International Symposium on Power Electronics, Electrical Drivers, Automation and Motion*, Pisa, Italy, 2010.

[50] Montisci A., Pintus R., **A Magnetohydrodynamic study of a inductive MHD generator**. *The European COMSOL Conference*, Milano, Italy, 2009.

[51] Montisci A., Pintus R., **Feasibility analysis and conceptual design of a inductive MHD Generator.** *The 8th International Symposium on Electric and Magnetic Fields, EMF 2009*, Mondovì, Italy, 2009.

[52] Moreau R., **Magnetohydrodynamics.** *Fluid Mechanics and its applications*, Vol.3, Kluwer Academic Publishers, The Netherlands, 2010.

[53] Nimvari M. E. et al, **Analysis of triple combined cycle with MHD generator as a topping cycle.** *Proceedings of the 3rd Conference on Thermal Power Plants (CTPP)*, p. 1-5, 2011.

[54] Novotny P., Vit T., Vestfalova M., Lopes J., **Standing-Wave Thermoacoustic Engines**. *EPJ Web of Conferences_EFM2011*, Vol.25, n° 01061, EDP Sciences, 2012.

[55] Okuo T., Aoki Y., Yatsu S., Oikawa S., Kitagawa H., Kayukawa N., Tuchida B., Nishimura R., Yagi M. and Yoshizaki I., **Heavy metal electrodes development for coal-fired MHD generator channels.** *In Proc. IEEE Int. Conf. on Plasma Science*, USA, p. 115, 1990.

[56] Patent Application No. PCT/EP2014/074866, Publication No. WO/2015/071485, https://patentscope.wipo.int/search/en/detail.jsf?docId=WO2015071485.

[57] Petersen H. **The Properties of Helium**. *Danish Atomic Energy Commission*, Rep. No.224, 1970.

[58] Pintauro P. N., **Perspectives on Membranes and Separators for Electrochemical Energy Conversion, and Storage Devices.** *Polymer Reviews*, Vol.55, 2015.

[59] Pintus R. **Development of an Inductive Magnetohydrodynamic Generator.** *PhD Thesis*. University of Cagliari, Italy, A.A. 2009/2010.

[60] Rapp D., Surampudi S., Nesmith B., Mondt J., **Advanced Radioisotope Power System Technology Development for NASA Missions 2011 and Beyond.** *Proc. of 6th European Space Power Conf.*, Porto, Portugal, May 6-10, 2002.

[61] Rosa R. J., **Magnetohydrodynamic Energy Conversion.** *Hemisphere Publishing*, Washington, D.C., 1987.

[62] Rosa R. J. et al., **Plasmas in MHD power generation.** *IEEE Trans. Plasma Sc.*, Vol.19, No.6, 1991.

[63] Sasaki T., Kikuchi T. and Harada N., **Temperature measurement of noble and combustion gas plasmas with optical measurement system for MHD generators.** *In Proc. of the IEEE International Conference on Plasma Science*, San Diego, CA (USA), p. 1-1, 2009.

[64] Shercliff J. A., **A Textbook of Magnetohydrodynamics.** Pergamon Press, 1965.

[65] Shokrollahi H., **The magnetic and structural properties of the most important alloys of iron produced by mechanical alloying.** *Materials & Design*, Elsevier, Vol.30, p. 3374-3387, 2009.

[66] Singh G. K., **Solar power generation by PV (photovoltaic) technology: A review.** *Energy*, Vol.53, p. 1-13, 2013.

[67] Slavin V. S., Bakos G. C., Milovidova T. A. and Finnikov K. A., **Space power installation based on solar radiation collector and MHD generator.** *IEEE Transactions on Energy Conversion*, Vol.21, No.2, p. 491-503, 2006.

[68] Space TRIPS project. **Space Trips: The Up To Date Situation.** Available on line. http://space-trips.eu.seventhframework.sal.lv/wp-content/uploads/2015/06/Space-TRIPS-up-to-date.pdf

[69] Strutt J. W. (Lord Rayleigh), **The Explanation of Certain Acoustical Phenomena.** *Nature*, Vol.18, No.455, p. 319-321, 1878.

[70] Swift G. W., **Thermoacoustics**. *Springer Handbook of Acoustics*, Ch 7, p. 239-255, Editor: Prof. Thomas D. Rossing, Springer, 2007.

[71] Takahashi N., Muramatsu K., Natsumeda M., Ohashi K., Miyata K., Sayama K., **Solution of problem 25 (Optimization of die press model).** *In Proc. ICEF'96*, China, p. 383–386, 1996.

[72] Tijdeman H., **On the propagation of sound waves in cylindrical tubes.** *Journal of Sound and Vibration*, Vol.39, p. 1-33, 1975.

[73] Tsu T. C., **MHD power generators in central stations.** *IEEESpectrum*, Vol.4, No.6, p. 59-65, 1967.

[74] Vielstich W., **Handbook of Fuel Cells, 6 Volume Set.** Wiley, 2009.

[75] Voshall R. E., Wright R. J. and Liebermann R. W., **Design of Closed-Cycle MHD Generator with Nonequilibrium Ionization and System.** *IEEE Transactions on Plasma Science*, Vol.5, No.2, p. 110-122, 1977.

[76] Wang K., Sun D., Zhang J., Xu Y., Zou J., Wu K., Qiu L., Huang Z., **Operating characteristics and performance improvements of a 500 W traveling-wave thermoacoustic electric generator.** *Applied Energy*, Vol.160, p. 853-862, 2015.

[77] Yamato 1. February 2008. In **Wikipedia**. Retrieved December 20, 2016.

https://upload.wikimedia.org/wikipedia/commons/0/0d/Yamato_1_from_the_front.JPG

[78] Yang S. Y. et al., **An improved tabu based vector optimal algorithm for design optimizations of electromagnetic devices.** *IEEE Trans. Mag.*, Vol.40, No.2, p. 1140–1143, 2004.

[79] Zohm H., **Magnetohydrodynamic Stability of Tokamaks.** Wiley, 2015.

PART II

6 Magneto Plasma Sail

6.1 Introduction

The second part of this thesis deals with the theoretical study and the qualitative simulation of the formation process of the *Magneto Plasma Sail* (MPS). This propulsion system, by using a very small coil of current, is able to generate a very wide magnetosphere, which is able to thrust a spacecraft exploiting the energy of the solar wind, exactly as a sail drives a boat. Starting from the existing literature, first, the Solar Sail, the Magnetic Sail and the Magneto Plasma Sail propulsion concepts are defined and then the Magneto Plasma Sail is compared with other spacecraft propulsion systems. Finally, a Finite Element Analysis is performed, aiming to demonstrate the occurrence of the phenomena on which the MPS system is based on, namely the inflation of the magnetic sail produced by the injection of plasma, and the interaction of the sail with the solar wind.

6.2 Generalities

In the last three decades, a number of studies have been conducted about the proof of concept of the MPS propulsion system, which aims to harvest energy from the solar wind. The Sun releases continuously the solar wind, a fully ionized plasma of hydrogen, at a very high velocity which can reach a mean value of 400 km/s at 1 AU (about 150 million kilometers, roughly the distance Sun-Earth) [14]. At the same time, the Sun emits electromagnetic energy associated to the light radiation. Several studies have been carried out, in order to assess the feasibility of spacecraft propulsion systems which exploit such energy flow coming from the Sun.

The first proposed concept of solar sail is the so called *Photonic Solar Sail* [7] [13], which picks up the driving momentum from the reflection of the photons. Such device needs to deploy a very big physical surface in order to harvest the photon radiation pressure and thus create lift. The system brings its own advantages and drawbacks; on the one hand, the easy operability and the almost total absence of power supply, on the other hand, the deployment of a very large sail is troublesome and brings mass and fragility issues [30]. Existing solar sails consist of a thin film of aluminum on a polymer backing, with areas from 4 000 to 15 000 [m^2], and can provide a net force around 25-75 [mN] [30].

A second concept design is represented by the *Magnetic Solar Sails* [40]. This system, exploiting the flow of matter, rather than the solar radiation, consists in a very large coil of superconductive wire carrying an electric current. As the solar wind is fully ionized, the magnetic field generated by the coil diverts the wind particles, exerting for reaction a thrust on the spacecraft Fig. 39. The wire is powered initially with a trigger current, and then it can be maintained without providing external energy, excepted for the consumption of the cryogenic system for the superconductor cooling. The solar wind have a very high velocity, but its density is very low (more or less, six charges per cubic centimeter) [14], therefore the sail needs to be very wide to produce a reasonable thrust. In [28] [40] some estimations are performed giving for the coil diameter a magnitude of the order of 100-200 [km]. The main drawback of this system is that it is fairly massive (in the order of few metric tons) so that it presents technical and economical limits [30].

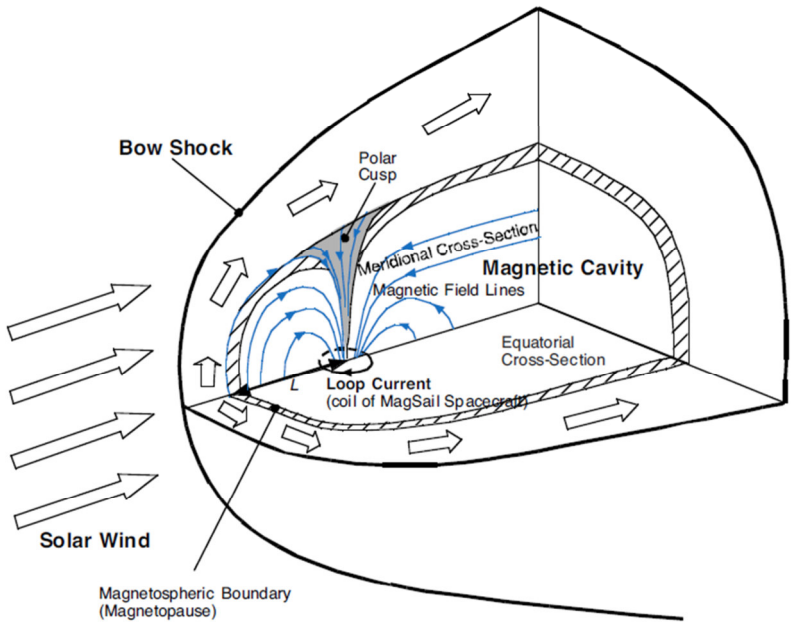

Fig. 39. Solar wind flow and magnetic field of a Magnetic Sail [11]

Afterwards, in [29] [30] [31] [32] [33] [34] [35] [39] has been proposed to inject a plasma flux at the center of a small coil with the goal to strengthen the imposed magnetic field. In particular conditions (high magnetic Reynolds number) the plasma jet strongly affects the magnetic field force lines, enabling the magnetic field extension far away from the aircraft, up to distances greater than for a simple dipole. This is the so called *Mini Magnetospheric Plasma Propulsion system* (M2P2) or *Magneto Plasma Sail* (MPS), which is driven by the same concept of the *Magnetic Solar Sail,* using a magnetic field to deflect the charges carried by the solar wind and obtaining as a reaction a thrust, which is transmitted to the spacecraft (see Fig. 40).

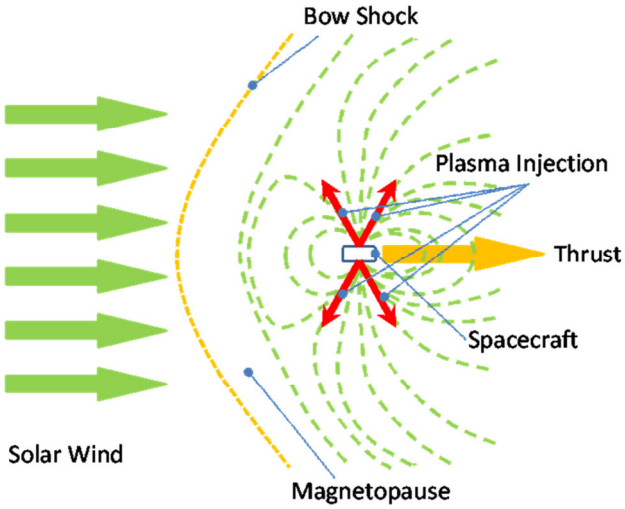

Fig. 40. Magneto Plasma Sail

The M2P2 system introduces manifold of strengths. First of all, it uses electromagnetic processes to produce obstacle to the solar wind, then the main technical problems of the existing solar sails are removed. Secondly, large scale interaction cross section can be obtained with low weight and low power requirements. Thirdly, whereas the classical magneto solar sails oppose a constant blocking area to the solar wind flow and, therefore, provide variable thrust, the MPS system acts as a balloon and it expands as the solar wind dynamic pressure reduces, providing a constant acceleration to the spacecraft as it moves away from the Sun. Finally, the M2P2 system could be characterized by the specific impulse, which is the amount of gas consumed per Newton second of thrust, usually used for the rocket propulsion systems comparison [30].

6.3 Existing space propulsion technologies: a comparison

During the last thirty years, many Space Agencies in the world have increased their efforts on the development of systems for Space exploration [3] [4] [6] [11] [12] [19] [28] [37] [40]. On the one hand, there are several reasons which make strategic this research from both a scientific and an industrial point of view. On the other hand, many issues remain unsolved, one of the most important being the thrust to weight ratio achievable by the propulsion system. To give an order of magnitude, the cost to send half of a kilogram of payload into Earth orbit with conventional rockets is roughly ten thousand dollars [4]. This high price is one of the reasons why saving spacecraft's mass is of priority interest for the Space designers.

Chemical rockets and electric thrusters rely on the same basic functioning principle. They propel a space vehicle by accelerating and ejecting an exhaust, so that the comparison can be done starting from the well-known thrust equation and rocket equation [12].

Classical chemical rockets can reach a not very high exhaust speed (3-4 km/s), restricted by the amount of energy released by known chemical reactions with known propellants, and by the limited achievable temperature linked to the melting point of the materials [4]. If on the one hand chemical rockets are energy limited, because they can work for only short periods due to the very high energy consumption rate, on the other hand they can furnish a very high power level, thus a strong thrust (in the order of MN) [4] [6]. The speed necessary to reach the heliopause in 10 years (around 50 [km/s]) cannot be attained by this type of propellers without an unacceptable fuel consumption, because the fuel to payload ratio increases exponentially according to the rocket equation [12], so they are suitable only for short term missions [4].

Electric thrusters (Ion, Hall and Plasma thrusters) use as exhaust a plasma produced and accelerated to very high velocities (10-10^3 [km/s]) [12]) by electric or magnetic fields. These devices are power limited, because the rate at which the energy can be transmitted to the propellant is limited by its own mass [6], so they can reach low thrust (from 20 [mN], to some dozen of N) and low acceleration [4]. They are not energy limited because, theoretically, an arbitrarily large amount of energy can be delivered to a given mass of propellant [6]. Due to the lower fuel consumption they can work for longer period than chemical rockets, so, even if they can generate much less thrust, in the frictionless environment of space, they can achieve greater speeds. Even if these features make electric rockets better equipped than chemical rockets for deep-space missions [4], the power requirements for those explorations are in the order of Megawatts [30]. Table 9 summarizes the main technical specifications of the cited propulsion systems compared with the theoretically estimated performance of the Magneto Plasma Sail (see section 0).

Table 9. Spacecraft engines comparison [4] [19] [30] [37]

	Chemical thruster	**Ion engine**	**Solar Sail (square 100 [m^2])**	**MPS (L=10[km])**
Propellant	Various: liquid and solid	Xe, Bi, Cs	No propellant	Xe, Ar, etc.
Exhaust velocity	2-5 [km/s]	10-50 [km/s]	No exhaust	1-10 [km/s]
Specific Impulse [s]	150-450	3000-4500	infinity	Around 5000
Thrust	10^6 [N]	20-500 [mN]	50 [mN]	1 [N]
Acceleration	5-90 [m/s^2]	5-10 [mm/s^2]	0.1 [mm/s^2]	10 [mm/s^2]
Thrust to power ratio	-	0.02-0.04 [N/kW]	-	0.25 [N/kW]
Thrust to weight ratio	0.01-180	10^{-6}-10^{-4}	10^{-5}	10^{-3}
Fuel efficiency	35%	80%	-	100%
Target mission	Earth launches, Short term	Near-earth, Main-belt and Comet rendezvous	Near-earth, Main-belt and Comet rendezvous Fast outer planet flyby	Fast outer planet flyby Deep space

6.4 Analytical performance estimation

The M2P2 system needs essentially for three elements to work properly; e.g. by considering a spacecraft at 1 AU distance from the sun, fitted with a 10 [cm] radius coil, in order to produce coupling with the solar wind over a blocking region with a radius of about 15-20 [km], are needed:

- ✓ an electric current creating a relative strong magnetic field (~700 Gauss is announced in the first idea [29] [30]);
- ✓ a high density and high energy plasma injected from the spacecraft within the coil, in order to inflate the magnetic field;

- ✓ a power source of about 3 [kW] for the magnetic field supply and the inflating plasma generation [29] [30].

The feasibility of the system relies on the possibility to reduce the radial coil magnetic field decay thanks to the plasma injection. If the magnetic field is in frozen conditions (magnetic Reynolds number $R_m >> 1$), so that the magnetic force lines are heavily linked to the fluid flow, the injection of plasma can drag the magnetic field outwards, resulting in a decrease of the field with the inverse of the distance (r^{-1}), rather than with the inverse of the square (r^{-2}) (as happens in vacuum for dipole magnetic fields due to the Biot-Savart law). The energy of the injected plasma will support this decrease in the magnetic field falloff [30].

In order to obtain the needed outward stretching of the magnetic field under the action of the plasma jet, the plasma pressure at the injection point will be a non-negligible fraction of the pressure exerted in turn by the magnetic field. The ratio between these two pressures (or equivalently energy densities) is given by:

$$\beta_{eta} = \frac{Plasma\ dynamic\ pressure}{Magnetic\ field\ pressure} = \frac{\rho \cdot v^2}{B^2/2\mu_0} = \frac{n_{density} \cdot K_B \cdot T}{B^2/2\mu_0} \qquad (6—1)$$

where ρ is the plasma mass density, v is the plasma velocity, $n_{density}$ is the plasma number density, k_B is the Boltzmann constant, T is the plasma temperature, B is the magnetic induction module and μ_0 is the vacuum magnetic permeability.

The thrust increases as β_{eta} increases, but otherwise also the power consumption increase contemporarily, so that the ratio between thrust and fuel consumption globally decreases. Accordingly, as long as possible is needed a fairly low β_{eta} for the plasma injected inside the high magnetic field region inside the coil. ($\beta_{eta} \approx 10^{-2}$[28] [30], or $\beta_{eta} \approx 10^{-4}$ [10] [11]).

The described technology could intercept, with a sail extension around 10-20 [km] and a power consumption of about 3 [kW], more thrust than 1 [N] [29] [30]. Due to the very low energy requirement, it will be probably sufficient a radioisotope generator as source of electrical power, a well known technology already available for Space missions. The achieved thrust is enough to propel the spacecraft in the wind direction with very low energy requirements. The magnetic sail will propel a spacecraft 100-200 [kg] weighted (on-board instrumentation, plus payload and propellant) with accelerations of 0.01[m/s^2], attaining velocities from 50 to 75 km/s after three

months [29] [30]. Aiming to a consumption of 0.5 [kg/day] during the acceleration phase, the estimated fuel requirement is of 30 [kg] [30].

The theoretical estimation of the fuel requirements for the entire acceleration phase of three months has been obtained by taken into account the loss of the 100% of the injected plasma; i.e., the fuel consumption rate calculated analytically represents a maximum estimation. Actually, if the MHD interaction parameter (for its definition see MHD Mathematical Model on page 25) is much higher than 1, electromagnetic forces are prevailing on inertia forces, so that the fluid streamlines tend to be heavily modified by the magnetic field distribution, allowing, in optimal conditions, the confinement of the injected plasma, which means excellent fuel efficiency.

The described theoretical expectations are far superior to the capabilities of all existing Space propulsion systems and might allow reaching the outer solar system (100 AU from the Sun) in around a decade [29] [30], therefore the target application for the proposed device is the deep Space exploration (Kuiper belt, Pluto, solar system boundaries).

6.5 State of the art

6.5.1 Numerical Simulation

In the studies conducted by Winglee et al [29] [30] [35], a transient MHD simulation has been proposed with the aim to describe the system behavior (magnetic sail formation and its interaction with the solar wind) and to estimate the achievable thrust. The proposed multi-fluid treatment is based on the equations of MHD, but the dynamics of electrons and ions are kept separate.

The thrust acting on the spacecraft due to the deflection of the solar wind has been calculated through the application of the momentum conservation theorem.

The transient simulation was conducted according to two steps; during the first one the solar wind dynamic pressure reach approximately an equilibrium condition with the magnetic pressure exerted by the spacecraft coil field; then starts the injection of low-energy plasma and the solar wind tends to a new equilibrium. The process is repeated for multiples of the magnetic flux and of the plasma densities, so that the dimensions of the magnetosphere could be studied as a function of the magnetic field strength.

Since the expected size of the magnetic bubble is around 10^5 times than that of the spacecraft, in order to try to get realistic scaling between the different parts of the system, the considered mesh

has been broken into several subsystems, where the smaller furnishes the inlet conditions for the larger one.

Detailed analysis and extrapolation of the results allow the authors achieving some very interesting conclusions. The size of the magnetosphere is directly proportional to the imposed B field; e.g. for a 10 [cm] diameter solenoidal coil, it has been extrapolated that a coil magnetic field of 60-70 [mT] should be necessary to reach a 20 [km] radius for the magnetosphere. The results indicates also that only a few millinewtons of force (few kilowatts of energy) have to be spent in order to sustain the coil magnetic field and the relative inflating plasma, intercepting 1 [N] of force (megawatts of power) from the solar wind. The resulting force (energy) leverage will be of about three orders of magnitude.

The MHD numerical model developed by Winglee et al. [29] [30] [35] is well built, even if the used boundary conditions are difficult to be understood and even if the calculations are necessarily affected by the simplifying assumptions.

The Larmor radius, which is the radius of the circular motion of a charged particle in a magnetic field, is very different for ions and electrons, so that their trajectories are differently deflected by the electromagnetic forces. Impinging electrons and ions from the solar wind are thus dissociated at the magnetopause giving rise to an initially balanced local charge separation. Afterwards, electrons, which have a Larmor radius around three orders of magnitude lower than ions, tend to be thickened at the external edge of the magnetopause where they could be lost more easily than ions. Therefore the charge separation tends to become unbalanced, giving rise to an outward electric field, so that the electro neutrality assumption at the magnetopause level cannot be accepted.

Furthermore, it is well known that if $r_{Li} < L$, where r_{Li} is the ion Larmor radius and L is the characteristic dimension of the magnetosphere (e. g. the sub-solar standoff distance), ions will be reflected at the magnetospheric boundary; but if $r_{Li} > L$, ions won't be reflected and will penetrate deep into the magnetic cavity without producing thrust. As a result, small ratio r_{Li} / L is required to obtain a detectable deviation in the ions trajectory and then a significant thrust level in the MHD approximation.

The MHD hypothesis would be valid to describe the involved physics only if the Larmor radius of both electrons and ions could be negligible ($r_L < L$) compared with the characteristic dimension

of the magnetosphere [17], but in reality the ion Larmor radius is greater than or comparable to that size [10] [11] [15] [17].

This consideration leads to caution regarding the used pure MHD models. These models must necessarily take into account the separation of electrons and ions in the magnetosphere and thus the presence in this area of electrostatic forces. Separate equations for the motion of each elementary particle such as those used for particles in the cell (PIC) modeling [2] [8] [20] [24], are suitable for such differentiation, but, in counterpart, they introduce a high complexity, with a large number of unknowns, becoming very heavy to handle. Hybrid models still retain a portion of the fluid model in describing the physics of the system, but also take into account the particles inertia. Hybrid models like MHD/PIC [15] [16] [17] [36] allow approaching the solution with a degree of accuracy higher than simple MHD models, and with more acceptable computational costs with respect to full PIC simulations.

Due to these considerations, Khazanov [17] and Omidi [36] started with a different approach, developing their hybrid simulations with the same initial conditions as Winglee [29] [30]. Their results deviated from the MHD ones, or rather, they demonstrate that the achievable thrust with a 10 [km] magnetic sail was negligible and that a sail much larger than expected (>100 [km]) was necessary to achieve meaningful momentum transfer [17], with the related consequences (higher power consumption and higher weight of the system).

Table 10. Summary of simulations done under various studies [2]

Reference	Target	Dimension	Numerical model	Ions kinetics	Electrons kinetics
[21]	Magnetic sail	2D	MHD	-	-
[22]	M2P2	3D	MHD	-	-
[23]	Magnetic sail	2D	MHD	-	-
[17]	M2P2	3D	Hybrid-PIC	Considered	-
[36]	Plasma expansion	3D	Hybrid-PIC	Considered	-
[15]	M2P2	3D	Hybrid-PIC	Considered	-
[20]	Plasma expansion	2D	Full-PIC	Considered	Considered
[2]	Magnetic sail and M2P2	2D	Full-PIC	Considered	Considered

6.5.2 Experiments

The work conducted by Winglee et al. [31] [32] [33] [34] [35] [38] [39], investigated the performance of a M2P2 prototype opposed by an incoming plasma flow simulating the solar wind. The MPS setup consists of an electromagnet, at whose center a helicon source is positioned producing the inflating plasma, located at the one end of a cylindrical vacuum chamber.

The solar wind simulator, placed at the other end of the chamber, is a dual plasma source allowing the interaction to be studied for different power levels and shot duration. In order to identify the different plasma, M2P2 was run using Xenon (green emissions) as inflating plasma, while Argon (blue emissions) was usually used simulating the solar wind.

According to the authors, the results of the experiment demonstrate that the M2P2 is able to achieve all key functions that would enable it to efficiently tap energy from the solar wind.

First, the use of a helicon plasma source allows producing high-beta plasma within the M2P2 magnet. Second, the M2P2 system is able to absorb energy from the solar wind in the form of enhanced plasma density. Third, deflection of very energetic plasma sources despite the very low energy expended has been demonstrated. This is consistent with the initial predictions [30] that 1 [kW] MPS systems would be able to deflect several hundred [kW] plasma winds, producing propulsion for a spacecraft [35].

Summarizing, all key features of M2P2 needed for successful operation in Space have been demonstrated in the laboratory [35], even if for very short times, but no direct thrust measurements were done.

In [10] [11] [26] the first laboratory scale model experiments of the MPS were arranged with the aim to evaluate the thrust acting on the spacecraft due to the momentum transfer from the solar wind.

First a solenoidal coil placed in a vacuum chamber and subjected to a hydrogen plasma jet (which simulates the solar wind), reproduces the pure magnetic sail. The experiment confirms the formation of the magnetic cavity around the coil.

However, when the system has been tested with a plasma jet from the coil center, only the control over the magnetic cavity size has been demonstrated, but no meaningful thrust increase have been detected. This is because only a 10% inflation of the magnetic sail was obtained with the

plasma injection, which results, under the noisy conditions of the experiment, in an undetectable thrust increase.

Moreover, by comparing the experimental results with that given by hybrid simulations, the measured thrust is always lower than that calculated numerically (Fig. 41 and Fig. 42). This is because under the laboratory conditions there are much more collisions with neutrals, which limit the achievable thrust level, meaning that the laboratory experiment cannot predict the entire feature of collisionless plasmas in Space.

The goal for future experiments will be to increase the dimensions of the plasma test chamber and the power of the plasma source with the aim to obtain a higher inflation of the field, thus a larger magnetic cavity and a more clearly detectable thrust gain.

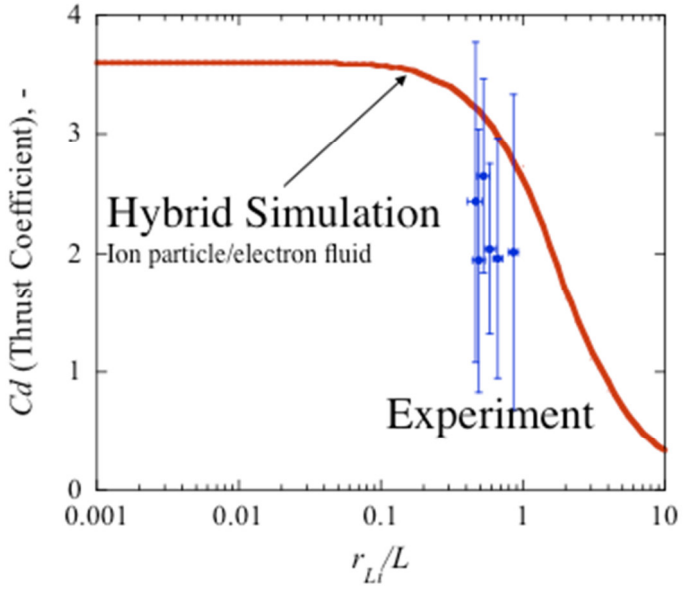

Fig. 41. Thrust coefficient evolution as a function of the ratio between the ion Larmor radius (r_{Li}) and the size of the magnetosphere (L): Comparison between hybrid simulation and experimental results [28].

The force F acting on the current loop depends on the area blocking the solar wind:

$$F = C_d \frac{1}{2} \rho v_{sw}^2 S_{block} \qquad (6—2)$$

where, $\frac{1}{2}\rho v_{sw}^2$ is the dynamic pressure exerted by the solar wind, v_{sw} is its velocity and ρ its density, $S_{block} = \pi L_{ssd}^2$ is the blocking area, L_{ssd} is the sub solar standoff distance.

Theoretically, the maximum achievable speed would be that of the solar wind itself, but the acceleration depends on the exerted thrust and on the weight of the spacecraft. The thrust coefficient

C_d is the only unknown in equation (6—2) and it is theoretically derived for various scales of Magnetic sail [1] [8] [21] [27].

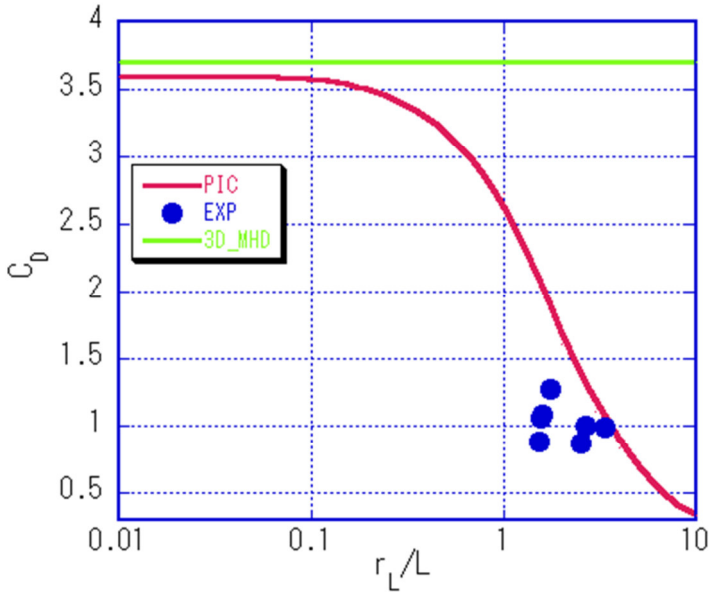

Fig. 42. Thrust coefficient evolution as a function of the ratio between the ion Larmor radius (r_{Li}) and the size of the magnetosphere (L): Comparison between MHD and PIC simulation and experimental results [18].

Table 11. Summary of the requirements for some experiments from literature

Reference	Ueno [26] [27] [28]	Funaki [10] [11]	Kojima [18]	Winglee [34] [35] [38]
Solar wind				Argon
Density	$1.24 \cdot 10^{19}$ m^{-3}	~10^{19} m^{-3}	$2 \cdot 10^{18}$ m^{-3}	$5 \cdot 10^{19}$ m^{-3}
Velocity	47 km/s	45 km/s	60 km/s	
Temperature	1 eV	1 eV	-	10-20 eV
Injection flow rate	-	0.4 g/s	-	
Runtime	1 ms	0.8 ms	0.7 ms	50 µs-1 ms
Plasma injection	Hydrogen	Hydrogen	-	Xenon
Density	$3.2 \cdot 10^{19}$ m^{-3}	$2 \cdot 10^{18}$ m^{-3}	-	10^{18} m^{-3}
Velocity	17.2 km/s	-	-	
Temperature	1 eV	-	-	10 eV
Injection flow rate	0.05 g/s	0,05 g/s	-	
Runtime	1 ms	0.8 ms	0.7 ms	2 ms
Coil	Solenoid	Solenoid	Solenoid	Electromagnet
Diameter	75 mm	50-75 mm	12 mm	20 cm

Number of turns	40	20		
Magnetic induction B at the coil center	0.06 T	1.8-2 T	1 T	0.05-0.2 [T]
Current intensity	0.14 kA	4.2 kA	-	
Current duration	0.9 ms	0.9 ms	0.9 ms	
Size of the magnetosphere	0.1 m	0.1 m	-	
Magnetic Reynolds number	20	12	-	
Measures	Thrust, Magnetic field	Thrust	Thrust	Magnetic field, Electric potential, Electron temperature, and density of plasma

6.6 FEM analysis of the magnetic sail formation process

6.6.1 Presentation of the problem

Magneto Plasma Sails aim to obtain thrust by the interaction between the solar wind and an on-board magnetic field expanded by a plasma injection. While there have been many studies on this revolutionary propulsion system, its real performance is still unclear. Currently, many experimental studies have been conducted on laboratory scale only for short periods and have not clearly evidenced thrust gain due to the plasma injection. At the same time, several researchers, mainly from USA and Japan, have developed different numerical models (MHD, PIC, Hybrid) to study the magnetic field inflation process and the interaction of the formed magnetic bubble with the solar wind [2] [8] [15] [16] [17] [20] [21] [22] [23] [30] [31]. The aim of this work is to implement a FEM analysis of the device starting from ideal MHD hypothesis, in order to assess the magnetic sail formation process, its inflation and its interaction with the solar wind.

6.6.2 Model main hypothesis

The MPS system combines several phenomena: fluid mechanics, electromagnetism, heat transfer, mass transport and plasma physics. As basic assumption, the involved plasma is only as a highly conducting fluid where the single charged particles are not distinguishable (MHD hypothesis). Therefore, a simplified 2D FEM analysis of the interaction among the magnetic field,

the injected plasma and the external solar wind has been performed observing the classical MHD model. Heat transfer and transport phenomena have been momentarily neglected. The studied 2D domain has been set as a square with a side of 10 [m]. A 20 [cm] diameter, single coil made by a 5 [mm] copper wire, representing the on-board magnetic field source, has been positioned at the center of the domain. The solar wind has been simulated by a fluid flow coming from the left side of the domain. The inflating plasma has been injected along the axial direction at the center of the coil when the interaction between the solar wind and the on-board magnetic field has reached stationary conditions. A triangular, extremely fine, physics-controlled mesh has been chosen (Fig. 43).

Table 12. Main properties of the working fluid

Parameter	**Description**	**Simulated values**
μ/μ_0	Relative magnetic permeability	1
$\varepsilon/\varepsilon_0$	Relative electric permittivity	1
σ [S/m]	Electric conductivity	10^8
η [Pa·s]	Dynamic viscosity	10^{-4}
γ_{heat}	Heat capacity ratio	1.4
k [W/(m·K)]	Thermal conductivity	k(T)
c [m/s]	Speed of sound	c(T)
ρ [kg/m^3]	Mass density	(p, T) (Perfect gas law)

The domain has been considered initially full of an ideal highly conductive compressible fluid at 293.15 [K] of temperature and 1 [atm] of background pressure, whose characteristics are summarized in Table 12.

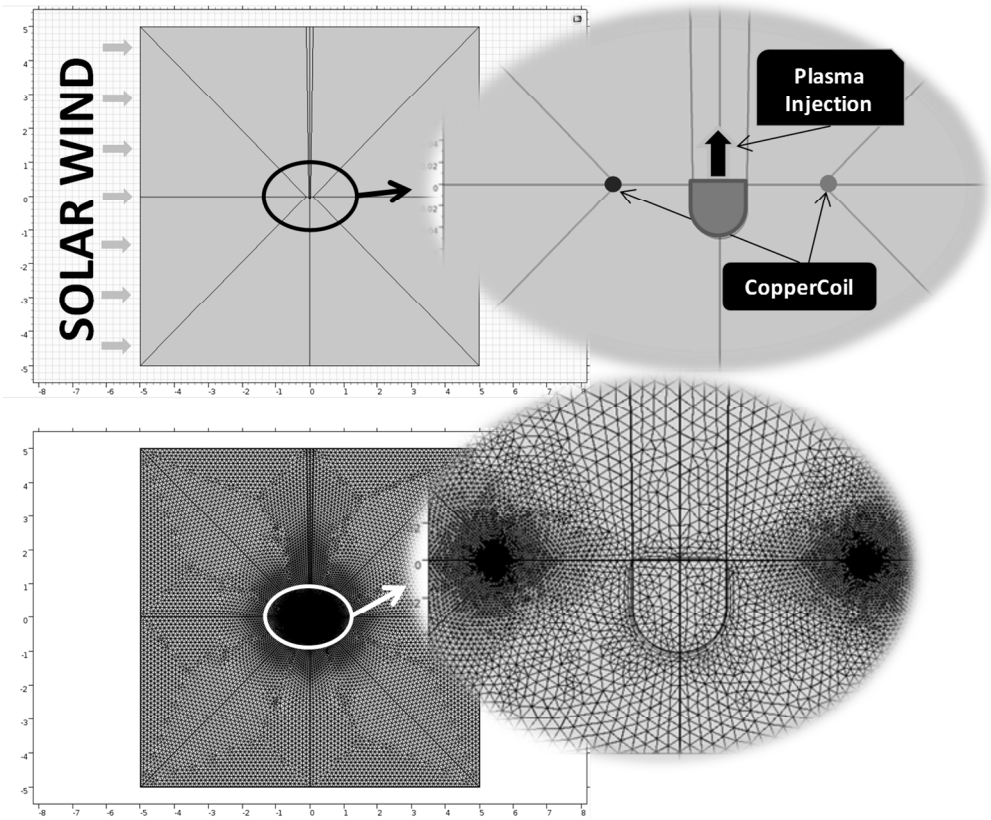

Fig. 43. FEM Study: geometry and mesh

6.6.3 Governing equations, initial values and boundary conditions

Several transient MHD simulations have been performed combining the laminar flow with the magnetic fields module of the commercial software COMSOL® [5]. The interaction between the physics is due to the Lorentz force (see equation (2—1)). The Laminar Flow interface is used to compute velocity $\boldsymbol{u}$ and pressure p fields for a single-phase fluid in the laminar flow regime. A flow remains laminar as long as the Reynolds number is below a critical value, which depends on the studied system. Even if the simulated conditions are nearly turbulent, the system has been modelled as if it had a laminar behavior in order to reduce the computational costs. The model equations are the Navier-Stokes equations for conservation of momentum (6—3) and the continuity equation (6—4) for conservation of mass.

$$\rho(\boldsymbol{v}\cdot\nabla)\boldsymbol{v} = \nabla\cdot\left[-p\boldsymbol{I} + \mu(\nabla\boldsymbol{v} + (\nabla\boldsymbol{v})^T) - \frac{2}{3}\mu(\nabla\cdot\boldsymbol{v})\boldsymbol{I}\right] + \boldsymbol{F} \qquad (6—3)$$

$$\nabla(\rho\cdot\boldsymbol{v}) = 0 \qquad (6—4)$$

The considered boundary conditions have been:

Fluid properties; used to set the fluid dynamic properties of the mean and the reference temperature and pressure in the whole domain;

Initial Values; all the initial values of the variables have been set to zero;

Wall no-slip, which sets to zero the velocity of the fluid at the edge, has been considered for the injector walls and the coil;

Inlet; sets the velocity of the solar wind flow from the left edge of the domain and the velocity of plasma injection on the upper boundary of the injector (see Fig. 43)

Outlet; null pressure has been imposed as outlet boundary condition on the remaining external edges;

The Magnetic Fields interface is used to compute magnetic field and induced current distributions within and around coils and magnets. The physics interface solves Maxwell's equations formulated using the magnetic vector potential ($\boldsymbol{A}$), whose initial value has been set to zero.

$$\sigma \cdot \frac{\partial \boldsymbol{A}}{\partial t} + \nabla \times \boldsymbol{H} = \boldsymbol{J_e} \qquad (6—5)$$

$$\boldsymbol{B} = \nabla \times \boldsymbol{A} \qquad (6—6)$$

$$\boldsymbol{B} = \mu \cdot \boldsymbol{H} \qquad (6—7)$$

The considered boundary conditions have been:

Ampére's law; sets the electromagnetic properties of the mean and the reference temperature and pressure in the whole domain;

Magnetic Insulation; sets the tangential components of the magnetic potential to zero, has been imposed at the external boundaries of the studied domain;

Initial Values; all the initial values of the variables have been set to zero;

External current density; imposes a current density in the order of 10^7 [A/m^2] inside the coil positioned at the center of the domain, which is constant along the whole cross section.

Firstly a transient simulation of the dipole magnetic field has been performed in order to assess its distribution in domain.

Hereinafter, the magnetic field module has been coupled with the fluid-dynamic one by introducing an induced current linked to interaction between the calculated electromagnetic field and the velocity field coming from the laminar flow module:

$$\boldsymbol{J_i = \sigma(E + v \times B)} \qquad (6—8)$$

The total current density will be the sum of the external imposed one with the induced one:

$$\boldsymbol{J = J_e + J_i} \qquad (6—9)$$

At the same time, to complete the bi-directional coupling, also a volume force, the Lorentz force (see equation (2—1)), has been added to the fluid-dynamic settings.

6.7 Results & comments

Starting from the previously described rough conditions, a transient FEM multiphysics simulation of three steps has been performed in 2D in order to qualitatively assess the magnetosphere formation process of the MPS system. First of all, a simple transient magnetic study has been run until reaching of steady state conditions in order to visualize the magnetic field due to the imposed current in the coil (Fig. 44).

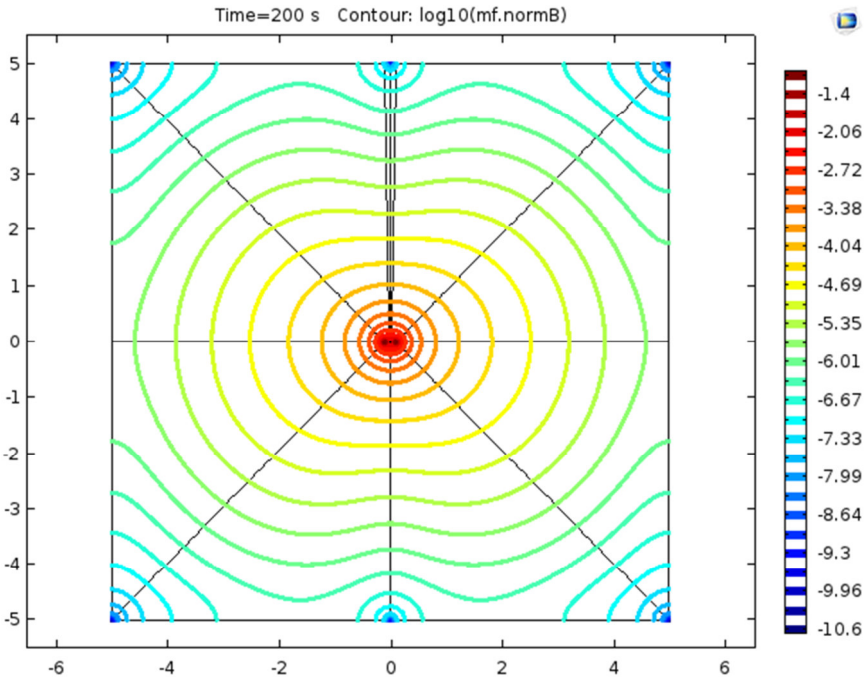

Fig. 44. Regime magnetic flux density norm B (log scale)

Moreover a second transient simulation has been performed, with a duration of 50 [s], by coupling fluid dynamics and electromagnetism with the goal to demonstrate the possibility to inflate the magnetic field due to the injection of highly conducting plasma inside the coil. A first evidence of the effect of the plasma injection in terms of magnetic sail inflation is given in the following contour maps of the magnetic field norm (Fig. 45) and of the induced current density (Fig. 46).

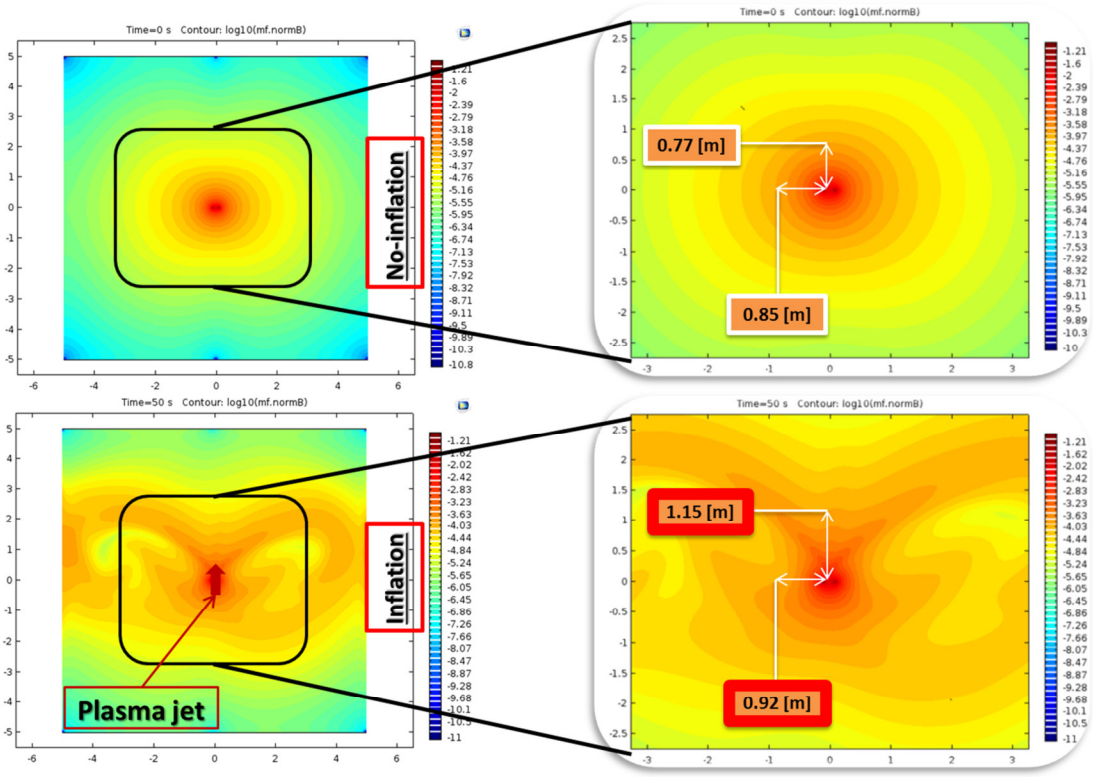

Fig. 45. Effect of 50 [s] of plasma injection at 10 [m/s] on the B field (isolines-log scale)

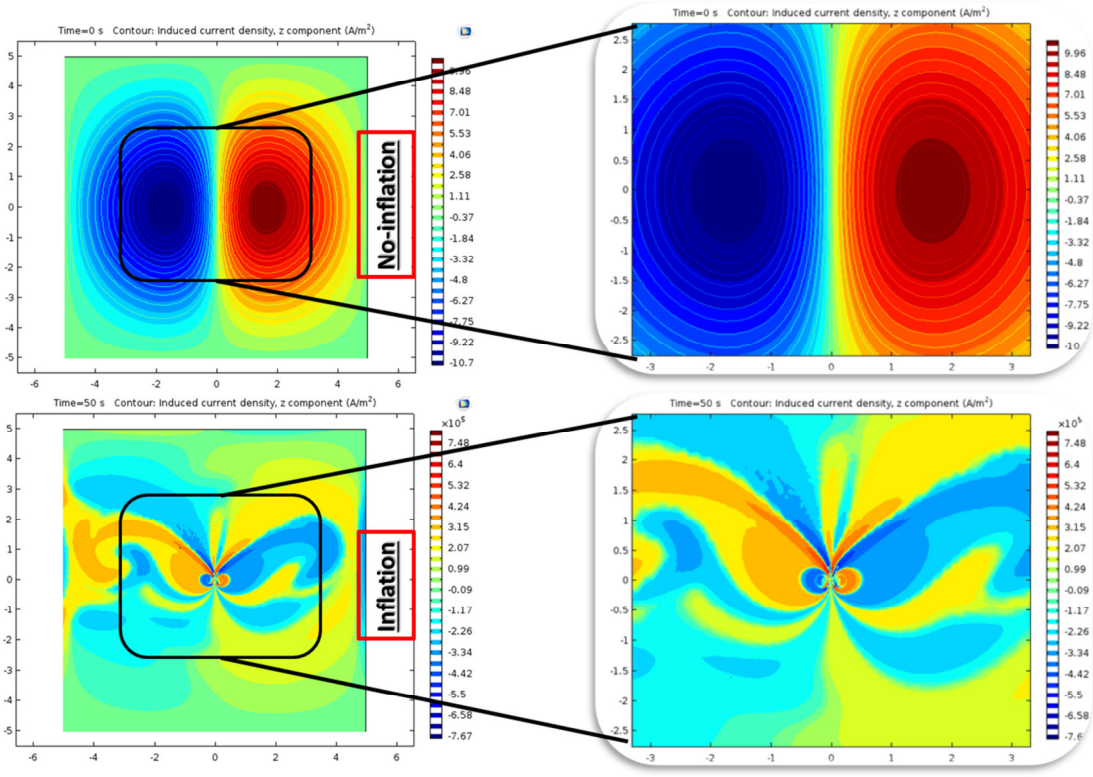

Fig. 46.Induced current density before and after 50 [s] of plasma injection

With the aim to reduce the computational complexity of the model, the coil is considered immersed in a highly conducting mean. This choice makes the model different from the real application, but it is able to reproduce the same effect occurring in the magnetic sails in the Space.

The injection of plasma is simulated by imposing a velocity of the mean at the center of the coil equal to 10 [m/s]. In Fig. 47 and Fig. 48, the effect of this injection is clearly shown. The diagrams show the profile of the magnetic field with respect to the distance, along the sub-solar direction and its perpendicular direction (red arrows in Fig. 47 and white lines in Fig. 48).

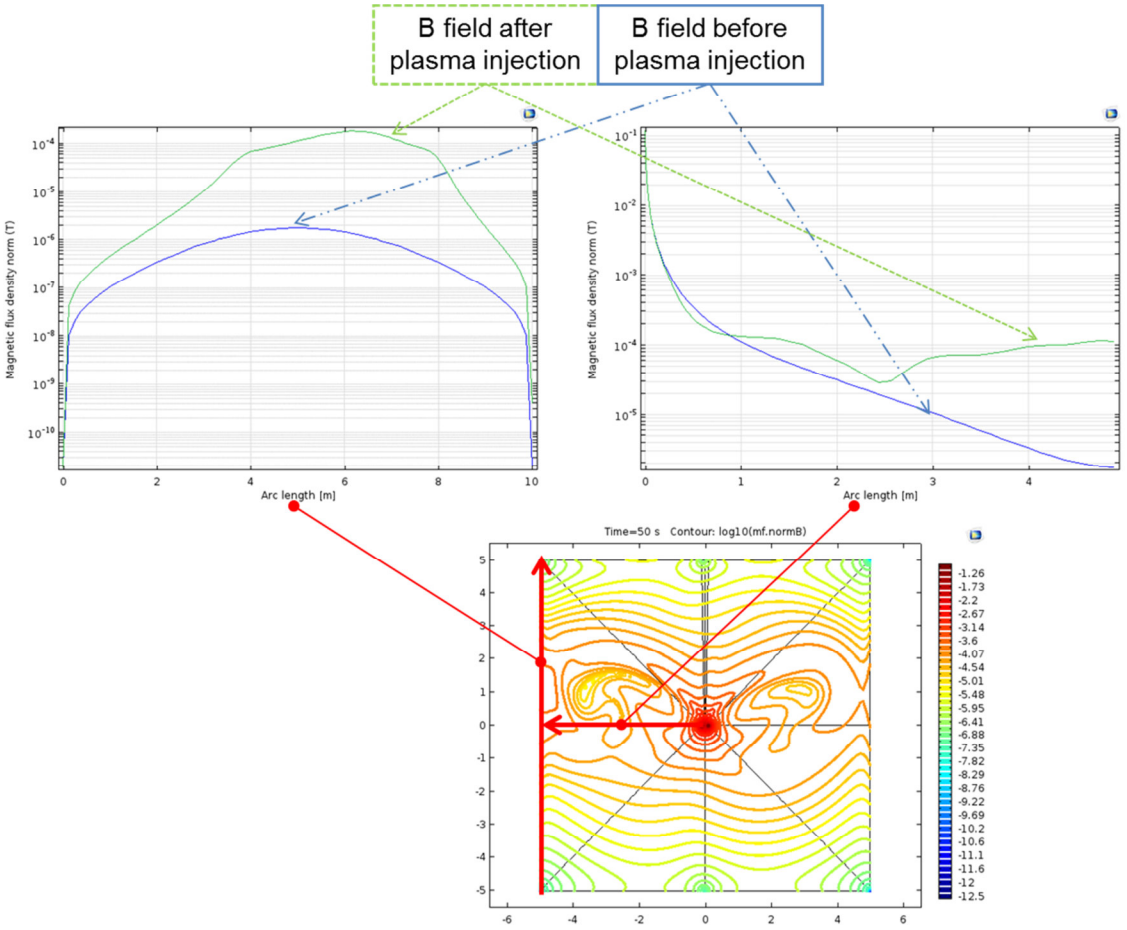

Fig. 47. B field along the red highlighted directions before and after 50 [s] of plasma injection

Without any injection, a simple dipole magnetic field vanishes more or less with the cube of the distance (blue line in Fig. 47 on the upper right image). This decay rate is greater than what we have in the vacuum, because the coil induces a distribution of current in the mean, which act as a shield of the magnetic field. The same diagram shows how the profile changes (green line in Fig. 47 on the upper right image) when a plasma injection at 10 [m/s] is applied axially at the center of the coil. It might be observed also an increase of the B field along the left edge of the domain (green line in

Fig. 47 on the upper left image), which means that the magnetopause is pushed away from the coil and finally the solar sail is enlarged.

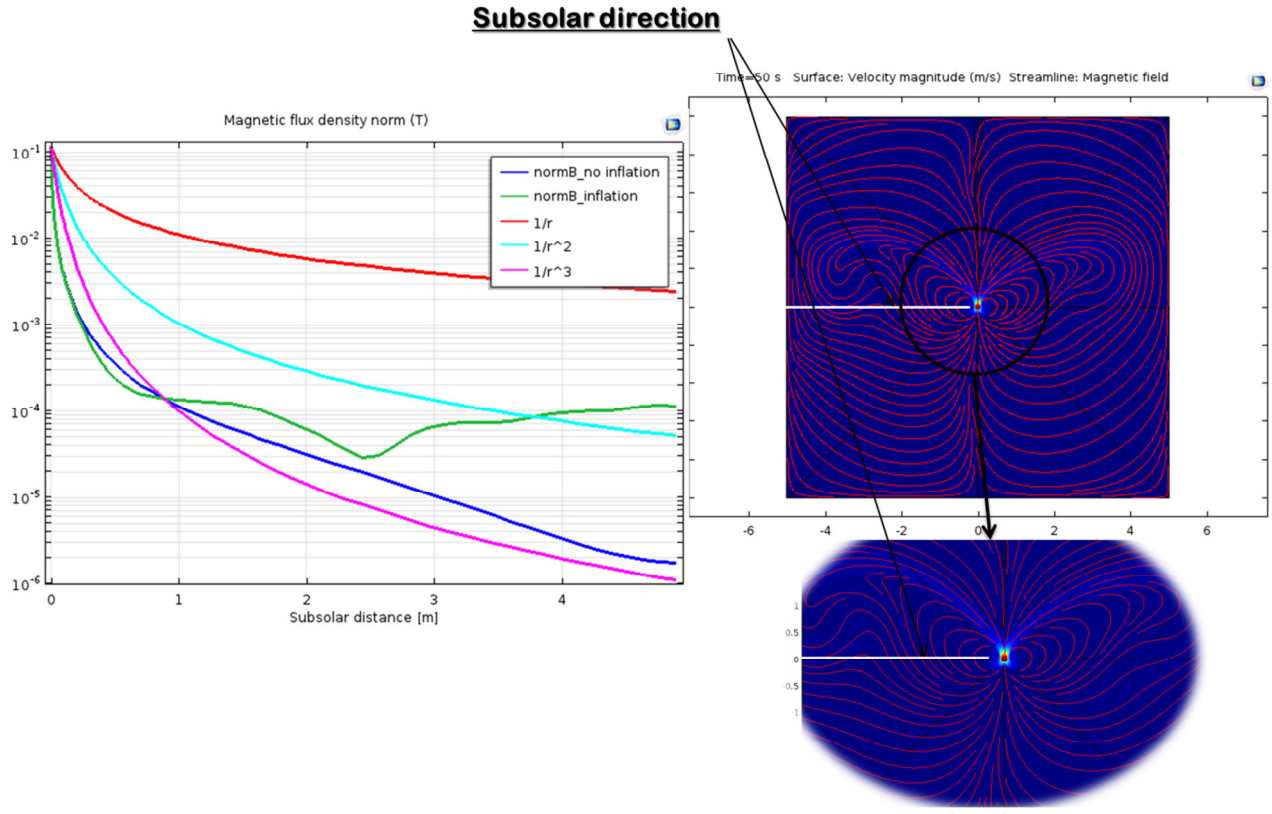

Fig. 48. B field fall off along the sub solar direction faced with the trends: 1/r, $1/r^2$, $1/r^3$

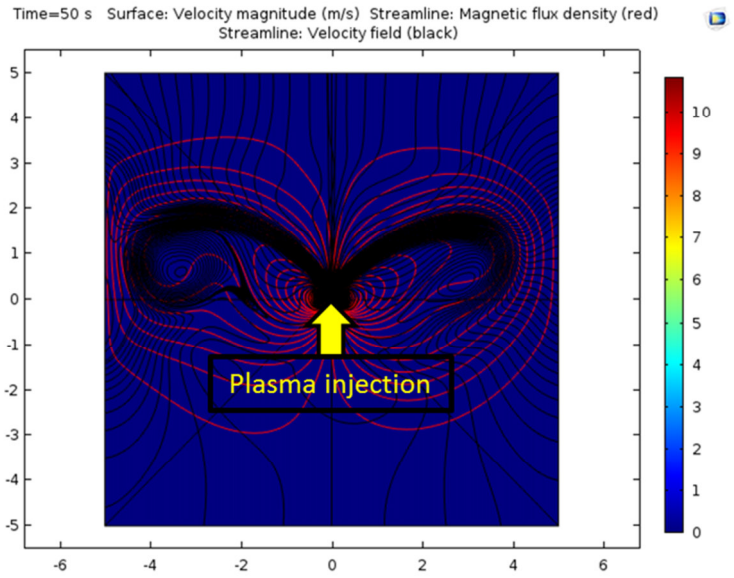

Fig. 49. Inflating effect of a 10 [m/s] plasma injection on the magnetic sail

(Black streamlines = Splitted Velocity field)

(Red streamlines = Enlarged Magnetic field)

A second important issue to establish is the effect of the solar wind on the sail. In fact, the wind exerts a fluid dynamic pressure on the magnetic field and the sail is consolidated when equilibrium with the opposed magnetic pressure is reached. If the force imposed by the wind is too big with respect to the resistance opposed by the magnetic field, it could cause the destruction of the sail. The possibility to establish an equilibrium condition depends on several parameters, the main ones being the wind velocity, the electric current supplying the solid coil and the properties of the injected plasma. In order to deduce that conditions, a velocity, simulating the solar wind, has been set from the left side of the domain and the third step of the transient analysis has been performed with a duration of 20 [s].

In the following, three different scenarios (see Table 13) with the same high conductive fluid (see Table 12) and the same current density imposed in the coil, are compared; the first two with a solar wind velocity of 1 [m/s], while the last one with a solar wind velocity of 10 [m/s]. Each scenario has been analyzed without injection of plasma and with an axial injection of plasma at the center of the coil in the direction orthogonal to the wind, at 1 [m/s] in the first case and at 10 [m/s] for the other two.

Table 13. Velocity settings for the three different case studies

	Case 1	**Case 2**	**Case 3**
Plasma velocity (v_{inj})	1 [m/s]	10 [m/s]	10 [m/s]
Solar wind velocity (v_{sw})	1 [m/s]	1 [m/s]	10 [m/s]

The figures show, for the three case studies, the magnetosphere inflation due to the injection of plasma in terms of velocity (Fig. 50, Fig. 52 and Fig. 54) and magnetic field (Fig. 51, Fig. 53 and Fig. 55). On the left of every image the whole studied domain is shown, before and after the plasma injection, on the right a magnified detail is reported. White and red framed squares inside the right images indicate the magnetic sail dimensions along the sub-solar direction and its perpendicular. The evidence of the inflation is given by the increased distance of the magnetopause limit from the center of the solid coil.

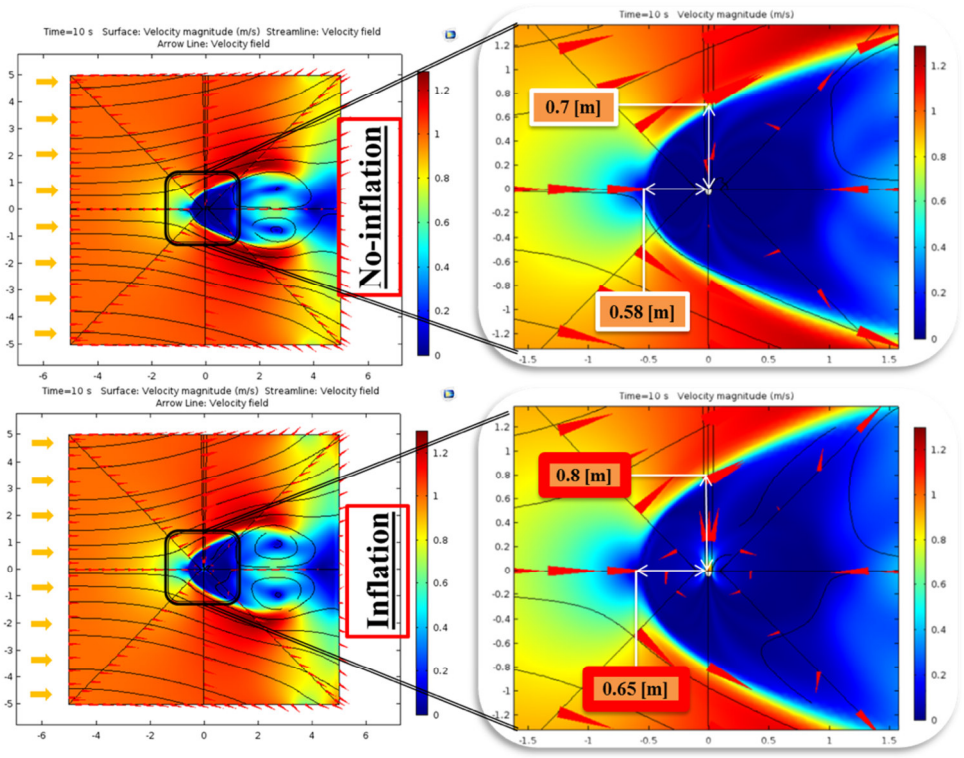

Fig. 50. Case1: Impact of a 1 [m/s] solar wind on the magnetic sail with and without a 1 [m/s] plasma injection (Velocity field)

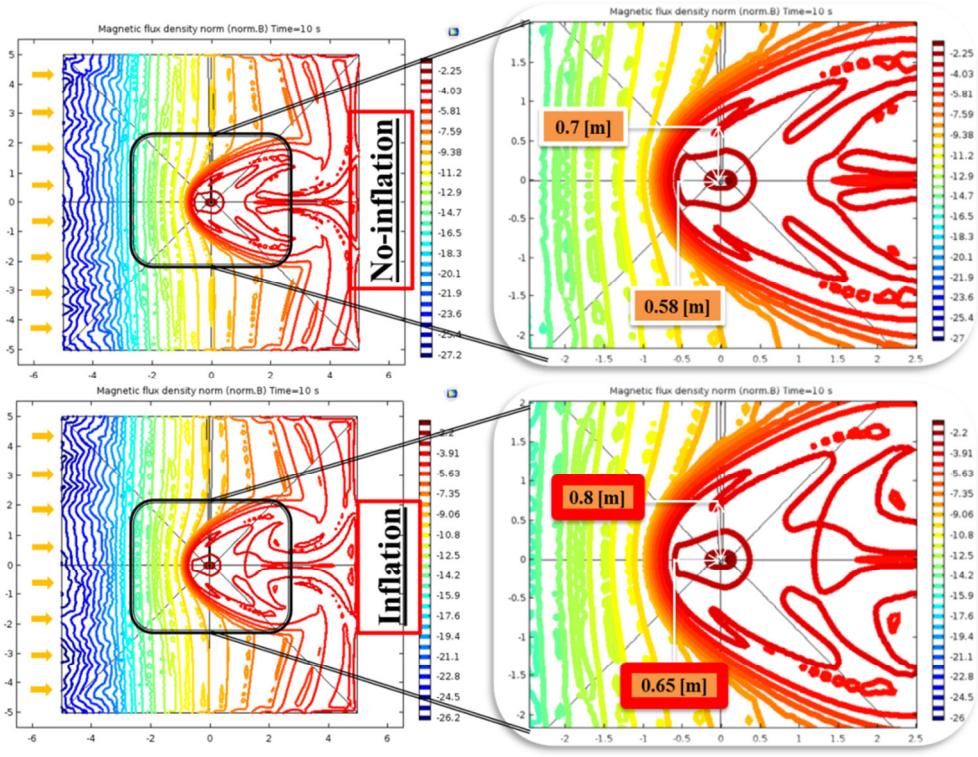

Fig. 51. Case1: Impact of a 1 [m/s] solar wind on the magnetic sail with and without a 1 [m/s] plasma injection (Magnetic Flux Density)

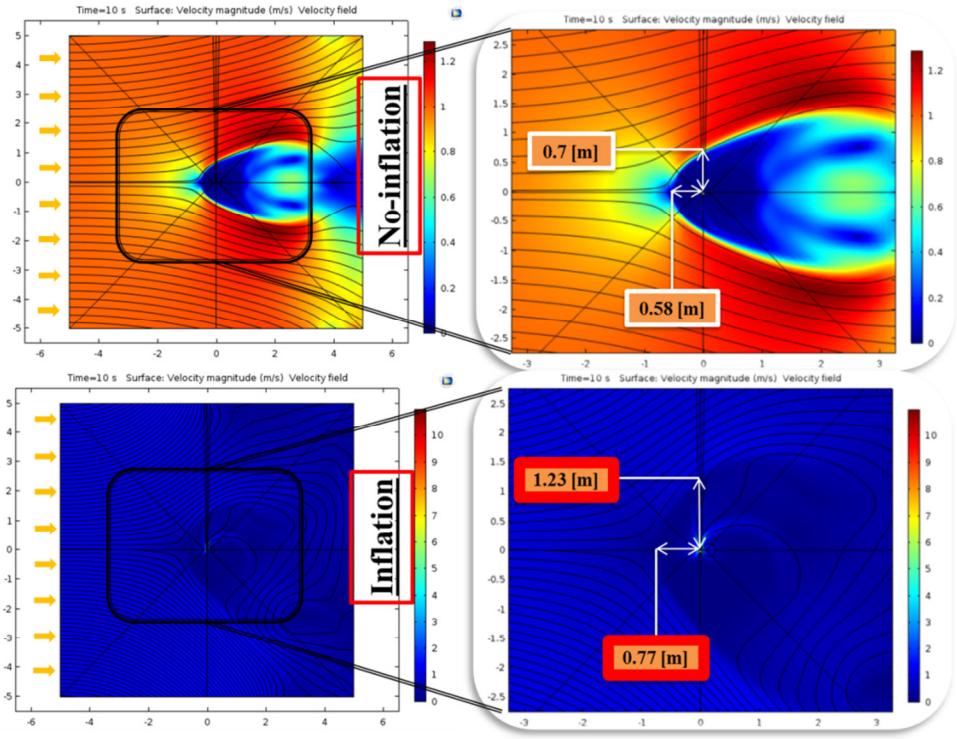

Fig. 52. Case2: Impact of a 1 [m/s] solar wind on the magnetic sail with and without a 10 [m/s] plasma injection (Velocity field)

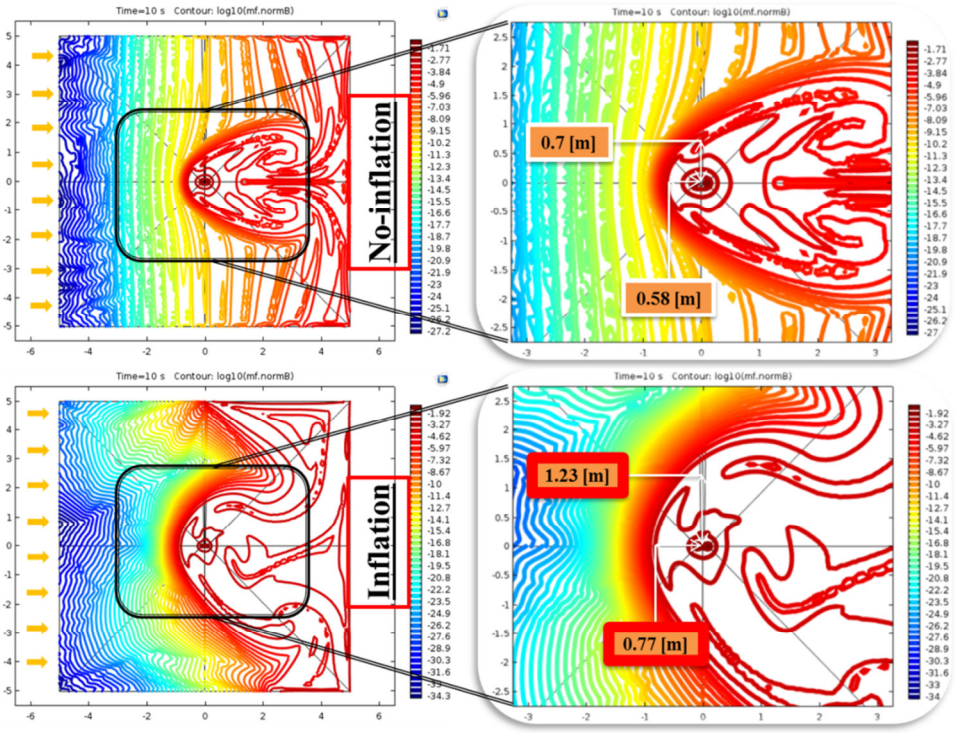

Fig. 53. Case2: Impact of a 1 [m/s] solar wind on the magnetic sail with and without a 10 [m/s] plasma injection (Magnetic Flux Density)

Comparing case 1 with case 2, both from the velocity (Fig. 50 and Fig. 52) and the magnetic induction (Fig. 51 and Fig. 53) point of view, it is noticed in case 2 a bigger inflation effect than in case 1. This is due to the higher velocity of the injected plasma and the corresponding higher Magnetic Reynolds number (see Table 14). Around 32.7% expansion of the magnetic sail along the sub-solar direction (standoff distance) and around 75% extension along its perpendicular is obtained in case 2, whereas, only around 12-14% enlargement regards case 1.

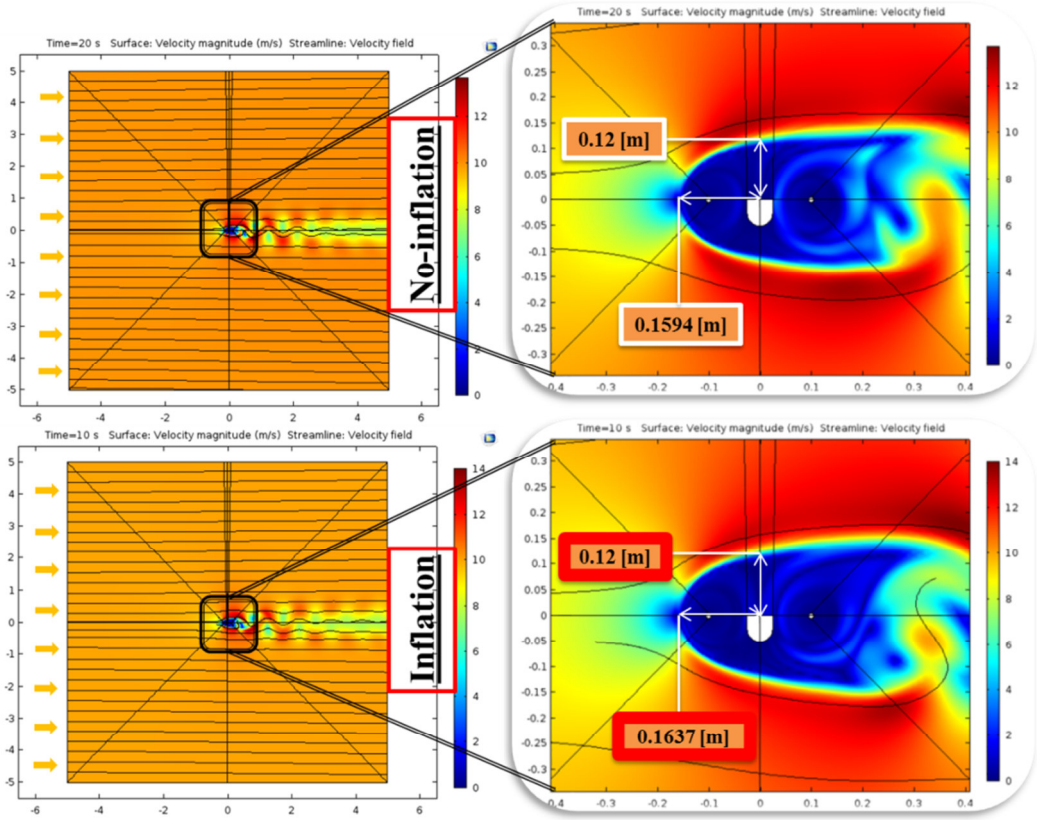

Fig. 54. Case3: Impact of a 10 [m/s] solar wind on the magnetic sail with and without a 10 [m/s] plasma injection (Velocity field)

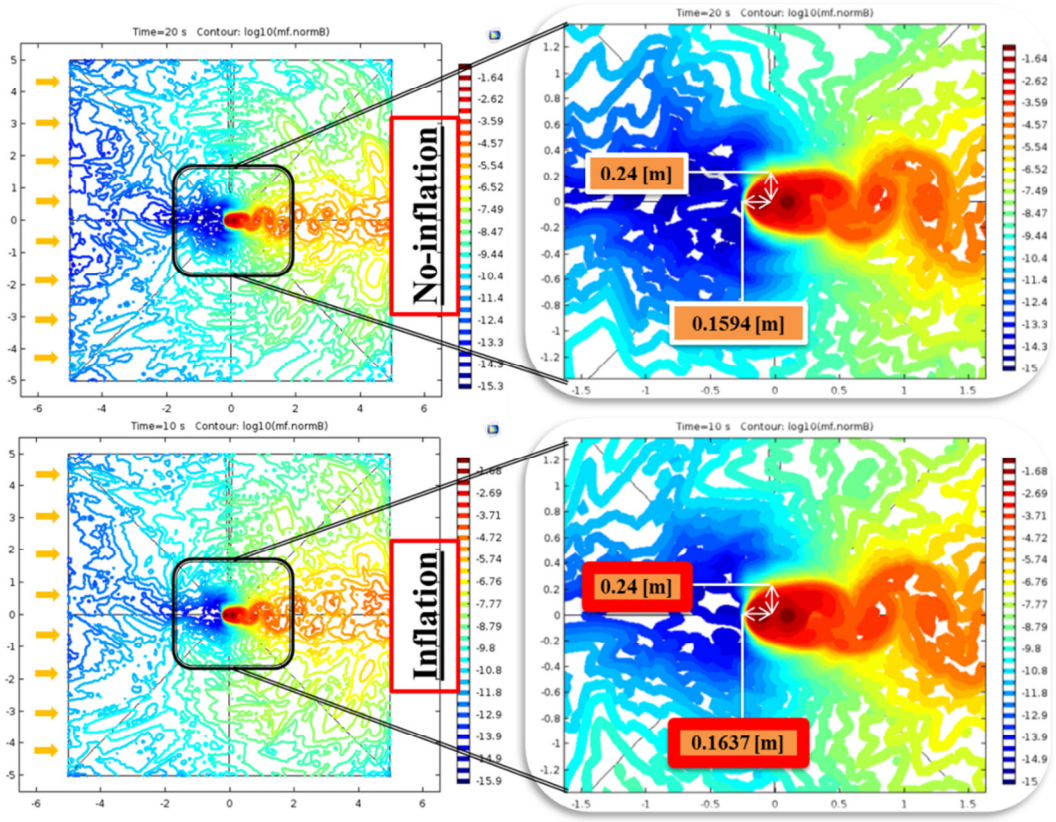

Fig. 55. Case3: Impact of a 10 [m/s] solar wind on the magnetic sail with and without a 10 [m/s] plasma injection (Magnetic Flux Density)

All these images show that the injection of the plasma has the effect of enlarging the magnetic sail and then of increasing the blocking area opposed to the solar wind, so that the thrust on the coil will be increased.

Interesting considerations could be done on the showed deformation of the magnetic sail due to the action of the wind (see Fig. 50, Fig. 51, Fig. 52, Fig. 53, Fig. 54 and Fig. 55).

For case 3, the extension obtained along the sub-solar direction is very weak (only around 2.7%) and the enlargement along its perpendicular is not detectable. This is linked to the velocity of the solar wind which is higher than in the other two cases studied; all the other parameters are the same of case 2. In fact, when the dynamic pressure exerted by the solar wind is too big with respect to the magnetic pressure opposed by the on-board magnetic field, the solar wind could penetrate the magnetic sail removing the injected plasma cloud (see Fig. 54 and Fig. 55).

The deformability of the magnetic sail has also another key effect. The velocity of the wind and the density of the particles reduce moving away from the Sun, and then the thrust should reduce too;

nevertheless, the reduction of the dynamic pressure exerted by the wind allows the sail to enlarge, so that the reduction of the thrust is partially compensated. A similar reasoning can be done also when the spacecraft reaches a high velocity, therefore the relative velocity is reduced and consequently the thrust too. On the other hand, the reduction of the relative velocity determines a reduction of the wind pressure, then the sail enlarges and it can capture a larger tube of flow. Therefore, concluding, the magneto plasma sail behaves as an almost constant push system as it moves away from the sun.

6.8 Conclusions

The results of this study, even if the simulation parameters are right different from the ones of the real Space application (see Table 15), represent a first important step in the comprehension of the phenomenon and allow creating the premises for a dimensionless analysis of the system. Furthermore, since Space like conditions, in terms of density and velocity of the wind, are very difficult to be obtained in laboratory, the dimensionless approach is mandatory.

Table 14. Non-dimensional parameters

Description	**(case1)**	**(case2)**	**(case3)**
Plasma injection velocity	1 [m/s]	10 [m/s]	10 [m/s]
Reynolds number	10^3	10^4	10^4
Magnetic Reynolds number	12.6	126	126
Max Interaction parameter	10^5	10^4	10^4

The results provided indications on the non-dimensional numbers (Table 14), such as the fluid dynamic and magnetic Reynolds numbers and the MHD interaction parameter, whose values have a range of validity, which do not depend on the domain and the parameters of the model.

Starting from the simulated conditions, which allowed demonstrating the feasibility of the magnetic sail formation process, the results could be extrapolated toward other orders of magnitude, just taking care to keep the same non-dimensional parameters values. E.g. the inflation effect obtained in case 2, could be moved to higher orders of magnitude for the domain characteristic dimension (standoff distance). As estimated in literature [30], a magnetosphere at least of 10 [km] should be necessary in order to intercept a 1 [N] thrust from the solar wind at 1AU from the sun. By considering the same background fluid of the simulated conditions (same density, viscosity and

permeability), in order to have a 10^4 increment in the sail standoff distance, a 10^4 reduction in the fluid conductivity allow to maintain the same values for R_m and N, ensuring for the same solar wind velocity of the simulation (1 [m/s]), the same percentage of sail enlargement of case 2. Actually, the available degrees of freedom are three, so that aside from the fluid conductivity (linked to the charge number density), also the plasma injection speed and the magnetic flux density (linked to the current density) could be modified in order to reach the goal of a 10 kilometers magnetic sail.

Table 15 summarizes the reference conditions for the non-dimensional parameters calculation used in literature [11] [26] and for the FEM simulation proposed in this thesis study.

Table 15. Reference conditions for the non-dimensional parameters calculation

	Description	**Injected plasma** (simulation)	**Injected plasma** (from literature) [11][26][28][30]
v	Velocity [m/s]	See Table 13	$2 \cdot 10^4$
L	System characteristic dimension [m] (coil radius)	0.1	10^4
ρ	Mass density [kg/m^3]	1	-
η	Dynamic viscosity [Pa·s]	10^{-4}	-
σ	Electric conductivity [S/m]	10^8	10^3
$n_{density}$	Charge number density [m^{-3}]	-	$5 \cdot 10^{19}$
B	Magnetic flux density at the coil center[T]	0.1 T	0.015
μ	Magnetic permeability [H/m]	$4\pi 10^{-7}$	$4\pi 10^{-7}$

First, for the injected plasma, the Magnetic Reynolds number is much greater than one, so that the magnetic field may be considered in frozen conditions, and its field lines will be strongly advected by the fluid flow as confirmed from the simulation results (see Fig. 45, Fig. 47 and Fig. 48).

Furthermore, the interaction parameter, which represents the ratio between the electromagnetic forces and the inertia forces, is much larger than one too, so that the fluid streamlines are strongly modified by the magnetic field distribution (see Fig. 49).

This globally means that the plasma injected from the center of the on-board coil is able to lead outward the magnetic field, causing its extension far away from the aircraft; contemporarily the plasma results to be confined inside the magnetic bubble, reinforcing the source current density and, consequently, the magnetic field, and allowing a considerable reduction of the fuel consumption.

To summarize, the magnetosphere formation process is shown and its inflation is clearly evidenced. Moreover, the interaction of the magnetic sail with the solar wind flow is qualitatively simulated. The introduction of non-dimensional parameters allows extending the simulation results to different orders of magnitude for the domain, the velocities and all the plasma parameters.

Bibliography

[1] Akita D., Suzuki K., **Kinetic Analysis on Plasma Flow of Solar Wind around Magnetic Sail.** *36th AIAA Plasmadynamics and Lasers Conference,* Toronto, AIAA-2005-4791, 2005.

[2] Ashida Y., Funaki I., Yamakawa H., Usui H., Kajimura Y., Kojima H., **Two-Dimensional Particle-In-Cell Simulation of Magnetic Sails.** *Journal of Propulsion and Power*, Vol.30, No.1, p. 233-245, 2014.

[3] Cassenti B. N., Matloff G. L., Strobl J., **The structural response and stability of interstellar solar sails.** *Journal of the British Interplanetary Society*, Vol.49, p. 345-350, 1996.

[4] Choueiri E. Y., **New dawn for electric rockets.** *Scientific American*, Vol.300, No.2, p. 58-65, 2009.

[5] COMSOL Multiphysics® User's Guide. Version 5.1.

[6] ESA (European Space Agency). **Electric versus chemical propulsion.** Smart-1 mission. http://sci.esa.int/smart-1/34201-electric-spacecraft-propulsion/?fbodylongid=1535

[7] Forward R. L., **Grey solar sails.** *The Journal of the Astronautical Sciences*, Vol.38, No.2, p. 161-185, 1990.

[8] Fujita K., **Particle Simulation of Moderately-Sized Magnetic Sails**. *The Journal of Space Technology and Science*, Vol.20, No.2, p.26-31, 2004.

[9] Funaki I., Ashida Y., Yamakawa H., Kajimura Y., **Analysis of a small-scale Magneto Plasma Sail and Propulsive Characteristics.** *Transactions of the Japan Society for Aeronautical and Space Sciences*, Vol.12, No.29, p. 11- 18, 2014.

[10] Funaki I., Yamakawa H., Kajimura Y., Ueno K., Oshio Y., Nishida H., Usui H., Matsumoto M., Shinoara I., **Experimental and Numerical Investigations on the Thrust Production Process of Magnetoplasma Sail.** *46th AIAA/ASME/SAE/ASEE Joint Propulsion Conference* Nashville, Tennessee, USA, 2010.

[11] Funaki I., Yamakawa H., **Solar Wind sails.** *Exploring the Solar Wind*, Dr. Marian Lazar (Ed.), InTech, 2012. http://www.intechopen.com/books/exploring-the-solar-wind/solar-wind-sails

[12] Goebel D. M., Kantz I., **Fundamentals of Electric Propulsion: Ion and Hall Thrusters.** *Space Science and Technology series*, Vol.1, 2008.

[13] Greschik G., Mikulas M. M., **Design Study of a Square Solar Sail Architecture.** *Journal of Spacecraft and Rockets*, Vol.39, No.5, 2002.

[14] Hathaway D. H., **The Solar Wind.** Solar Physics, Marshall Space Flight Center. *NASA* http://solarscience.msfc.nasa.gov/SolarWind.shtml

[15] Kajimura Y., Funaki I., Shinohara I., Usui H., Yamakawa H., **Thrust Evaluation of Magneto Plasma sail by Using Three-Dimensional Hybrid PIC Code.** *46th AIAA/ASME/SAE/ASEE Joint Propulsion Conference*, Nashville, Tennessee, USA, 2010.

[16] Kajimura Y., Usui H., Ueno K., Funaki I., Nunami M., Shinohara I., Nakamura M., Yamakawa H., **Hybrid Particle-in-Cell Simulations of Magnetic Sail in Laboratory Experiment.** *Journal of Propulsion and Power*, Vol.26, No.1, p. 159-166, 2010.

[17] Khazanov G., Delamere P., Kabin K., Linde T. J., **Fundamentals of the Plasma Sail Concept: Magnetohydrodynamic and Kinetic Studies.** *Journal of Propulsion and Power*, Vol.21, No.5, p.853-861, 2005.

[18] Kojima H., Funaki I., Shimizu Y., Yamakawa H., Shinohara S., Nakayama Y., **Experimental Simulation of a Plasma flow around Magnetic Sail.** *IEPC-2005-107, 29th International Electric Propulsion Conference*, Princeton University, USA, 2005.

[19] Leipold M., Fichtner H., Heber B., Groepper P., Lascar S., Burger F., Eiden M., Niederstadt T., Sickinger C., Herbeck L., Dachwald B., Seboldt W., **Heliopause Explorer-a sailcraft mission to the outer boundaries of the solar system.** *Acta Astronautica*, Vol.59, p. 785-796, 2006.

[20] Moritaka T., Usui H., Nunami M., Kajimura Y., Nakamura M., Matsumoto M., **Full Particle-in-Cell Simulation Study on Magnetic Inflation around a Magneto Plasma Sail.** *IEEE Transactions on Plasma Science*, Vol.38, No.9, 2010.

[21] Nishida H., Nakayama Y., **Two-dimensional Magnetohydrodynamic Simulation of a Magnetic Sail.** *Journal of Spacecraft and Rockets*, Vol.43, No.3, p.667-672, 2006.

[22] Nishida H., Funaki I., Ogawa H., Inatani Y., **MHD Analysis on Propulsive characteristics of Magneto Plasma Sail.** *IEPC-2007-195, 30th International Electric Propulsion Conference*, Florence, Italy, 2007.

[23] Nishida H., Funaki I., **Analysis of Thrust Characteristics of a Magnetic Sail in Magnetized Solar Wind.** *Journal of Propulsion and Power*, Vol.28, No.3, 2012.

[24] Ren C., **Introduction to Particle-in-Cell Methods in Plasma Simulations.** University of Rochester, *Proceedings from the HEDP Summer School*, 2011.

[25] Richtmyer R. D., Morton K. W., **Difference Methods for Initial Value Problems.** *Interscience Publisher*, p. 300, New York, 1967.

[26] Ueno K., Ayabe T., Funaki I., Horisawa H., Yamakawa H., **Imaging of Plasma Flow around Magnetoplasma Sail in Laboratory Experiment.** *Journal of Plasma and Fusion Research*, Vol.8, 2009.

[27] Ueno, K., Funaki, I., Kimura, T., Horisawa, H., and Yamakawa, H., **Thrust Measurement of Pure Magnetic Sail using Parallelogram-pendulum Method**. *Journal of Propulsion and Power*, Vol.25, No.2, p.536-539, 2009.

[28] Ueno K., Kimura T., Ayabe T., Funaki I., Yamakawa H., Horisawa H., **Thrust Measurement of Pure Magnetic Sail.** *Transactions of the Japan Society for Aeronautical and Space Sciences*, Vol.7, No.26, p. 65-69, 2009.

[29] Winglee R. M., **Mini-Magnetospheric Plasma Propulsion (M2P2)**. *NASA Innovative Advanced Concepts (NIAC)*, Award No. 07600-010, Final report. NASA, 1999.

[30] Winglee R. M., Slough J., Ziemba T., Goodson A., **Mini-Magnetospheric Plasma Propulsion: Tapping the energy of the solar wind for spacecraft propulsion.** *Journal of geophysical research*. Vol.105, No.A9, p. 21,067-21,077, 2000.

[31] Winglee R. M., Slough J., Ziemba T., Goodson A., **Mini-Magnetospheric Plasma Propulsion: High Speed Propulsion Sailing the Solar Wind.** *Space Technology and Applications International Forum-2000*, American Institute of Physics, **CP504**, p. 962, 2000.

[32] Winglee R. M., Slough J., Ziemba T., Euripides P. Gallagher D., **Laboratory testing of mini-magnetospheric plasma propulsion prototype.** *Space Technology and Applications International Forum*, American Institute of Physics, **CP552**, p. 407, 2001.

[33] Winglee R. M., Ziemba T., Euripides P., Slough J., **Computer modeling of the laboratory testing of Mini-Magnetospheric Plasma Propulsion (M2P2).** *Proceedings of the 27th International Electric Propulsion Conference*, October 15-19, 2001.

[34] Winglee R. M., Slough J., Ziemba T., Euripides P., Adrian M. L., Gallagher D., Craven P., Tomlinson W., Cravens J., Burch J., **Large-Scale Mini-Magnetosphere Plasma Propulsion**

(M2P2) Experiments. *Proceedings of the 7th International Spacecraft Charging Technology Conference, ESTEC*, European Space Agency, ESA SP-476, p. 593, 2001.

[35] Winglee R. M., Euripides P., Ziemba T., Slough J., Giersch L., **Simulation of Mini-Magnetospheric Plasma Propulsion (M2P2) interacting with an external plasma wind.** *39th AIAA/ASME/SAE/ASEE Joint Propulsion Conference and Exhibit*, Huntsville, AIAA 2003-5224, Alabama, USA, 2003.

[36] Winske D., Omidi N., **Plasma expansion in the presence of a dipole magnetic field.** *Physics of Plasmas*, Vol.12, No.7, 072514, 2005.

[37] Yamakawa H., Funaki I., Nakayama Y., Fujita K., Ogawa H., Nonaka S., Kuninaka H., Sawai S., Nishida H., Asahi R., Otsu H., Nakashima H., **Magneto-plasma sail - An engineering satellite concept and its application for outer planet missions.** *Acta Astronautica*, Vol.59, p. 777-784, 2006.

[38] Ziemba T., Winglee R. M., Slough J., Euripides P., **Parameterization of the Laboratory Performance of the Mini-Magnetospheric Plasma Propulsion (M2P2) Prototype.** *27th International Electric Propulsion Conference*, October 15-19, 2001.

[39] Ziemba T., Euripides P., Winglee R. M., Slough J., Giersch L., **Efficient plasma production in low background neutral pressures with the M2P2 prototype.** *39th AIAA/ASME/SAE/ASEE Joint Propulsion Conference*, July 20-23, 2003.

[40] Zubrin R. M., Andrews D. G., **Magnetic Sails and Interstellar Travel.** *Journal of the British Interplanetary Society*, Vol.43, p. 265-272, 1990.